Politecnico di Torino

Master's Degree in Materials Engineering

Academic Year 2025/2026

Graduation Session March 2026

Heat treatments optimization of a novel nickel-based superalloy designed for high temperature applications manufactured via PBF-LB

Thesis supervisors:
Prof. Daniele Ugues
Prof. Emilio Bassini

Candidate:
Mattia Cannella

Abstract

The present thesis focuses on the optimization of solution and aging heat treatments for a novel nickel-based superalloy produced by Laser Beam Powder Bed Fusion (PBF-LB). This superalloy was specifically developed for gas turbine applications, which require enhanced creep resistance, excellent high-temperature performance, and low susceptibility to strain-age cracking (SAC). Owing to the absence of literature on appropriate heat treatment strategies for this material, preliminary thermal characterization was conducted using Differential Scanning Calorimetry (DSC).

As the alloy is intended for critical components that must exhibit minimal residual defects, such as pores or cracks, Hot Isostatic Pressing (HIP) was applied as an essential initial post-processing step to ensure defect healing. Based on the thermal analysis results, solution heat treatment trials were subsequently performed on HIP-treated samples. In the first series of trials, solution treatments were conducted within the optimal temperature window identified by DSC analysis, followed by air cooling, corresponding to a high cooling rate. The treated samples were extensively characterized, with particular emphasis on microstructural evolution.

Microstructural analysis primarily focused on identifying detrimental phases potentially formed due to overheating during the solution treatment. This investigation was essential because grain size maximization was a key requirement for improving creep resistance. After determining the maximum allowable solution temperature, defined by the onset of incipient melting, secondary phase analysis was carried out. In particular, γ' precipitates and carbides were quantitatively evaluated using image analysis techniques, as these phases are chiefly responsible for high-temperature mechanical strength.

In the second series of solution treatment trials, controlled cooling was performed in a low-pressure furnace to better replicate industrial conditions, targeting a cooling rate of 40 °C/min.

Following optimization of the solution treatment parameters, which resulted in the desired γ' fraction and precipitate size, the aging treatment was subsequently optimized. A similar microstructural and hardness characterization was conducted on the aged samples to achieve further refinement. This systematic approach led to the development of an alternative and highly stable heat treatment recipe that provides a favourable balance between creep resistance and hardness. Future work will involve applying this optimized treatment to tensile specimens in order to obtain a more comprehensive assessment of the mechanical performance of this novel superalloy.

Contents

1. Introduction

1.1. Metal additive manufacturing

Additive Manufacturing (AM) involves the layer-by-layer production of components from Computer-Aided Design (CAD) data. Unlike traditional manufacturing technologies for metallic materials such as casting, forging, or milling, AM does not involve the removal of material; it simply adds material layer by layer. Compared to casting, AM can overcome the limitations of mold and size, enabling the direct production of parts with extremely complex shapes. The AM process offers significant advantages in terms of complexity, enabling innovative designs to be created for enhanced mechanical and thermal performance and reduced system mass. Indeed, AM design allows for the consolidation of multiple components into one, enabling lightweighting. Furthermore, AM design freedom allows for optimized material distribution, reducing mass while maintaining the mechanical and other performance requirements of the component [1]. Another advantage is the ability to rapidly prototype, thereby shortening the product development cycle [2].

In addition to the aforementioned benefits, it is important to acknowledge the disadvantages associated with the utilisation of AM. Every AM technique has specific drawbacks, but many of these are common to different ones. The main issues encountered in production include size limitations, imperfections in the material, uncertainty regarding the material's properties and long-term performance, and a lack of predictability and repeatability in the process [3].

Therefore, the AM process needs to be more reliable and optimized in order to be adopted for production. To optimize the manufacturing process, a deep knowledge of the process itself is required. While traditional manufacturing techniques are well understood and the outcome of the process is relatively easy to predict, AM lacks this level of understanding. Real systems need to be simulated by models that aim to accurately predict their performance. Hence, modelling metal AM is a key area of research as it is the main enabler of final component optimization [4].

Another critical issue is the limited selection of materials that can be used in the process compared to traditional techniques. Indeed, materials classified as non-weldable, such as alloys that contain a relatively high content of elements like aluminium or titanium, are subject to cracking, making it very difficult to produce defect-free parts using AM [5].

Lastly, additively manufactured components need customised post-processing treatments to enhance mechanical properties. The presence of high residual stress (due to the very rapid solidification rate) and porosity resulting from the AM process,

requires optimization of heat treatment and the application of additional post-processing operations, such as Hot Isostatic Pressing (HIP) [6]. Therefore, despite its high potential, AM has not yet reached a high level of technology readiness in some sectors, and much research work is needed to make it industrially viable.

1.1.1. Laser Beam Powder Bed Fusion (PBF-LB)

The Laser Beam Powder Bed Fusion (PBF-LB), also known as Selective Laser Melting (SLM), Direct Metal Laser Melting (DMLM) or Direct Metal Laser Sintering (DMLS), is one of the main technologies of AM for the production of metallic materials. It is becoming increasingly popular in industry thanks to its ability to produce high-quality parts with fine feature sizes and adequate build volumes for a wide range of part sizes. PBF-LB diffusion has spread widely and reached many different sectors, such as aerospace, automotive, biomedical and energy [7].

In the PBF-LB process, the laser beam acts as the heat source, selectively melting the layer of powder spread on the substrate. In particular, specific points of the powder bed are scanned by the laser beam along previously programmed paths. Indeed, in this process, the computer generates a two-dimensional scanning path according to the profile, controlling the position of the scanning mirror to direct and change the laser path. The melted powder layer then cools and solidifies to form a new, compact layer of the final component. Once the first layer is complete, the powder dispenser platform moves upwards to supply the material needed to create the next level. The building platform then lowers by a distance equal to the layer thickness and the recoater transfers material from the dispenser to the building platform to form a new level. This cycle is repeated until the final component is finished [8]. Figure 1.1 shows a representative scheme of the process.

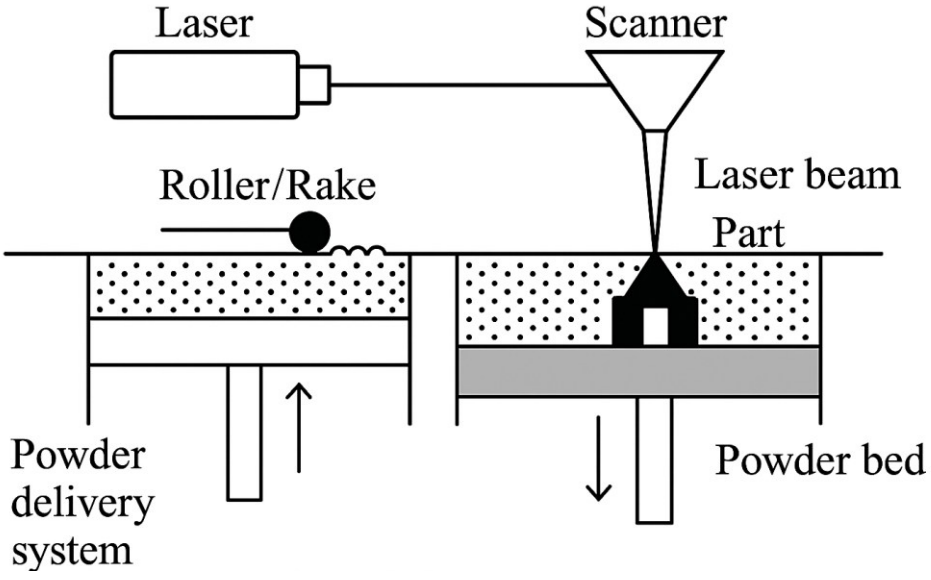

Figure 1.1: Scheme of PBF-LB process.

Although the process is relatively simple in terms of functioning, it involves an extremely high number of parameters that influence the outcome. For example, Rehme and Emmelmann [9] stated that the process is affected by around 130 input parameters. The parameters can be divided into can be divided into four large groups: machine-based, material-based, process and post-treatment parameters. Another crucial factor is that the part must be fixed directly to the substrate, either independently or via support structures. The supports serve to fix the part to the base plate, prevent deformation, and facilitate heat dissipation. In addition to the parameters, consideration must also be given to the design of the component and the supports to ensure the part has a high density, good surface quality and high accuracy [7].

Moving on to the components necessary for PBF-LB machine, the main structural parts of the system as described by Yadroitsev et al. [7] are:

- Laser: in the majority of cases, the PBF-LB system employs a continuous wave Yb-fiber laser, (Ytterbium-doped fiber laser) with wavelength of approximately 1070 nm, as a source for the beam.
- Scanning system: the beam passes through the laser beam expander and enters the scanning system. There are usually two distinct types of scanning system optics: passive and active. Regardless of the configuration, beam deflection is achieved by means of two independently controlled mirrors.
- Powder delivery system: regarding the methods used to carry the powder, there are two main alternatives. The first involves preloading the reservoir with powder, which is then supplied by moving the piston upwards from the bottom. The second approach involves delivering the powder from the upper reservoir to a hopper positioned above the working area.
- Powder deposition system: its primary function is to create an even layer of powder of consistent and uniform thickness on the base plate. Recoating systems include several types of rollers. The roller can move in a linear or circular fashion.
- Build platform: the substrate on which the items are produced is fixed directly to the build platform. Ideally, the substrate material should closely resemble the powder in terms of its chemical composition. This is essential to avoid circumstances where the melting of the powder and substrate leads to the formation of brittle intermetallic compounds or where the metal components are incompatible with each other. To minimise residual stress, platforms equipped with a preheating mechanism are used. Once the build is complete, the manufactured parts are separated from the substrate, typically by wire electrical discharge machining (EDM) or sawing.

Turning to the outcome of the process, one of the most notable features of PBF-LB is the resulting microstructure. However, components produced using PBF-LB will have a different microstructure to those produced using conventional processes.

Indeed, the resulting microstructure is strongly influenced by a cooling rate of up to 10^5 K/s and extreme thermal gradients [10]. The temperature of the melt pool can be extremely high, resulting in the volatilisation of elements and a deviation from the nominal chemical composition [11]. In addition, the material undergoes multiple thermal cycles and is reheated as the next layer is deposited. This commonly results in a cellular/dendritic microstructure, represented in Figure 1.2, that resembles that of a multiple-pass welding process [3].

Although the process has been optimized, the microstructure can still be characterised by critical defects that influence the final properties of the material, such as:

- Porosity: phenomena such as 'lack of fusion' or 'keyhole porosity' can generate a high number of pores [12].
- Residual stress: rapid thermal cycles can result in high residual stress, leading to warping or cracking [13].
- Surface roughness: the irregular surface morphology acts as a potential stress concentrator, influencing the fatigue behaviour [14].

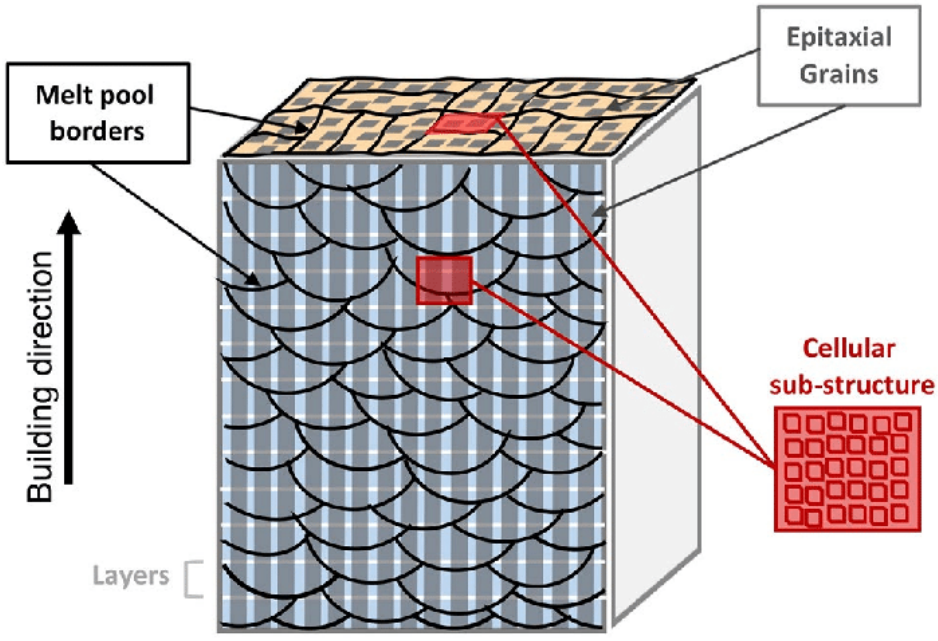

Figure 1.2: Schematic representation of the typical post PBF-LB (as-built) microstructure *[15]*.

Another typical characteristic of PBF-LB microstructures is anisotropy. Indeed, given that the material is built up layer by layer, the grain orientation depends strongly on the building direction. This preferred orientation can significantly influence the mechanical response of the part depending on the direction of the applied load. In order

to mitigate the effects of anisotropy and defects, the use of customised heat treatments and HIP is essential. These processes aim to homogenise the microstructure and close the residual porosity, improving the component density.

Moving on to the materials used, the feedstock metals for PBF-LB are typically pure metals, pre-alloys, and multicomponent alloy powders. The most common metallic materials currently manufactured by PBF-LB are aluminium-based alloys ($AlSi_{10}Mg$), iron-based alloys, titanium-based alloys (Ti_6Al_4V), nickel-based alloys (Inconel series), cobalt-based alloys (CoCr), copper-based alloys (CuCrZr) and stainless steel (316L), as well as intermetallics (Ti-Al) [16] [17].

PBF-LB suitable metallic materials must satisfy several conditions, such as having high weldability and being available in a spherical shape with a diameter of 15-60 µm. Weldability is particularly important because it prevents hot cracking caused by elemental segregation [18].

This restricts the range of materials that can be used compared to conventional processes, which offer notably better scalability and lower powder costs. There is an urgent need to increase the maturity level for serial production, which presents an opportunity for research into expanding the PBF-LB process.

1.2. Nickel-based superalloys

Superalloys are alloys with a complex chemical composition, typically consisting mainly of nickel, cobalt or iron with the addition of various other elements. Superalloys are characterised by their elevated mechanical properties at high temperatures. Indeed, they can withstand operating temperatures of up to 70% of their melting point. This percentage is higher than that of other material classes.

Nickel-based superalloys are a class of superalloys that exhibit exceptional properties, including high-temperature strength, corrosion resistance, and thermal fatigue resistance. These properties make them ideal for use in hot-section components under extreme conditions, including those in aero-engines, gas turbines, hypersonic vehicles and nuclear power plants [19]. Nickel-based superalloys are generally divided into three categories: wet corrosion alloys, high-temperature alloys and special alloys.

Nickel superalloys are a prevalent category of superalloys, for a number of reasons. The Face Centered Cubic (FCC) structure of the material is responsible for its ductility and tenacity. Indeed, an FCC matrix permits a substantial and effective deformation of the material. Furthermore, nickel, unlike iron or cobalt, retains its crystalline configuration even at high temperatures, ensuring remarkable stability, and exhibits excellent corrosion and oxidation resistance owing to its high melting point. Another significant factor is that the diffusion speed in an FCC structure is notably slow, which is a highly beneficial factor in enhancing the creep resistance. Moreover, nickel can dissolve various alloying elements, reaching nearly 50 wt. %, which results in many contemporary Ni-based superalloys containing more than ten alloying elements [20].

1.2.1. Chemical composition

Nickel superalloys are defined by their microstructure, which typically consists of an FCC austenitic matrix (γ), reinforced by γ' precipitate. The chemical elements contained in nickel superalloys can be classified into three main groups based on their characteristics, role, and partition within the different phases of the material:

- Solid solution strengtheners: elements such as cobalt (Co), chromium (Cr), molybdenum (Mo), tungsten (W) and rhenium (Re) are usually found primarily in the γ matrix. These elements improve the resistance of the matrix through solid solution strengthening, impeding dislocation movement. The elements contained in the solid solution differ from nickel in terms of their atomic dimensions and, for this reason, strengthen the matrix to varying degrees. The lattice deformations caused by the foreign atom hinder the motion of dislocations. Aluminium also plays a role in this type of strengthening mechanism, but as its main effect is on the precipitates, it is categorised as a γ' former.

- γ' and γ'' formers: aluminium (Al), titanium (Ti), tantalum (Ta) and niobium (Nb) are responsible for the formation of strengthening phases γ' and γ''. An elevated combined content of Al and Ti has been shown to increase the volumetric fraction of γ', thereby significantly enhancing yield strength and creep resistance at elevated temperatures. However, an excess of these elements can result in an increased tendency for cracking during the additive manufacturing process, as they diminish the weldability of the alloy. This phenomenon can be attributed to the rapid precipitation of phases, which has the potential to generate residual stresses of a particularly high level.

- Grain boundary strengtheners and carbide formers: elements such as carbon (C), boron (B), zirconium (Zr) and hafnium (Hf) segregate at grain boundaries, where they form carbides and borides. These chemical elements are present only in small quantities. Carbon is commonly added to Ni-based superalloys to promote strengthening through carbide precipitation. Indeed, carbides and borides act as obstacles to the sliding mechanism between grains. However, the presence of C inherently reduces weldability, and high carbide density further exacerbates this limitation by increasing susceptibility to both thermal and deformation cracking. In addition, the introduction of rare earth elements such as yttrium (Y), cerium (Ce) and lanthanum (La) acts as a purifying agent, combining with impurities such as sulphur and significantly improving the resistance to oxidation [21]. It is also worth noting that elements primarily classified in other categories, such as Ti, Ta, Cr, and Mo, have been shown to function as carbide formers as well, despite partitioning predominantly to the γ or γ' phases.

Among these elements, it is important to monitor the balance of elements such as Cr, Mo, W and Re, as excessive levels of these species increase the risk of forming brittle intermetallic compounds. These are commonly referred to as Topologically Close-Packed (TCP) phases, the most typical examples of which include the σ, μ, and Laves phases [20]. Effects of main elements on nickel superalloys are resumed in Table *1.1*.

Table 1.1: Summary of the effect of alloying elements in Ni-based superalloys

Element	Solid solution strengthening	Precipitation strengthening	Carbide/boride formation
Co	✓		
Cr	✓		✓
Mo	✓		✓
W	✓		✓
Re	✓		
Hf	✓		✓
Al		✓	
Ti		✓	✓
Ta		✓	✓
Nb		✓	✓

1.2.2. Microstructure and phases characteristics

The microstructure of nickel-based superalloys is characterised by a complex mixture of phases, schematically represented in Figure 1.3, that have a significant impact on the material properties based on their relative abundance, distribution and size.

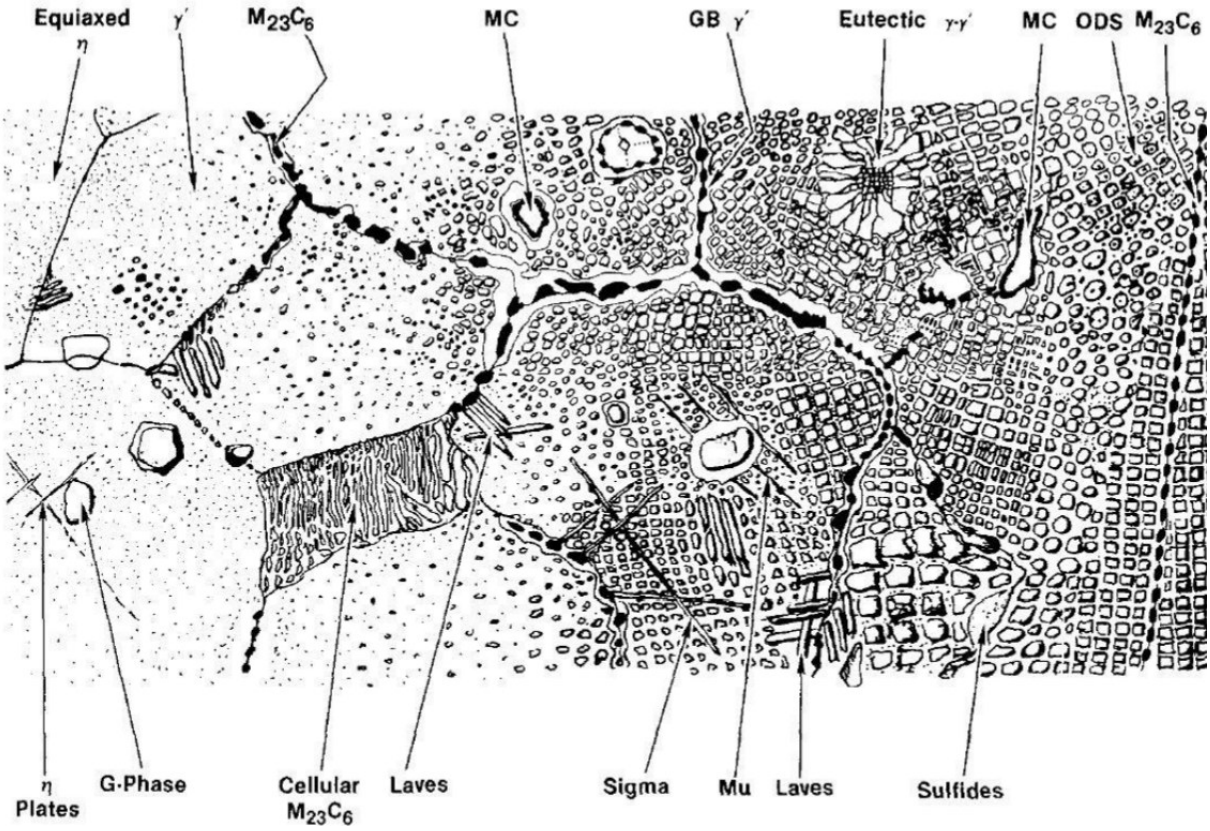

Figure 1.3: Schematical representation of phases contained in Ni-based superalloys *[22]*.

The main phase is the γ austenite matrix, which is a disordered solid solution with an FCC structure. This structure is stable for pure nickel from room temperature up to its melting point (1455 °C), avoiding phase transformations that could cause volumetric changes during heating or cooling. In addition, the high number of slip systems characteristic of the FCC lattice determines the good ductility and toughness of the superalloy matrix.

The main strengthening phase, as previously mentioned, is γ′, an ordered intermetallic phase with an FCC lattice and a generic composition of Ni_3(Al, Ti, Ta). γ′ is derived from the intermetallic compound Ni_3Al. In this compound, aluminium can be partially replaced by titanium, as well as by tantalum and niobium. The composition of the γ′ phase varies in different superalloys depending on the abundance of these elements. Additionally, Ti, Ta and Nb form different lattices when combined with Ni: hexagonal compact for Ni_3Ti, orthorhombic or body-centred tetragonal for Ni_3Nb and body-centred tetragonal for Ni_3Ta. Therefore, depending on the elements present, the parameters of the γ′ cell vary, which also affects the distortion by the misfit with the

γ matrix. The greater the misfit, the greater the internal stress induced in the material. Usually, the interface between γ and γ′ is coherent, but when Al is abundantly substituted by other elements in γ′, the misfit grows and the interface could become incoherent.

In nickel-based superalloys, γ′ precipitates are generally classified into three distinct populations, namely primary, secondary, and tertiary, as illustrated in Figure 1.4. Primary γ′ is characterised by comparatively large precipitates of irregular morphology, situated at grain boundaries. Secondary γ′ precipitates are finer and are distributed within the grain interior; depending on the heat treatment applied, they may adopt a variety of morphologies, including spheroidal, cuboidal, or fan-like. Tertiary γ′ is the finest of the three populations, frequently of nanometric dimensions, and occupies the matrix channels between other γ′ particles. Owing to its extremely small size, it is most readily observed in regions with low density of primary and secondary γ′, such as in the vicinity of grain boundaries. Both secondary and tertiary γ′ typically form during heat treatment rather than during solidification.

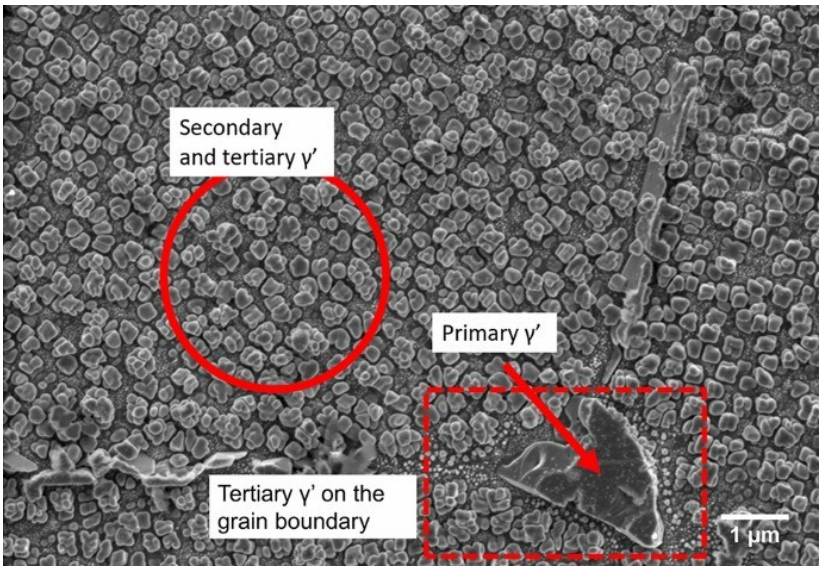

Figure 1.4: Trimodal distribution of γ′ precipitates in Rene 65 *[23]*.

A distinct strengthening phase, designated γ″, is present in certain superalloys, particularly those with elevated Nb contents, such as Inconel 718. This phase has an approximate composition of Ni_3Nb and adopts a body-centred tetragonal crystal structure, rendering it non-coherent with the γ matrix. Although γ″ provides substantial strengthening, it is thermodynamically metastable and transforms to the δ phase upon prolonged exposure to temperatures above 650 °C.

Several categories of carbides may form in nickel-based superalloys, depending on alloy composition and processing conditions. The principal carbide types observed in the microstructure are MC, M_6C, and $M_{23}C_6$.

MC carbides precipitate during solidification through the direct combination of refractory elements, such as Hf, Ta, Ti, and Nb, with carbon and may be found both at grain boundaries and within grain interiors. Their effect on mechanical behaviour depends on their location: grain boundary carbides impede intergranular sliding, thereby enhancing creep resistance, and contribute to the control of grain growth, while intragranular carbides act as obstacles to dislocation motion through a pinning mechanism. Although MC carbides are inherently stable at elevated temperatures, in alloys containing Cr, Mo, or W they may decompose during prolonged exposure in the 700-1000 °C range, forming $M_{23}C_6$ or M_6C according to the following reactions:

$$\gamma + MC \rightarrow M_{23}C_6 + \gamma'$$

$$\gamma + MC \rightarrow M_6C + \gamma'$$

The formation of M_6C is particularly favoured by Mo and W additions. Once formed, M_6C is highly stable at elevated temperatures and, when located at grain boundaries, confers the same beneficial effect on creep resistance as described above for MC carbides.

$M_{23}C_6$ is most prevalent in Cr-rich alloys and is accordingly often approximated as $Cr_{23}C_6$ in composition. Like M6C, it precipitates preferentially at grain boundaries, as can be seen in Figure 1.5, but its thermal stability is confined to the 800–1000 °C range.

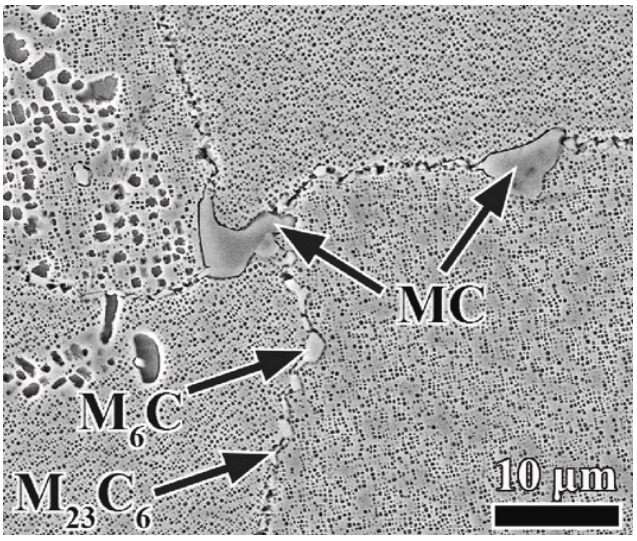

Figure 1.5: Microstructure of different carbides in a nickel-based superalloy *[24]*.

Its mechanical influence is dual in nature: on one hand, the formation of continuous $M_{23}C_6$ films along grain boundaries, is detrimental, as such films embrittle the interfaces, promoting intergranular cracking and reducing tensile elongation [25]. On the other hand, a fine and discontinuous distribution of $M_{23}C_6$ along grain boundaries can pin these interfaces, suppressing both grain boundary sliding and migration and thereby contributing to enhanced creep life [26].

In addition to the phases described above, which generally exert a desirable effect on material performance, brittle phases known as Topologically Close-Packed (TCP) phases may also form. TCP phases derive from intermetallic compounds characterised by a high coordination number and are conventionally grouped into three families: σ phases, η phases, and Laves phases.

The σ phase has an A_xB_y stoichiometry, where x and y range from 1 to 7, and forms preferentially in alloys with elevated Cr and Mo contents. A representative example is $(Cr, Mo)_x(Ni, Co)_y$. The η phase follows an A_7B_6 stoichiometry and can reach considerable compositional complexity, as in $(Co, Fe, Ni)_7(Mo, W, Cr)_6$. Laves phases, with their A_2B formulation, are similarly complex, in some cases incorporating up to eight alloying elements.

The formation of these phases is linked to prolonged exposure to elevated temperatures, conditions under which strengthening phases dissolve and alloying elements segregate locally. They typically adopt an acicular or elongated plate-like morphology and are preferentially located at grain boundaries. Their effect on mechanical properties is strongly negative: acting as stress concentrators, a role directly linked to their sharp, elongated morphology, they become preferential crack nucleation sites, while simultaneously depleting the γ matrix of solid solution strengthening elements. In AM processes, the Laves phase is particularly critical: the strong interdendritic segregation of elements such as Nb and Mo during rapid solidification promotes its formation, drastically increasing susceptibility to hot cracking [19].

1.2.3. Evolution of PM nickel superalloys

The development of powder metallurgy (PM) nickel-based superalloys began in the 1960s, when these materials were first introduced for turbine disc applications in military aeroengines. These alloys were produced to overcome the chemical segregation and structural inhomogeneities inherent to traditional cast-and-wrought processes. Indeed, they offer a more homogeneous microstructure that translates into higher fatigue resistance and yield strength. Their evolution is usually divided into three distinct generations, driven by the demand for improved mechanical reliability and higher operating temperatures, as can be seen in Figure 1.6.

The first generation, represented by René 95, was designed specifically for military turbine discs, where the priority was high stress tolerance at moderate temperatures. The resulting alloys were characterised by a high γ' volume fraction (52-56%) and a fine grain size (around 10 µm). To maintain this fine microstructure, components were generally subjected to sub-solvus heat treatments. This generation achieved a maximum operating temperature of 650 °C [27].

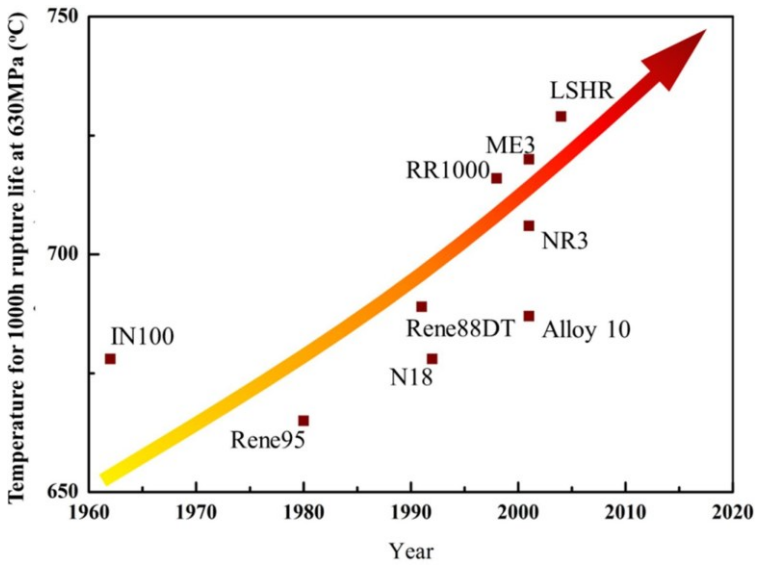

Figure 1.6: Historical development of PM Ni-based superalloys *[28]*.

The second generation, represented by alloys such as René 88DT, focused on damage tolerance and fatigue crack propagation resistance. This is due to meet the demands of civil aviation, like longer service lives and temperatures up to 700 °C. For this purpose, supersolvus heat treatments were adopted to produce grain sizes of around 50 µm. γ' volume fractions were kept lower than in the first generation, largely to avoid cracking during the processing of these coarser microstructures [29].

Third-generation alloys, such as René 104, were developed to push operating temperatures into the 700–750 °C range. These alloys represent a return to high γ' volume fractions, similar to the first generation, but with an approach to grain boundary engineering [30]. Grain sizes were held at around 50 µm to limit creep rates, while cobalt contents increased significantly, reaching up to 21.3% in alloys such as LSHR, and chromium levels were modestly reduced. The content of precipitation strengthening elements Al, Ti, and Nb is between 6% and 13.5%. Furthermore, there is an increased reliance on grain boundary strengthening elements such as carbon and boron. These elements promote the precipitation of carbides and borides, which act as pinning sites to prevent grain growth at high temperatures [31].

Currently, research is focusing on a fourth generation, with 815 °C set as the target operating temperature, alongside goals of high strength, phase stability and low fatigue crack growth. Alloys like GNPM01 lean heavily on refractory elements such as tungsten and tantalum, and early results are encouraging, with creep resistance and maximum operating temperature higher than third-generation standards [32].

1.2.4. AM of Ni-based superalloys

Nickel-based superalloys present significant challenges when processed by conventional subtractive manufacturing techniques. During casting of complex components, γ' precipitates can become coarse or unevenly distributed, reducing mechanical properties.

To limit segregation, successive heat treatments just below the melting temperature are mandatory. Moreover, extensive post-processing is required to reach the final shape. Machining adds another layer of difficulty: high hardness and tendency to work harden make material removal slow and expensive. Consequently, particular attention must be paid to selecting tooling, coolants and parameters, which increases production costs.

Beyond the technical difficulties, conventional processing routes are also highly inefficient from a material utilisation standpoint. The thermomechanical steps involved in turbine component manufacturing typically introduce severe chemical segregation, and the subsequent machining stages generate substantial material waste, with only around 10% of the initial stock ultimately forming part of the finished component [33] [20]. Due to these reason AM has become attractive to the production of Ni-based superalloys components in many sectors.

There are two main process families of AM of Ni-based superalloys: Powder Bed Fusion (PBF) and Directed Energy Deposition (DED) [34]. PBF and in particular PBF-LB has steadily gained prominence both in industry and in the research community, as reflected by the publication trends from Web of Science shown in Figure 1.7. The growing interest in PBF-LB can be attributed to several factors: its high design flexibility, its ability to produce complex geometries and integrated components, and its favourable buy-to-fly ratio. Additionally, LPBF technology enables the adjustment of parameters such as laser power, scan speed, hatch distance and scan strategy. This allows for mechanical properties comparable to those of conventional manufacturing [35].

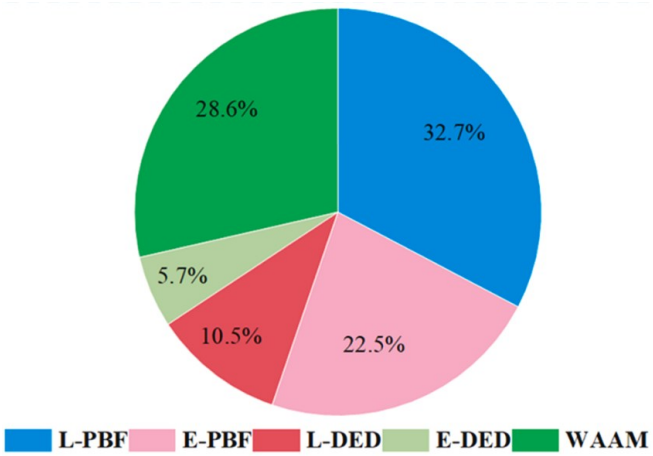

Figure 1.7: Distribution of AM technologies for Ni-based superalloys, based on data from the Web of Science from January 2014 to December 2025 *[20]*.

These advantages come alongside a number of critical challenges, many of which represent active research topics in the additive manufacturing of nickel-based superalloys. A deep understanding of the mechanical properties and their relationship to the resulting microstructure, and in turn to the process parameters, is still needed to bring this technology to a sufficient level of technological readiness. Furthermore,

achieving the mechanical property standards required for industrial applications demands the development of tailored post-process heat treatments.

One of the most significant defect-related challenges in PBF-LB processing is hot cracking, which is closely linked to alloy weldability. This characteristic is commonly quantified by the index Al + 0.5Ti (in wt.%), where values exceeding 3 wt.% conventionally define non-weldable alloys. Based on this index, the widely recognised weldability diagram (Figure 1.8) showing the relationship between Ti and Al content in superalloys was created. As alloy compositions have become more complex, the more complete M_{SAC} index (Al + 0.5Ti + 0.3Nb + 0.15Ta) was introduced, where the coefficients reflect the contribution of each element to γ' formation [36].

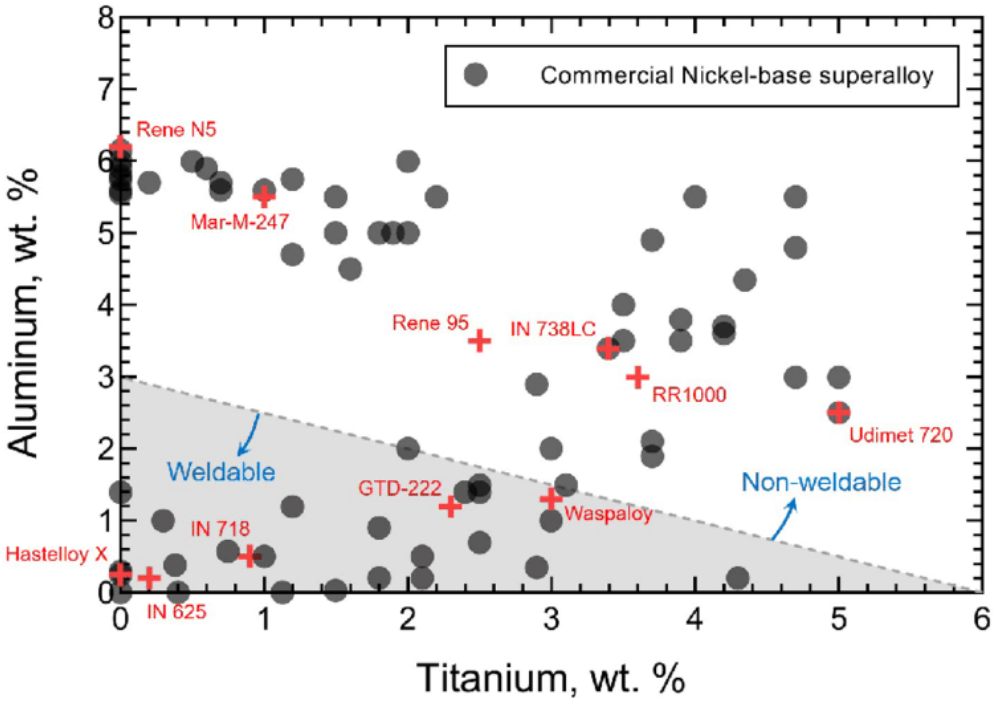

Figure 1.8: Relationship between estimated weldability superalloy and Al and Ti content in Ni-based superalloys *[37]*.

Hot cracking susceptibility is therefore particularly pronounced in alloys containing high concentrations of γ'-forming elements, which tend to segregate into interdendritic regions during the final stages of solidification. Elevated γ' volume fractions also broaden the solidification range and increase the driving force for eutectic formation, thereby exacerbating cracking. Specifically, segregation of these elements into interdendritic regions near the solidus temperature stabilizes thin liquid films that are unable to withstand thermally induced stresses. Moreover, the high cooling rates and thermal gradients in PBF-LB process further increase the level of residual stresses.

To mitigate these issues, modern Ni-based superalloy design often employs a high Ta/Al ratio as a compositional criterion. This approach enables control of the γ' content, as reflected by the M_{SAC} index, and reduces the associated phase

transformation stresses that contribute to cracking. A slight reduction in the γ' fraction and a narrower solidification interval can significantly decrease hot-crack density without compromising high-temperature mechanical performance. In addition, technical advancements in PBF-LB equipment, enabling powder bed preheating, reduce residual stresses and improve crack resistance. Finally, the inclusion could be mitigated by the use of high-quality powder and optimization of process parameters [20].

Another important defect recognized in PBF-LB components is porosity. The porosity can be divided into two main types: spherical pores and lack-of-fusion defects. Spherical pores derive from the gas entrapped in the powders, which could be released during the melting phase of the process. This type of defect could be mitigated by using a higher quality of powder feedstock. Lack-of-fusion defects, by contrast, arise from inadequate wetting between a newly deposited layer and the one beneath it. They are associated with suboptimal process parameters, including laser power, scan speed, hatch spacing, and layer thickness, as well as combined energy input metrics such as Linear Energy Density (LED), Areal Energy Density (AED), and Volumetric Energy Density (VED). Insufficient energy input, reflected in a low VED, prevents proper inter-layer bonding and limits the extent of liquid metal formation, while excessively high VED promotes keyhole defects and spherical porosity [34]. Morphologically, lack-of-fusion defects are distinguished from gas pores by their higher aspect ratio and sharper edges, in contrast to the more rounded geometry of the latter.

1.3. Heat treatments for Ni-based superalloys

The chemical and microstructural complexity of nickel-based superalloys necessitates carefully designed heat treatment (HT) sequences to achieve the target microstructure and properties. These treatments serve several interconnected purposes:

- Increasing the γ' content and homogenising its distribution within the matrix.
- Obtaining the appropriate γ' size and shape for the intended application.
- Promoting carbide precipitation with regular morphologies and favourable spatial distribution, avoiding continuous decoration of grain boundaries.
- Stabilising the desired phases while eventually dissolving detrimental TCP phases formed previously.
- Relieving the residual stresses introduced by the rapid cooling inherent to the process. This consideration is particularly relevant for AM components.

The two stages common to almost all heat treatment sequences for nickel-based superalloys are solution treatment and aging, and a representative schedule is illustrated in Figure 1.9. The starting microstructure, and therefore the appropriate heat treatment strategy, depends on the fabrication route. In cast components, the starting microstructure is typically characterised by irregularly shaped and non-uniformly distributed γ' precipitates. In contrast, components produced by PBF-LB generally lack γ' precipitates in the as-built condition due to the extremely high cooling rates inherent to the process.

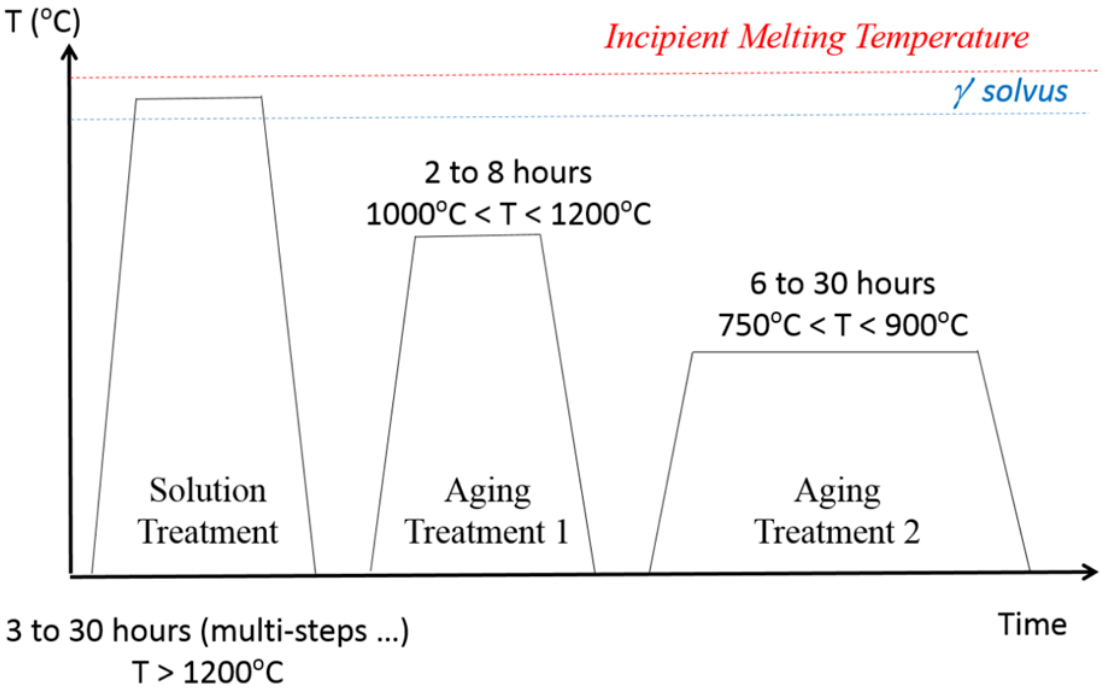

Figure 1.9: Typical heat treatments schedule for a nickel-based superalloy *[38]*.

Solution treatment (also known as homogenisation) involves heating the component to a supersolvus temperature, i.e. above the γ' solvus of the alloy, and holding it there for a period of several hours to achieve complete dissolution of the γ' phase. Temperature control during this stage is critical: it must be high enough to ensure full dissolution yet must not exceed the solidus to avoid incipient melting. This phenomenon refers to localised fusion in microstructurally heterogeneous regions, such as grain boundaries, where the presence of low-melting-point phases causes premature melting before the bulk solidus is reached. Following the hold, the component is cooled at a rate selected to yield the desired γ' volume fraction, size and shape. The primary objective of solution treatment is thus to condition the γ' phase in preparation for the final properties to be developed during aging. In addition, this step can dissolve detrimental Laves phases and excessively coarse carbides that would otherwise impair mechanical performance. The solution temperature also influences recrystallisation and regulates grain size. New trends in solution treatment, involves multiple steps and extended holding times [35].

Aging treatments encompass a wide range of temperatures, durations and step configurations. Consequently, a variety of aging schedules have been reported in the literature. In conventional practice, aging comprises two stages, applied to a starting microstructure consisting of a γ matrix supersaturated with γ'-forming elements. The first aging step is carried out below the γ' solvus to promote the nucleation and growth of secondary and tertiary γ', yielding a more uniform precipitate distribution with a regular cuboidal morphology and wider inter-precipitate channels.

The second aging stage is performed at a lower temperature, typically between 750 and 900 °C. Its primary objective is to relieve residual stresses arising from prior processing steps. At these temperatures, the higher γ' content leads to a narrowing of the matrix channels, which become progressively filled with tertiary γ'. This reduction in channel width restricts dislocation mobility and is known to improve both creep resistance and broader mechanical performance [38]. Recent trends in aging treatments include direct aging, which eliminates the solution step and thereby reduces processing costs [39], and the addition of further aging steps. These supplementary steps aim to optimize carbide microstructure, improve grain boundary characteristics (grain boundary engineering) and apply a thermal barrier coating (TBC).

Despite these advances, a comprehensive and systematic description of heat treatment practices for PBF-LB nickel-based superalloys is currently lacking, making optimization challenging for end-users. In this context, Table 1.2 provides a comparative overview of heat treatment schedules reported in the literature for alloys compositionally similar to SAM, covering fabrication routes including conventional casting, PBF-LB, PBF-EB, and DED-LB. The alloys selected for comparison are IN738, CM247, and MAR-M 247, chosen on the basis of their content of elements partitioning preferentially to the γ matrix and of γ'-forming elements. It should be noted, however, that compositional

similarity does not necessarily imply equivalent microstructural behaviour, and significant differences may still exist between these alloys and SAM.

Table 1.2: Summary of the main heat treatments found in literature for IN738, CM247 LC and MAR-M 247.

Material	**Fabrication method**	**Solution**	**Aging**	**Reference**
IN738 LC	Cast	1120-1220 °C/1-3.5 h, AC-WQ	845 °C/2-48 h, WQ	El-Bagoury [40]
IN738	DED-LB	1120 °C/2 h, AC	850 °C/24 h, AC	Ramakrishnan [41]
IN738	DED-LB	1120-1270 °C/2-8 h, AC	850 °C/24 h, AC	Wang [42]
IN738 LC	PBF-LB	1120-1230 °C/2-4 h, AC	840 °C/24 h, AC	Messè [43]
CM247 LC	Cast	1220-1280 °C/8-16 h, AC	1080 °C/4 h + 870 °C/20 h, AC	Mostafei [44]
CM247 LC	Cast	1220 °C/2h, GQ	770 °C/20 h, FC	Huang [45]
CM247 LC	DED-LB	1232 °C/2 h, GQ	1080 °C/2 h + 870 °C/20 h, AC	Seidel [46]
CM247 LC	PBF-LB	1260 °C/18 h, AC	870 °C/18 h, FC	Divya [47]
CM247 LC	PBF-LB	1205-1245 °C/2 h, GQ	1080 °C/4 h, GQ	Bassini [48]
MAR-M 247	Cast	1185-1270 °C/2-21 h, AC	770-980 °C/1-20 h, AC	Baldan [49]
MAR-M 247	DED-LB	1232 °C/2 h, GQ	1080 °C/2 h + 870 °C/20 h, AC	Seidel [46]
MAR-M 247	PBF-LB	-	870 °C/12 h, AC	Basak [50]
MAR-M 247	PBF-EB	1180-1295 °C/0.5-1 h, AC	1080 °C/4 h + 900 °C/8 h, AC	Ramsperger [51]

AC = Air Cooling, FC = Furnace Cooling, WQ = Water Quenching, GQ = Gas Quenching

In PBF-LB nickel-based superalloys the HIP treatment was added to the conventional heat treatments sequence. HIP and its combination with traditional heat treatment process is nowadays studied and under development by academic and industrial field. HIP consists of subjecting the component simultaneously to elevated temperature and isostatic pressure, typically in the range of 100-200 MPa, using an inert gas such as argon as the pressure-transmitting medium. The combination of heat and pressure

promotes the closure and healing of internal defects, such as the gas pores and lack-of-fusion voids that are inherent to the PBF-LB process. This densification effect is one of the primary motivations for introducing HIP in the processing of AM components, as residual porosity is known to act as a stress concentrator and a preferential site for fatigue crack initiation, significantly reducing the fatigue life of the component.

Beyond defect healing, HIP at sufficiently high temperatures also promotes microstructural homogenisation, contributing to a more uniform distribution of alloying elements and phases. When performed at supersolvus temperatures, HIP can simultaneously dissolve the γ' phase and close internal defects in a single step. This approach, often referred to as supersolvus HIP, has attracted considerable interest in both the academic and industrial fields.

Despite its potential, HIP requires further development to close the knowledge gap between processing parameters and microstructural outcomes. The influence of temperature, pressure, and holding time on the resulting microstructure is complex and remains an active area of research. The optimal parameter combination must be carefully established to achieve full densification and the desired microstructural state, while remaining below the solidus temperature to avoid incipient melting, which would introduce detrimental defects and compromise the integrity of the component.

1.4. Outline of the novel Ni-based superalloy

1.4.1. Design requirements and performance targets

The efficiency of modern gas turbines is closely linked to the ability of materials to withstand extremely high operating temperatures. In this context, SAM alloy was developed specifically for PBF-LB components used in the hot gas pathway of gas turbines, where thin-walled or geometrically complex designs make additive manufacturing the only viable production route. During alloy development, an average operating temperature in the range of 700-750 °C was targeted, with the ability to sustain peaks up to 1000 °C.

To meet these requirements, specific performance benchmarks were established. In terms of creep rupture resistance, the component must pass testing at 850 °C under loads between 170 and 230 MPa for a minimum of 100 to 400 hours, with loading applied in the most critical direction, perpendicular to the build layers. In addition to creep resistance, adequate oxidation resistance is required. Chromium serves as the primary oxide-forming element, generating a protective Cr_2O_3 surface layer stable up to approximately 900 °C. The use of Cr rather than Al as the primary oxide former is a deliberate design choice: a sufficiently high Al content to promote Al_2O_3 layer formation cannot be achieved without increasing susceptibility to strain age cracking (SAC). The Cr content is nevertheless limited by the risk of TCP phase formation and other undesired phase instabilities [52].

In terms of oxidation performance, the alloy occupies an intermediate position between classic Cr_2O_3-forming alloys such as IN939 and IN738LC, which exhibit mass increases of 2-3 mg/cm² after 3000 hours of isothermal testing, and pure Al_2O_3-forming alloys, which show mass increases of approximately 0.4 mg/cm². Under cyclic oxidation conditions, consisting of alternating exposures at 950 °C for 23 hours and room temperature for 1 hour over a total of 3000 hours in air, the alloy exhibits a mass increase of 0.9-2 mg/cm², a more demanding test condition than isothermal exposure. Considering that the Al content is the primary factor governing SAC susceptibility, there will hardly be any other alloy that combines such good oxidation resistance with low SAC susceptibility [53].

1.4.2. Chemical design and processability

Alloys processed by PBF-LB have traditionally been adaptations of existing cast superalloys, such as IN738LC, which were originally optimized for processes with low cooling rates and are conventionally considered poorly weldable. When processed by PBF-LB, these alloys tend to form cracks both during solidification and during subsequent heat treatment, in the form of hot cracking and strain age cracking respectively.

SAM departs from this tradition through a clean-sheet design approach: rather than applying incremental modifications to an existing alloy, its chemical composition was developed from scratch with the extreme thermal cycles of AM explicitly considered. The primary objective was to achieve an alloy that combines good processability with high mechanical performance.

SAM addresses this limitation directly: unlike modified conventional alloys, which sacrifice mechanical and creep resistance to gain weldability, SAM is capable of combining PBF-LB processability with properties comparable to those of IN738LC. The typical trade-off between creep capability and SAC in nickel-based superalloys is observable in Figure 1.10.

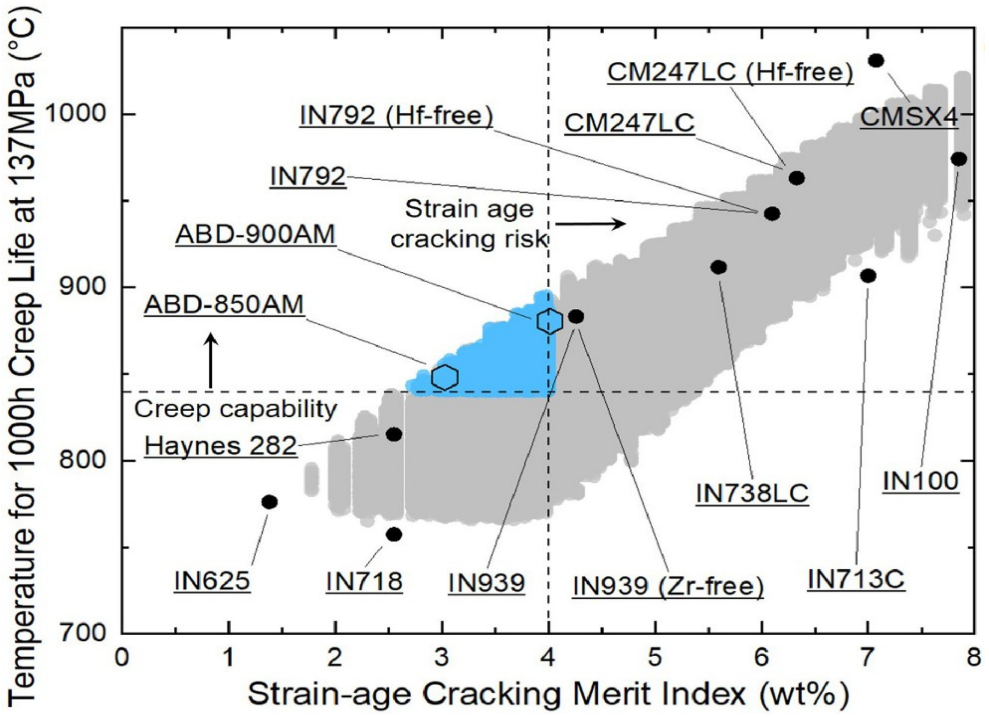

Figure 1.10: Diagram representing strain-age cracking index and its relationship to creep resistance *[54]*.

Tantalum plays a central role in the design of this superalloy. As a γ'-forming element characterised by low diffusivity in nickel, Ta significantly slows the precipitation kinetics of the γ' phase compared to other γ'-forming elements, which is particularly advantageous in controlling phase evolution during processing. A sufficiently high Ta/(Al, Ti, Nb) ratio effectively decelerates the overall precipitation kinetics, enhancing resistance to SAC. If this ratio is too low, γ' precipitation proceeds too rapidly, increasing the likelihood of SAC-related failure. Conversely, an excessively high ratio may promote the formation of detrimental TCP phases, compromising microstructural stability.

The Ta content also governs the stability of carbide phases through the Ta/C ratio, which is maintained between 250 and 700 (by weight) in the alloy design. This range ensures a sufficient volume fraction of TaC as the primary MC carbide, while limiting

the amount of free carbon available to form $Cr_{23}C_6$. During elevated-temperature exposure, TaC becomes metastable and progressively transforms into $Cr_{23}C_6$, which precipitates as continuous grain boundary films and deteriorates creep resistance. A higher Ta/C ratio slows this transformation by reducing the driving force for $Cr_{23}C_6$ formation [53].

The strategy of intentionally slowing γ' precipitation kinetics necessarily results in a comparatively reduced Al content, which leads to a lower γ' volume fraction during AM and the early stages of subsequent heat treatments. As a consequence, the intrinsic stresses generated during the AM process can partially relax before being compounded by the additional stresses associated with γ' formation, thereby mitigating the risk of SAC.

Cobalt also contributes significantly to this alloy design. Co promotes the partitioning of Ta from the γ matrix into the γ' phase, increasing the γ' content and compensating for the intentionally reduced concentrations of other γ'-forming elements. This redistribution enhances the γ/γ' lattice mismatch, which in turn contributes to strengthening through improved precipitation hardening.

Minor elements such as boron, carbon, and zirconium, play an important though carefully balanced role. Boron is detrimental to hot cracking susceptibility at higher contents, but beneficial for SAC resistance and high-temperature ductility through intrinsic grain boundary strengthening, an effect that operates even in the absence of oxygen. Zirconium, by contrast, does not worsen hot cracking but slightly increases SAC susceptibility; it nevertheless improves stress-rupture life and notch resistance at high temperatures, likely through sulphur binding and protection of grain boundaries against oxygen attack during service. Carbon is kept at low levels (0.001-0.03 wt.%) to limit the volume fraction of TaC at grain and cell boundaries, which otherwise raises residual stress and promotes SAC initiation. A small addition of yttrium (below 0.06 wt.%) further contributes to oxidation resistance by promoting the formation of a more adherent and stable oxide scale [52].

Given that the present work is focused on heat treatments, the susceptibility of the material to SAC is of particular relevance. A preliminary comparison of SAM with other nickel-based superalloys was therefore carried out using the MSAC index. The diagram in Figure 1.11 plots the Al weight fraction on the x-axis against the combined contribution of the other γ'-forming elements, weighted by their respective coefficients, on the y-axis. The threshold line corresponding to MSAC = 4, above which materials become susceptible to SAC, is also indicated [36].

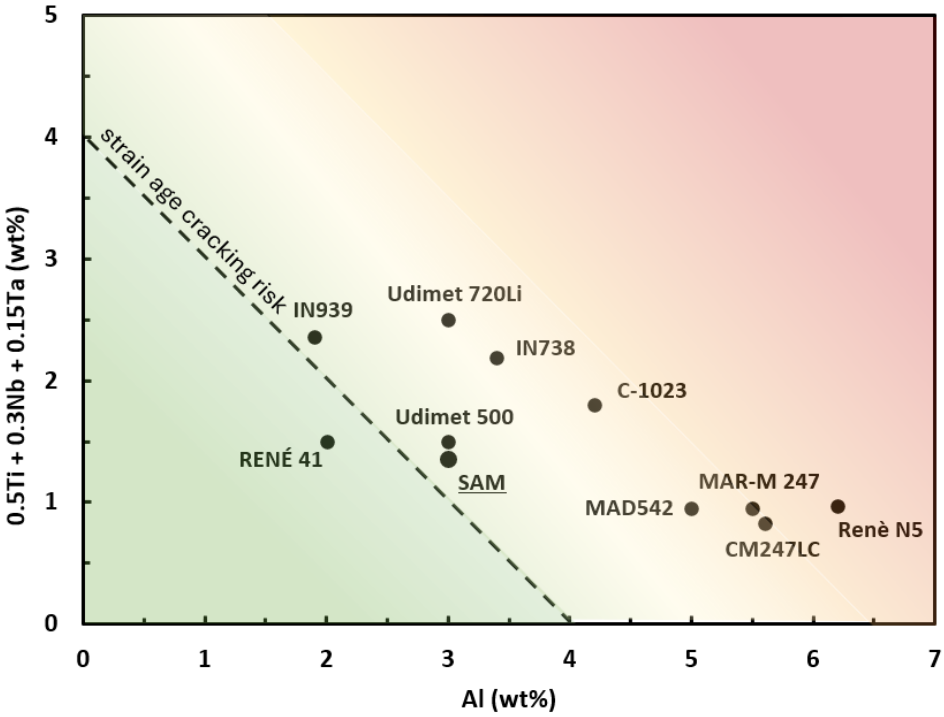

Figure 1.11: Weldability diagram based on the MSAC index.

It is worth noting that recently some alloys positioned over this threshold, such as CM247 LC and MAD542, have been successfully processed without cracking, though this required considerable effort and was only made possible through extensive optimization of printing parameters. SAM exhibits a notably lower MSAC index than these materials and, although it lies slightly above the threshold line, its susceptibility to SAC is substantially reduced.

A more comprehensive assessment of weldability was carried out using the diagram shown in Figure 1.12, adapted from the work of Basak [55] [56]. In the original diagram, only Ti and Al were included on the y-axis; in the present work, this axis was replaced by the MSAC index, which incorporates the contributions of Ta and Nb in addition to Al and Ti, ensuring that all γ'-forming elements are accounted for. The x-axis was retained from the original. The boundary lines dividing the weldability fields were also taken from the original diagram: the lower line passes just below alloys such as René 41 and IN939, the middle line passes through the region occupied by IN738, and the steepest line, marking the boundary of the non-weldable field, passes through MAR-M 247 and CM247 LC. The validity of these boundaries was verified by cross-referencing the weldability classifications of the alloys shown with data reported in the work of Basak, where available.

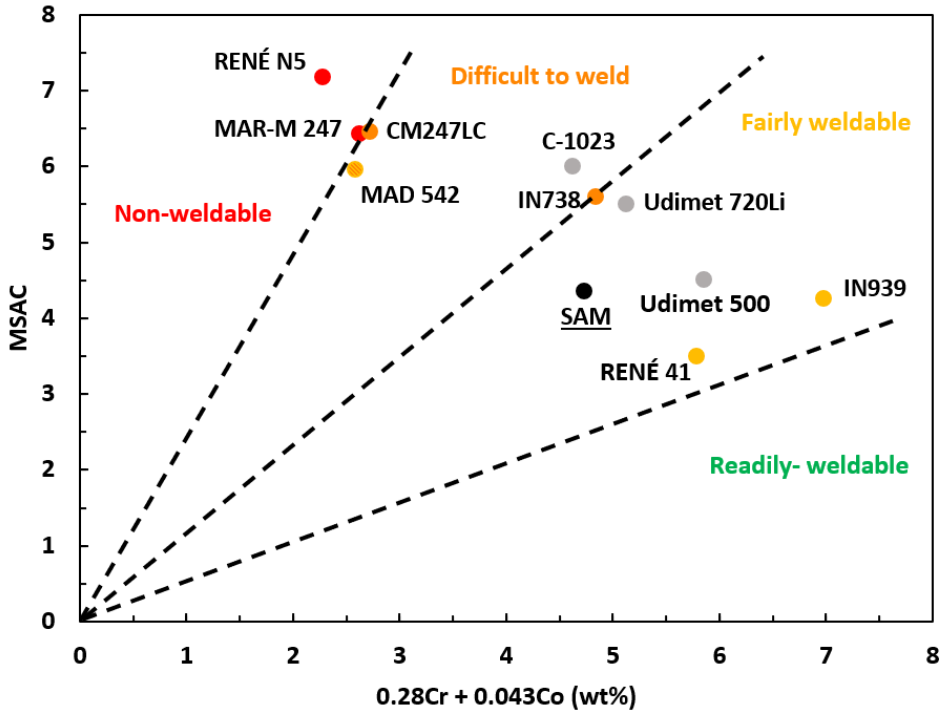

Figure 1.12: Modified weldability diagram based on MSAC and Cr + Co content.

Based on this diagram, SAM falls within the fairly weldable field, indicating a good processability potential compared to other high γ' content nickel-based superalloys such as CM247LC and IN738, which are positioned in the difficult-to-weld or non-weldable regions.

An important role in the processability and reduction of SAC is played by hafnium. During solidification following the printing process, Hf promotes the formation of an intermetallic phase that sequesters γ'-forming elements, particularly Ta and Al, from the matrix, reducing their local concentration. During the subsequent heating phase of solution treatment, the presence of this intermetallic slows the precipitation kinetics of γ', preventing the rapid phase formation that would otherwise drive SAC. Furthermore, when the temperature is sufficient to promote grain growth, the intermetallic phase regulates this process through a mechanism known as strain-induced grain boundary movement (SIBM), producing a coarse-grained final microstructure with grain growth ratios that can exceed five times the initial size. This coarse microstructure confers exceptional resistance to viscous flow at elevated temperatures.

Once the temperature exceeds the γ' solvus, the intermetallic dissolves into the matrix, releasing Al and Ta and increasing their concentration. Upon cooling from the solution treatment, this elevated solute content translates into a high γ' volume fraction. The mechanism is illustrated schematically in Figure 1.13, which highlights the difference in microstructural evolution between composition with and without Hf.

Despite these advantages, the use of Hf requires precise compositional control. Concentrations above approximately 2-3% can render the intermetallic phase

excessively stable and insoluble, leading to the formation of a continuous film along grain boundaries that embrittles the microstructure and negates the benefits in terms of weldability and mechanical performance, as discussed in the previous section [53].

Beyond its role in processability, Hf also contributes to oxidation resistance. In ternary alloy systems, a continuous Al_2O_3 protective layer at 1000 °C in air typically requires at least 10% Cr and 5% Al. In Hf-containing alloys, however, a continuous and dense alumina layer forms even at Al contents as low as 3%, representing a significant advantage for alloys where high Al concentrations are deliberately avoided to limit SAC susceptibility. Finally, the Hf content, together with Mo and W, has a strong influence on the solution treatment window. A careful balance between these elements has therefore been established to ensure a sufficiently wide temperature interval between the γ' solvus and the solidus, which is essential for robust and reproducible heat treatment processing.

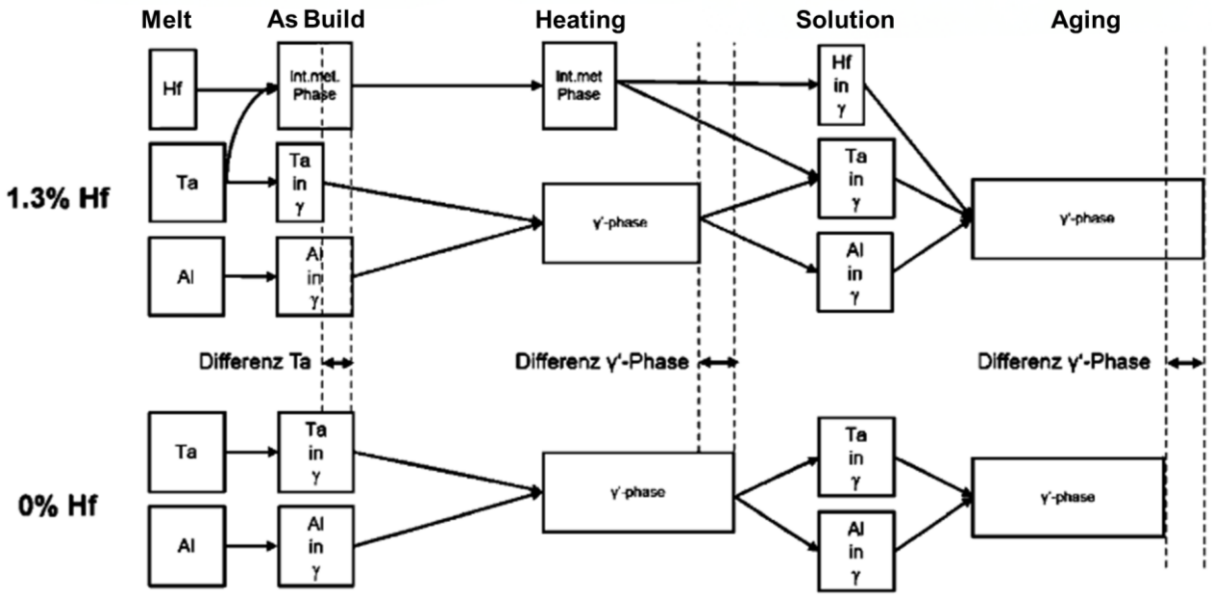

Figure 1.13: Effect of Hf in the different stages of SAM processing *[53]*.

2. Materials and methods

2.1. Differential Scanning Calorimetry (DSC)

The DSC was performed on samples of an approximate dimension of 3x3x9 mm. The average weight of the samples is 478 mg. The DSC instrument used for the analysis is the Setaram LabSys Evo.

The guidelines used for taking the characteristics temperature are taken from the work of Migas et al. and the NIST recommended Practice Guide "DTA and Heat-flux DSC Measurements of Alloy Melting and Freezing" [57] [58].

All the curves obtained by DSC were then analysed using Fityk software, which makes it possible to obtain all the characteristic temperatures and deconvolute peaks using its fitting tool. In particular to analyze the single peak, the following process was adopted:

1. Select the range to be analysed and isolate the peak using the "Data-Range Mode" function.
2. Setting of the baseline, using the "Baseline Mode". In all the case the baseline was built using the two extremities of the range, where the curve returns from the peak to the line. All the baselines were imposed as linear functions.
3. Flattening of the base of the peak using the "Strip background" function on the baseline.
4. Add the peak function using "Add-Peak Mode". Gaussian functions were used to build the peak functions.
5. Fitting of the added peaks on the curve using the "Start fitting" function. Manual modification of the peak parameters (height, centre and HWHM) is used to adjust the fit if necessary.
6. Verify that the added peak fits the curve properly through auxiliary plot 1, where the built peaks are subtracted from the DSC curve. A completely flat line indicates a perfect fit.

2.2. Heat treatments

Cubic samples of the novel nickel-based superalloy SAM, manufactured using PBF-LB on an EOS M290 system, were provided by Siemens Energy AB for the experimental work. These samples, referred to as 'as-built', were then subjected to three different heat treatment steps (HIP, solution and aging), which represent the topic of the thesis. The first part of the trials (Table 2.1) involved the HIP and solution steps (air cooling), with the aim of analysing the impact of the treatments on the microstructure and confirming the optimal solution temperature range. The Hot Isostatic Pressing (HIP) process was carried out using a Quintus Technologies QIH 15L unit at a fixed pressure

of 100 MPa with a holding time of 4 hours; cooling was performed within the unit at a controlled rate of 20 °C/min. Solution treatment in this first series was performed in a Nabertherm N120/85HA furnace.

Table 2.1: First stage of thermal treatments trials.

Sample	**HIP**	**Solution**		
	Temperature (°C)	**Temperature (° C)**	**Time (h)**	**Cooling**
HIP STD SOL 1140-1	1180	1140	1	Air
HIP STD SOL 1140		1140	4	Air
HIP STD SOL 1170		1170	4	Air
HIP STD SOL 1220		1220	4	Air
HIP STD SOL 1230		1230	4	Air
HIP STD SOL 1240		1240	4	Air
HIP STD SOL 1260		1260	4	Air
HIP 1220 SOL 1220	1220	1220	4	Air
HIP 1220 SOL 1230		1230	4	Air
HIP 1240 SOL 1220	1240	1220	4	Air

Following the identification of the optimal heat treatment window for the combination of HIP and solution (air cooling), a second cycle of trials (Table 2.2) was conducted, focusing on the optimal solution temperature (i.e. 1220 °C), but using furnace cooling instead of air cooling. This type of cooling is notably slower, indeed in this case was decided to fix a cooling rate of approximately 40 °C/min. The three different solutioned samples relate to the three different HIP treatment temperatures. The treatments were performed in TAV MiniJet HP235 vacuum heat treatment furnace, equipped with a thermocouple to check the cooling rate during the process.

Table 2.2: Second stage of thermal treatments trials.

Sample	**HIP**	**Solution**		
	Temperature (°C)	**Temperature (° C)**	**Time (h)**	**Cooling**
HIP STD SOL 1220-S	1180	1220	4	Furnace
HIP 1220 SOL 1220-S	1220	1220	4	Furnace
HIP 1240 SOL 1220-S	1240	1220	4	Furnace

Following this stage, an aging trial was conducted (Table 2.3) to investigate the effect of aging temperature on the resulting microstructure. Five different temperatures were tested, all applied to samples previously processed with the parameter combination that yielded the best outcome in the preceding stage, namely HIP and solution treatment both performed at 1220 °C, the latter followed by furnace cooling. Aging was carried out in a Nabertherm N120/85HA furnace, with air cooling applied after the treatment, given the negligible influence of cooling rate in this phase.

Table 2.3: Third stage of thermal treatments trials.

Sample	**HIP**	**Solution**	**Aging**	
	Temperature (°C)	**Temperature (° C)**	**Temperature (° C)**	**Time (h)**
AG 600	1220	1220	600	4
AG 800			800	4
AG 975			975	4
AG 1000			1000	4
AG 1025			1025	4

2.3. Metallographic preparation

All the heat-treated cubic specimens were cut into two sections (the XZ and XY planes) using a Remet MT60 cut-off machine with a double lubricant jet. The metallic samples were then embedded in phenolic resin with a Hergon MI30 encapsulating press at a temperature of 160 °C for 20 minutes. The samples obtained were then prepared using Presi Mecatech 234 polishing machine with the process described in Table 2.4.

Table 2.4: Stages and parameters used for the metallographic preparation.

Stage	**Time (s)**	**RPM disk**	**RPM head**	**Force (kN)**
SiC foil 80	120	150	100	1.5
SiC foil 180	120	150	100	1.5
SiC foil 500	120	150	100	1.5
SiC foil 600	120	150	100	1.5
SiC foil 800	120	120	100	1.2
SiC foil 1000	120	120	100	1.2
SiC foil 1200	120	120	100	1.2
Pad 3 µm + suspension	300	120	80	0.75
Pad 1 µm + suspension	300	120	80	0.75
Silica suspension	180	80	60	0.75

After the metallographic preparation stage, the specimens designated for microstructural analysis were electrolytically etched with orthophosphoric acid (H_3PO_4) at 2.5 V. This etching procedure selectively attacks the γ matrix, leaving other phases such as γ' and carbides in relief.

Electrolytic etching also proved particularly effective for grain size measurements, and in samples with coarser microstructures or large phases it serves as a valuable technique for preliminary observation. Furthermore, the gradient etching effect arising from the spatial variation in current density relative to the electrode position allows a wide range of etching conditions to be explored, making it possible to identify the optimal contrast for each sample. A representative example of the etched microstructure is shown in Figure 2.1.

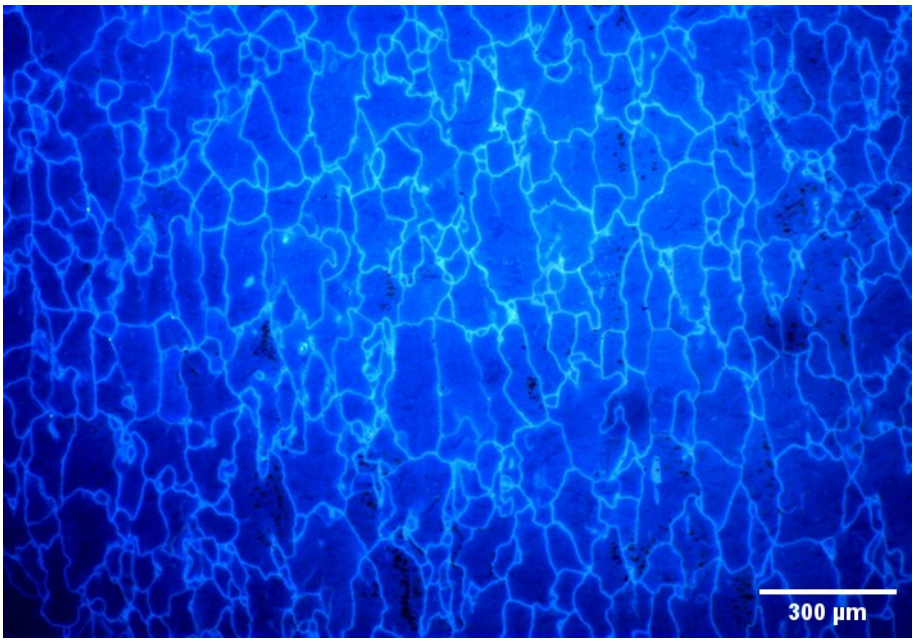

Figure 2.1: Light optical micrograph of an electrolytically etched specimen.

2.4. Hardness

Hardness provides a useful indication of the mechanical properties of a material and can be directly correlated with yield strength. It is measured by means of an indentation test, in which a non-deformable indenter of a defined geometry is pressed into the material surface and the resistance to penetration is quantified. Several hardness scales exist, each associated with a specific indenter geometry and loading conditions, including the Brinell, Vickers, and Rockwell scales.

Hardness measurements were performed using an Emcotest M4U 035 durometer, an instrument that supports a wide range of indentation systems and hardness scales. In this work, the Brinell hardness test was adopted in accordance with the ASTM E10-23 standard [59]. The test employs a spherical tungsten carbide (WC) indenter with a diameter of 2.5 mm, loaded with a force of 62.5 kg, defining the HB10 hardness scale.

Upon indenter removal, a near-circular residual imprint is left on the specimen surface, the diameter of which reflects the extent of penetration and thus the hardness of the material. Two diameter measurements were taken for each indentation, and their average was computed automatically by the instrument and used as input to the Brinell hardness formula:

$$\mathrm{HB10} = \frac{F}{A} = \frac{2F}{\pi D \cdot \left(D - \sqrt{D^2 - d^2}\right)}$$

where F is the applied load, A is the projected surface area of the imprint, D is the indenter diameter, and d is the measured imprint diameter. A schematical diagram of the test, with the output parameters is represented in Figure 2.2. Five measurements were performed on each of the samples analyzed.

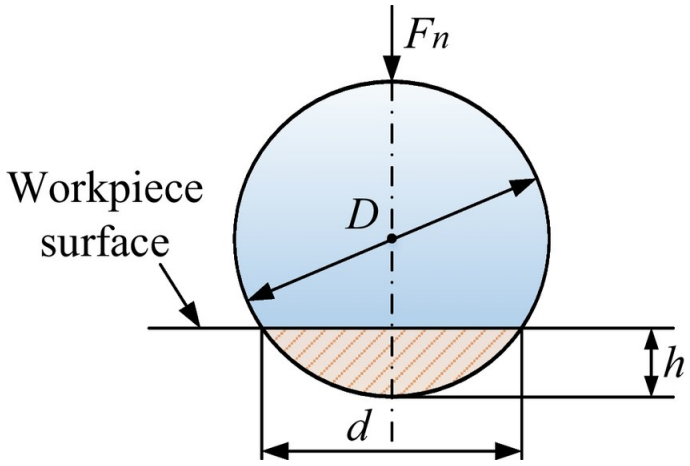

Figure 2.2: Diagram of indentation for Brinell test. *[60]*

2.5. Light Optical Microscope (LOM)

Light optical metallographic microscope LEICA MEF4 M was used to observe the microstructure of the material in electrolytical etched conditions. The instrument offers selectable magnifications of 50x, 100x, 200x, 500x, and 1000x, enabling observation across multiple length scales. In particular, it was used to take the images necessary for measuring the grain size and for an initial check of some samples prior to Scanning Electron Microscopy (SEM) or Field Emission Scanning Electron Microscope (FESEM) observations. This initial check primarily involves detecting defects, such as shrinkage porosity, lack of fusion and defects resulting from the formation and subsequent solidification of liquid. LOM is well suited to this role, as it provides rapid, high-contrast imaging of surface features without the preparation demands of electron-based techniques.

2.6. Scanning Electron Microscope (SEM)

A Zeiss Evo 15 scanning electron microscope (SEM) equipped with an Oxford Instruments Ultim Max 40 EDS detector was used for microstructural examination and semi-quantitative elemental analysis. Imaging was performed using secondary electrons (SE) when the focus was on surface morphology, and backscattered electrons (BSE) when phase identification was required. Magnifications ranging from 5,000x to 50,000x were selected according to the size of the microstructural features of interest and the purpose of the image, whether an overview or a detailed view of grain boundaries or specific phases.

The EDS detector was employed to assess the composition of individual phases where their size permitted reliable analysis. EDS is inherently semi-quantitative, with two main limitations: detection sensitivity, which makes light elements difficult to quantify accurately, and spatial resolution, which restricts analysis to features above a certain size threshold. Despite these limitations, it provides valuable compositional information at the micrometric scale, allowing the nature of precipitates and the approximate composition of the alloy matrix to be determined.

Prior to SEM analysis, a thin gold coating was deposited on the sample surface by sputter coating to enhance electrical conductivity, as the resin surrounding the mounted specimen is non-conductive. This step is essential to prevent charge accumulation during observation, which would otherwise distort the image and risk damaging the sample. The coating was applied using an Agar Auto Sputter Coater, in which the sample is placed inside a small vacuum chamber. Argon gas is introduced and ionised into a plasma state by applying a high voltage between two electrodes, with the gold target acting as the cathode and the sample as the anode, causing gold atoms to be ejected and deposited as a uniform thin film on the sample surface.

A Zeiss Merlin Field Emission Scanning Electron Microscope (FESEM) was also used in this study. Unlike conventional SEM, FESEM relies on a field emission gun (FEG) to generate a finer and more coherent electron beam, which translates into higher spatial resolution and improved performance at low accelerating voltages. This makes it the appropriate choice for resolving fine microstructural features such as tertiary and the finest secondary γ' precipitates, which fall below the resolution limit of conventional SEM. The instrument can reach resolutions down to 0.4-1 nm and typically operates between 0.1 and 3.0 kV, keeping beam-induced damage to a minimum. More broadly, the combination of high resolution and analytical capability makes FESEM a valuable tool for grain boundary analysis, nanoparticle imaging, and defect identification in advanced materials. In this study, however, all images were acquired in secondary electron mode, as the analyses were focused on γ' precipitate morphology, with magnifications ranging from 50,000x to 500,000x.

2.7. Image analysis

ImageJ software was used for image analysis of grain size, secondary γ' size, and volume fraction. Grain size measurements were performed on images taken on optical microscope, while γ' size and volume fraction analyses were carried out on SEM or FESEM images, depending on the size of the precipitates.

Grain size measurement, applied to the build direction in this work, was performed in accordance with ASTM E112-25 guidelines using the intercept method. This technique involves counting the number of grain boundary intersections along a test line of known length, from which the mean lineal intercept length is derived. The precision of the method is a function of the number of intercepts or intersections counted. Since reliable counts can be obtained without marking individual intercepts or intersections, the intercept method provides faster measurements than the planimetric method for an equivalent level of precision. Ten measurements were performed per sample [61].

The analysis of γ' size and volume fraction required a more involved image processing procedure, carried out through the following steps:

1. Measurement of the scale segment.
2. Adjusting the brightness and contrast depending on the image characteristics.
3. Selecting the better fitting model for the image, in order to distinguish γ' from the γ matrix. In this work, Li and Intermodes models are predominantly used.
4. Application of the "Fill Holes" and "Watershed" effects. The former fills the inner part of the γ' particles that the model was unable to detect, while the latter divides particles that are overimposed.
5. Setting the minimum threshold diameter for γ' particles.
6. Application of the "Analyze particles" tool to extrapolate data on the area, major and minor axes of single particles, γ' volume fraction and its average area across the entire image.

In images where low contrast between the γ and γ' phases prevented reliable thresholding using models implemented in ImageJ, an alternative approach was adopted in accordance with ASTM E562-19e1. In this method, a regular square grid of points is superimposed onto the image, and the number of points falling within the phase of interest is counted and divided by the total number of points, yielding the point fraction for that field. The average point fraction over n analysed fields provides an estimate of the volume fraction of the constituent. This technique is suitable only for bulk, opaque, planar sections examined by reflected light or electron imaging [62].

3. Results and discussion

3.1. Thermal analysis of the alloy

In the initial phase of the project, eight different DSC runs were carried out (see Table 3.1) to improve the design of the thermal treatment. Moreover, it enables a more in-depth understanding of the phase transformations that would occur. The information obtained was fundamental in determining the optimal temperature window for the solution and aging treatments.

Table 3.1: DSC analyses conducted.

DSC n.	**Sample**	**Weight (mg)**	**Run**	**Heating speed (°C/min)**	**Cooling speed (°C/min)**
1	As-built n. 1	450.6	1	20	20
2	As-built n. 2	486.8	1	10	10
3	As-built n. 3	494.4	1	20	40
4	As-built n. 3	494.4	2	20	40
5	HIP STD n. 1	457.9	1	20	20
6	HIP STD n. 1	457.9	2	20	20
7	HIP STD + SOL 1230° C	535.8	1	20	20
8	HIP STD + SOL 1260° C	446.1	1	20	20

The first three samples analysed were all in the as-built state. The main reason for carrying out three runs was to obtain data for estimating a CCT curve of γ' precipitation using three different cooling rates. Furthermore, additional checks were done on phase transformations during heating at two different speeds (as it is not possible to reach 40 °C/min in the heating stage).

DSC n. 4 was performed to check for any differences in the as-built n. 3 sample after the first DSC cycle, i.e. above its melting temperature. So, the analysis of the phases resulting from the solidification of the liquid was made possible by this.

DSC runs n. 5 and n. 6 are similar to the previous ones but were performed on the HIP STD n. 1 sample to check for differences from the as-built samples. The last two runs,

however, were conducted on post-solution samples to control the formation of new phases that result in additional transformations in the thermogram.

As there is no information about SAM in the literature, it was decided to consult the DSC curves of similar materials in order to confirm the different peaks. Similar compositions were identified in Inconel 738 LC, CM247 LC and MAR-M 247 superalloys.

3.1.1. As built samples analysis

The DSC heating curves in Figure 3.1 shows three different peaks. The first peak, at around 610 °C, is related to γ' formation. Indeed, in the L-PBF process, cooling is so rapid that γ' does not have time to form, as confirmed by Schulz et al. [63]. Therefore, when the sample is heated during the DSC test, precipitation occurs. This is confirmed by the fact that this peak is visible only in DSC curves involving first runs of as-built samples.

The change in heat flow between 1140 °C and 1170 °C can clearly be identified by the typical sigmoid shape of γ' dissolution, with an approximate onset temperature of 1148 °C and an approximate endset temperature of 1160 °C.

By observing the final melting peak, we can determine the solidus and liquidus temperatures, which are located at 1225 °C and 1390 °C, respectively. The solidus temperature is particularly interesting in this case, because it determines the temperature at which incipient melting will begin during heat treatment. The value found is similar to that reported in the literature for Inconel 738 LC [64].

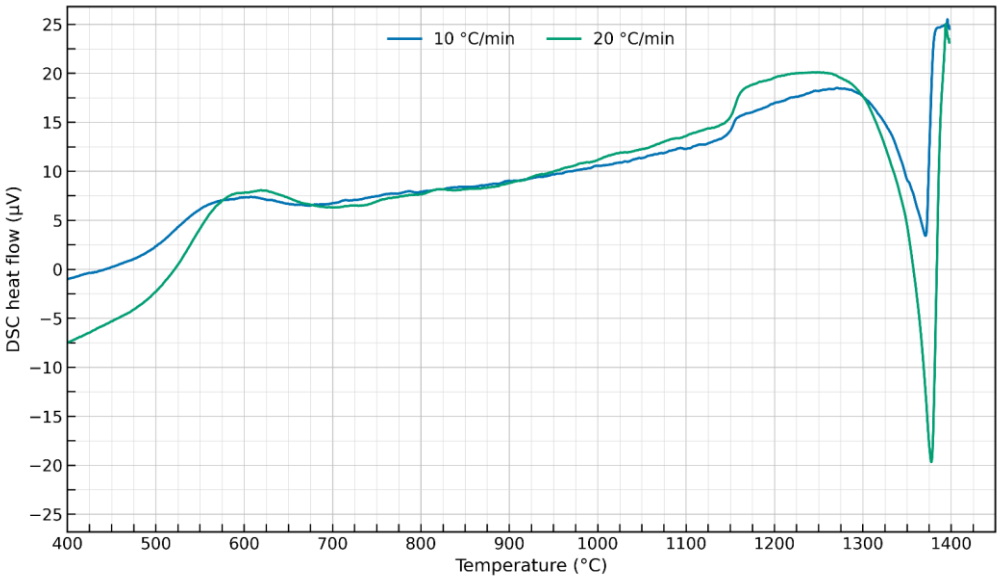

Figure 3.1: DSC analysis of the heating curve on the as-built samples at different heating speeds.

Following the hold at 1400 °C, the cooling curve shown in Figure 3.2 was recorded. The first peak observed corresponds to solidification and allows the liquidus

temperature to be determined with greater accuracy than during heating, as established by Migas et al. [57]. A liquidus temperature of 1370 °C was identified. The solidus temperature was also determined from the cooling curve, yielding results consistent with those obtained from the heating analysis.

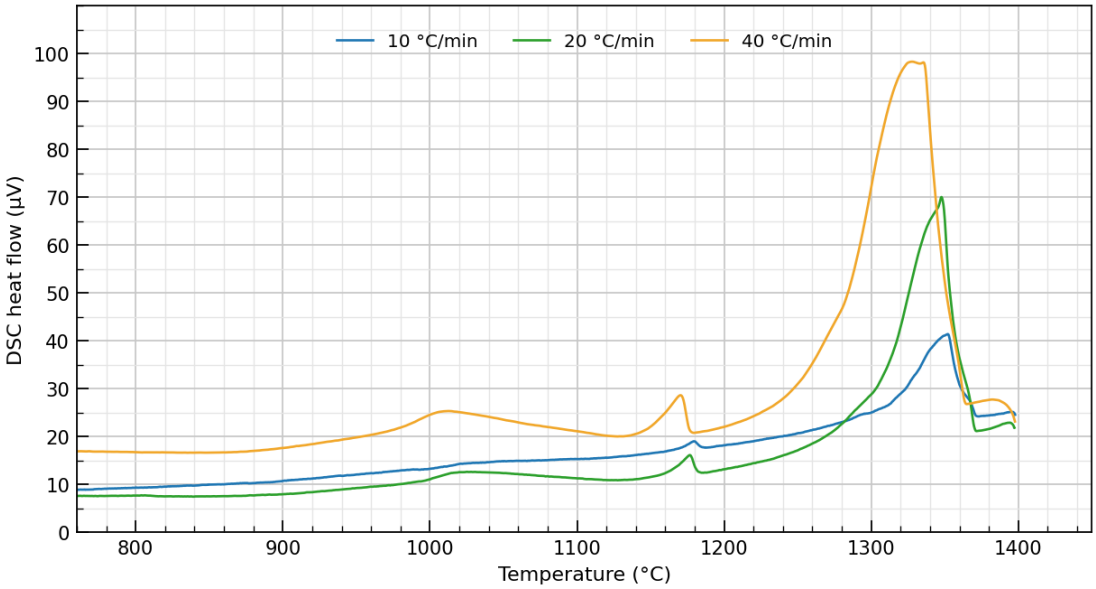

Figure 3.2: DSC analysis of the cooling curve on the as-built samples at different cooling speeds.

Subsequently, given the shape of the peak, it was decided to deconvolve this peak into three different curves using Fityk (Figure 3.3). Indeed, the peak has two different shoulders in addition to the main peak, and deconvolution with two curves did not produce satisfactory results. This analysis appears to be correct because the typical solidification sequence of Inconel 738 LC involves three stages, and is described as follows:

$$\mathrm{L} \rightarrow \mathrm{L} + \gamma \rightarrow \mathrm{L} + \gamma + \mathrm{MC} \rightarrow \gamma + \mathrm{MC} + \text{eutectic } (\gamma + \gamma') \text{ [65]}$$

In addition, all these phases were observed in the regions where the material melted, as can be seen in the SEM analyses on post DSC samples. Basing on literature it was determined that the first deconvolved peak was attributed to the γ' formation, the second peak to the MC carbide formation, and the final peak to the eutectic formation.

Following the solidification process, the peak at around 1180 °C indicates the γ' precipitation, which was detected at a slightly higher temperature than that indicated by the heating curve. Furthermore, the position of this peak depends on the cooling rate. Starting from the evaluation of the onset and endset of the transformation, the decision was made to construct the CCT curve (Figure 3.4), with γ' start and γ' finish from three different cooling rates. This graph was useful for evaluating γ' precipitation during slow cooling after solution heat treatment, which was performed in the final stage of the solution trials.

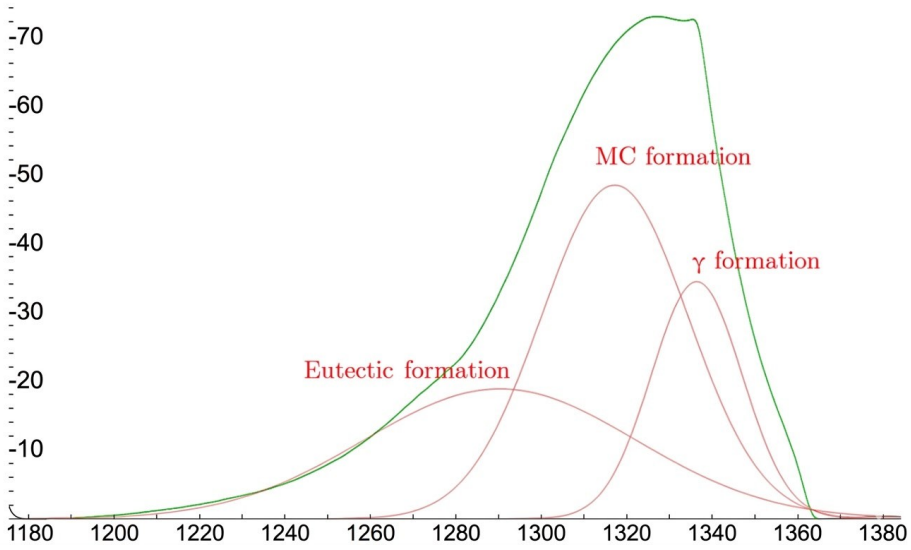

Figure 3.3: Deconvolution of solidification peak of DSC in Fityk.

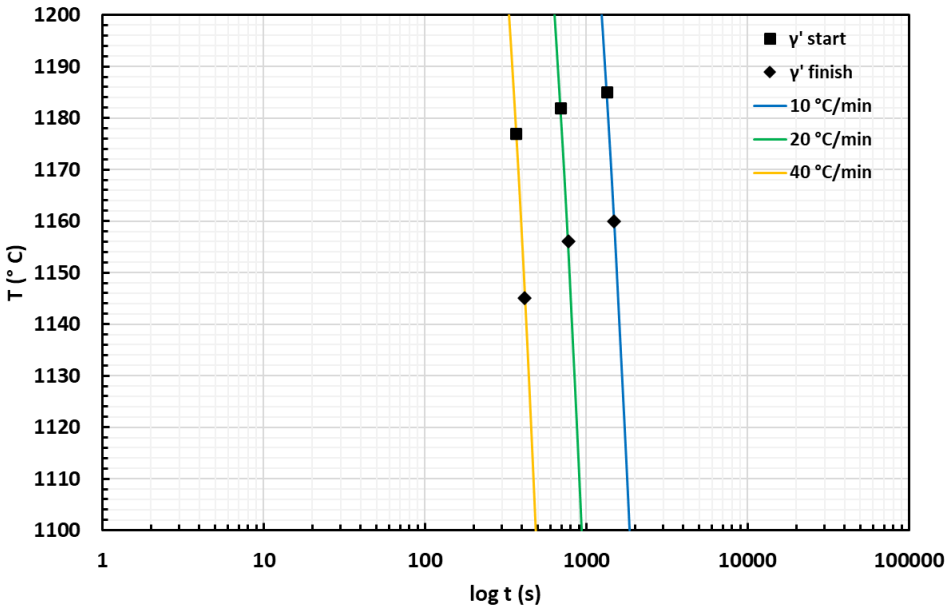

Figure 3.4: CCT curve related to γ' reprecipitation for SAM, based on DSC results.

Finally, the peak visible at around 1020 °C has been associated with the conversion of the MC carbides via the following reactions:

$$\gamma + \mathrm{MC} \rightarrow \mathrm{M_{23}C_6} + \gamma' \text{ [66]}$$

This interpretation is consistent with information on similar alloys, such as Inconel 738 LC [43], CM 247 LC [45] and MAR-M 247 [67]. In addition, it is also coherent with theoretical $\mathrm{M_{23}C_6}$ precipitation TTT curve calculated with Thermo-Calc in Figure 3.5 by Lerda et al. for Inconel 738.

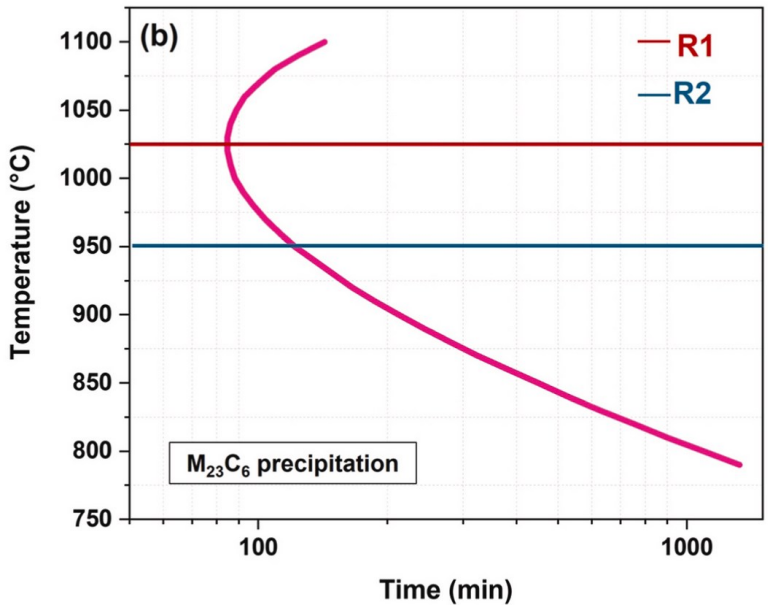

Figure 3.5: Thermo-Calc simulation of the TTT curve for the precipitation of $M_{23}C_6$ carbide at the grain boundary in Inconel 738 [13].

3.1.2. Double run analysis

The curve of the double run as-built sample has a similar cooling part to the single run curve. Conversely, the heating part presents some variations, allowing a better comprehension of the thermal history of the material. As can be seen in Figure 3.6, there are two main differences compared to the single run curve.

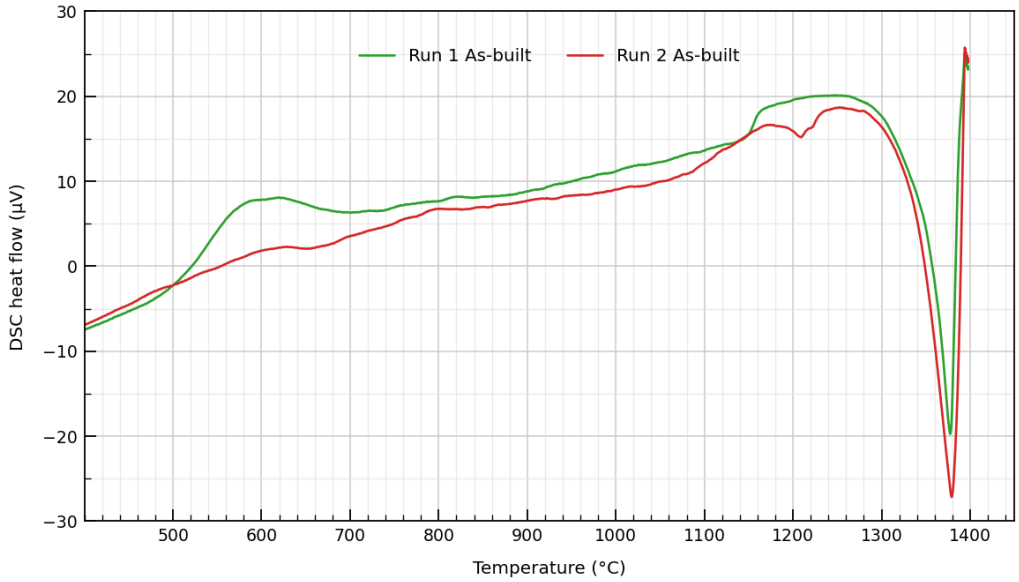

Figure 3.6: DSC analysis of the heating curve of the single and double run of the as-built sample.

Firstly, the exothermic peak at 600 °C is absent, confirming that it is derived from the PBF-LB process and is related to the formation of γ'. The second difference is the presence of an additional endothermic peak prior to final melting. This peak could therefore be linked to the formation of phases derived from the liquid, given that it

only appears in the second run where the melting point had already been reached during the first run. It has been hypothesised that this peak is associated with the melting of the eutectic phase located at the grain boundaries and derived from the incipient melting.

The presence of the eutectic phase and the accuracy of this interpretation were verified by investigating the sample derived from the DSC, using SEM. The analysis with backscattered electron (BSE) signal revealed the distinct phases and the occurrence of regions where liquid phases had formed (Figure 3.7). This is evident from the presence of eutectic zones with a dendritic structure. These zones are often contiguous with mixed carbides that have complex structures similar to those named in the literature as chinese-script, skeleton or fishbone-like carbides [68] [69].

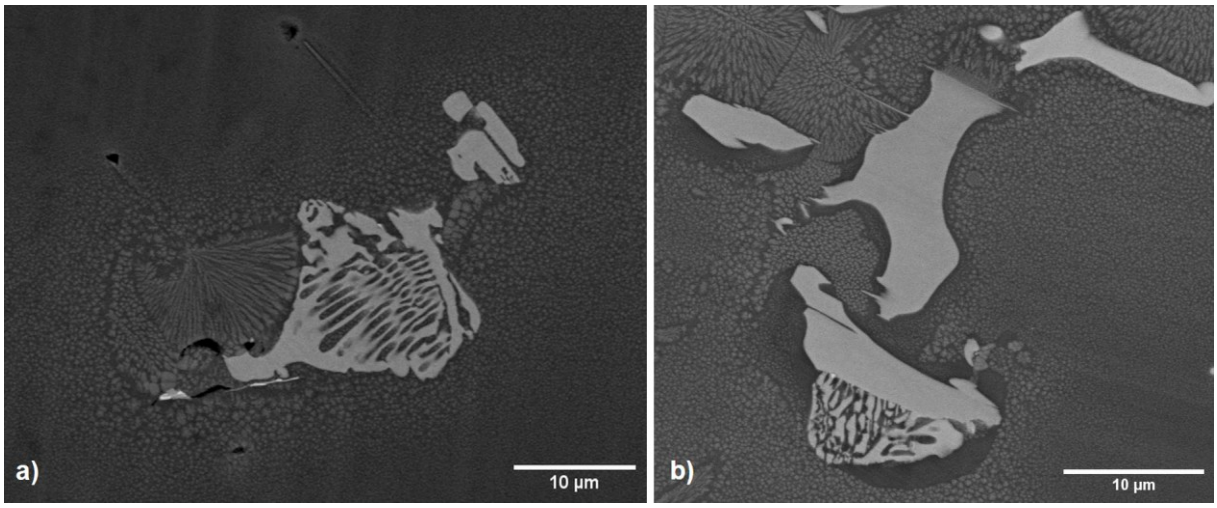

Figure 3.7: Morphologically complex carbides with the nearby eutectic structures.

The presence of morphologically complex carbides was found in similar alloy like MAR-M 247 and was linked to non-equilibrium conditions during solidification [67]. During the initial stage of solidification, the rapid formation of γ induces strong segregation of the material, resulting in the formation of MC eutectic carbides, which are rich in carbide-forming elements. EDS analysis (Table 3.2) confirms this hypothesis by revealing a high concentration of Hf and Ta in the MC carbide composition (Figure 3.8a). While this information cannot constitute valid evidence on its own, as EDS is a semi-quantitative analysis, when placed within a broader framework, as in this case, it provides useful insights.

The morphologically complex carbides differ from pre-existing MC carbides, which are characterized by a cuboidal shape ("blocky type" carbides) and a brighter BSE signal due to their higher tantalum content (Figure 3.8b). Indeed, as expected, the blocky-type carbide spectrum contains less Hf and has a higher Ta concentration, which is similar to what El-Bagoury et al. observed for Inconel 738 LC [70].

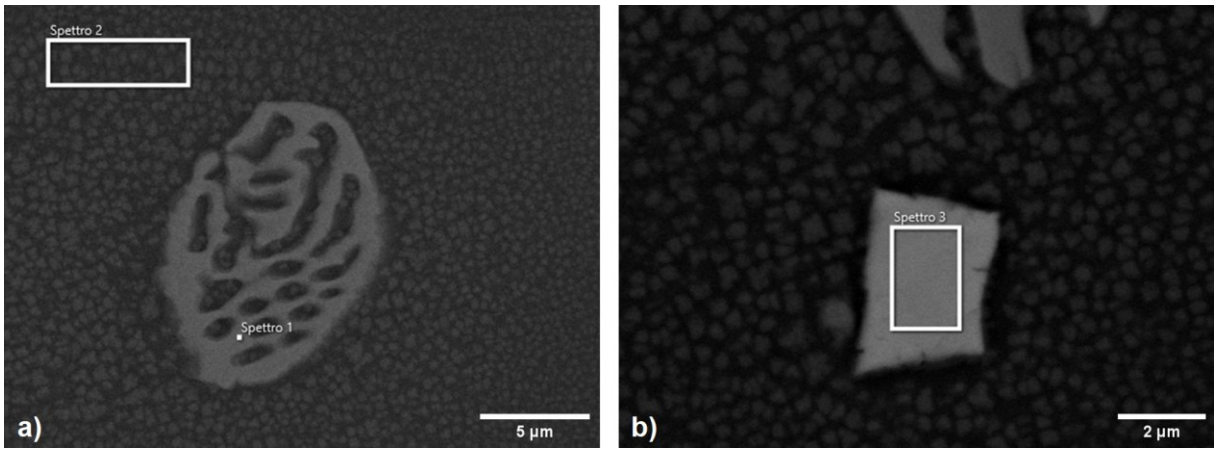

Figure 3.8: Spectrum analysed with EDS of (a) morphologically complex carbide and (b) blocky type carbide.

Table 3.2: EDS semi-quantitative analysis of chemical composition for the represented spectrum.

Spectrum	**C***	**Al**	**Cr**	**Co**	**Ni**	**Mo**	**Hf**	**Ta**	**W**
Spectrum 1	9.35	0.56	2.19	9.98	39.38	0.00	22.80	12.42	3.32
Spectrum 2	-	2.95	12.77	17.77	45.96	3.26	1.69	12.63	2.98
Spectrum 3	10.00	0.11	0.99	1.60	3.85	0.19	27.48	55.40	0.39

*The EDS analysis is not suitable for quantifying light elements such as carbon, so this value is only intended as an indication.

The last microstructural observation is that zones of a darker colour are often present around the mixed MC carbides. This is due to the presence of extremely fine γ' nuclei, as distinct from the larger, fan-like γ' present in the matrix. All of the observed microstructural features were also present in the double-run HIP STD sample.

Based on these findings and those from previous DSC analyses, the solidification sequence of the liquid portions that form when the solidus temperature is exceeded during an analysis or treatment has been hypothesised.

The microstructure derived from the liquid is formed by γ, γ' and MC carbides, which all precipitate from the matrix during solidification, as can be seen from the three peaks identified in the DSC. The microstructure is then modified by the transformation of the carbides from MC to $M_{23}C_6$ at approximately 1010 °C. This reaction occurs at the interface between the carbide and the matrix and results in the expulsion of tantalum into the matrix, creating a concentration gradient that causes two phenomena:

- γ'_{old} growth: where the matrix did not melt before, the growth of the pre-existing γ' phase is driven by diffusion.

- γ'_{new} nucleation: In the areas derived from the liquid, adjacent to the decomposing carbide, the nucleation of a new population of γ' is induced, initially in the form of an ultra-fine precipitate.

The resulting microstructure is characterized by the coexistence of three distinct γ' populations. The first population consists of small γ'_{old} particles, located far from the carbides. The second population consists of large γ'_{old} particles that were grown by Ta diffusion and are located near the carbides. The third population consists of fine γ'_{new} nuclei, adjacent to the carbides. These nuclei are smaller in size and give these regions a dark appearance.

To further investigate the validity of these findings, a maintenance period of 3 hours at 1010 °C during the cooling phase of a DSC trial was tested. The resulting microstructure (Figure 3.9) shows that the holding time permits Ta diffusion in the matrix, promoting the growth of the very fine γ' previously observed. Thus, the dark zone, which is characterized by nuclei that do not grow, is absent in this sample.

The key points of the process that takes place at 1010 °C can be summarized as follows:

1. The decomposition of primary MC carbides into secondary $M_{23}C_6$ carbides causes a localized release of Ta at the interface matrix-carbide.
2. Subsequently, the supersaturation of Ta in the matrix causes the growth of pre-existing γ' particles and the nucleation of a new, ultra-fine population of γ', adjacent to the carbide.
3. Implementing thermal maintenance at this temperature activates the diffusion of Ta in the matrix. This causes the growth of the fine γ' population and homogenizes the size and distribution of γ' in the microstructure.

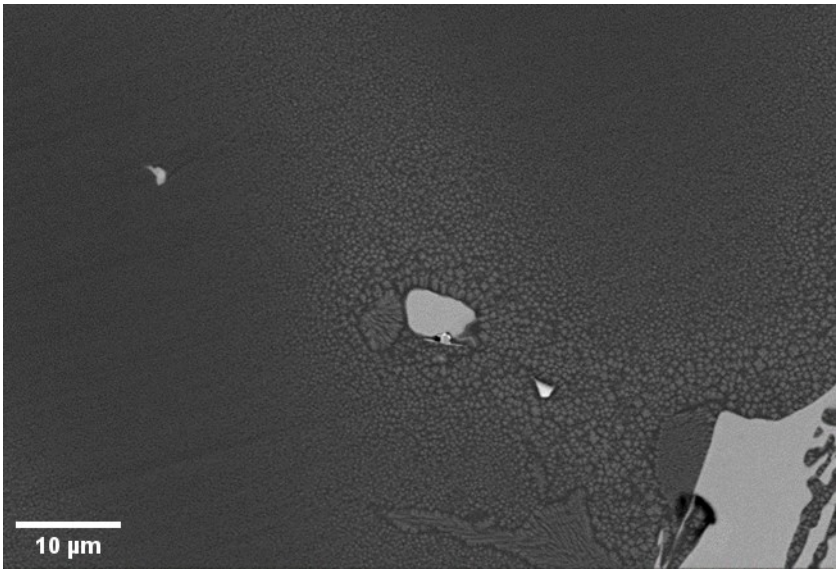

Figure 3.9: Microstructure obtained in the eutectic region after the maintenance at 1010 °C.

3.1.3. HIP and solution treated samples analysis

The last analysis was carried out on the HIP and solution samples. The heating curve for these samples is similar to that of the as-built sample (Figure 3.10). However, as with the double run curves, the peak related to the formation of γ' at 600 °C is practically negligible. This definitively confirms that the peak is due to the formation of γ', which was previously absent and can only be present in the first run of the as-built samples.

Focusing on γ' dissolution, the range is the same for all three curves. However, the trend after the transformation differs for the HIP STD + SOL 1230 curve compared to the HIP STD and as-built curves. This difference is likely due to the formation of liquid at the solution temperature of 1230 °C. Indeed, the only other curve in which a lowering is present is the double run curve. In this case, however, the endothermic peak is much more pronounced because the sample reached 1400 °C in the first run, maximising liquid formation.

Analysis of the HIP STD sample confirms this hypothesis, as the curve relating to this sample shows no signs of lowering. This was expected due to the heat treatment at 1180 °C, which is in the lower solution range, close to the γ' solvus but well below the solidus temperature (i.e. incipient melting).

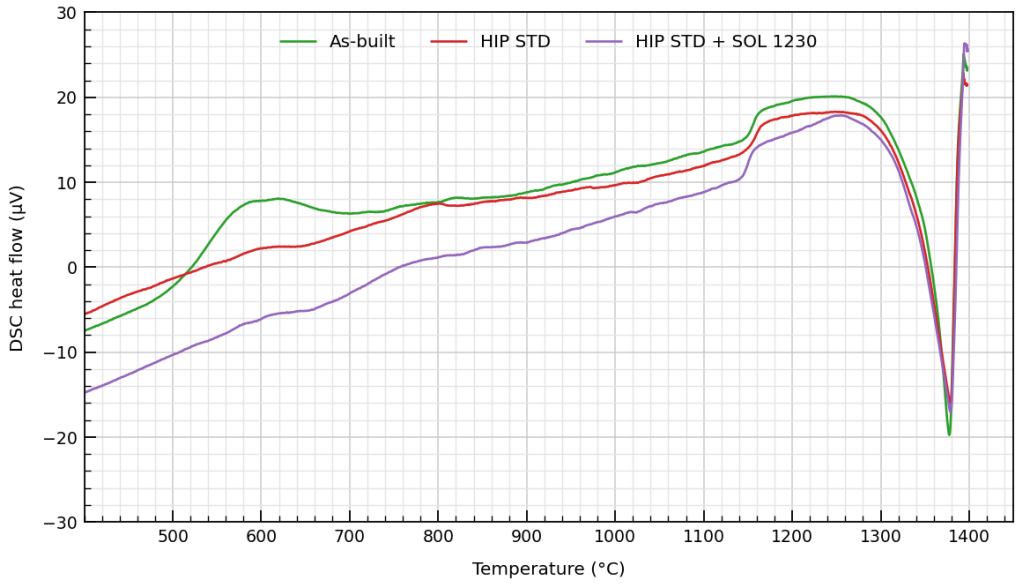

Figure 3.10: DSC analysis of the heating curve of As-built, HIP STD and HIP STD + SOL 1230 samples.

3.2. Solution heat treatment

The HIP and solution heat treatment parameters were established on the basis of DSC data, the standard temperatures provided by Siemens, and the findings of previous work on SAM [71]. Three different HIP temperatures were selected: 1180 °C, in line with the standard; 1220 °C, below the solidus temperature identified by DSC; and 1240 °C, slightly above it, to investigate whether incipient melting would occur.

For the solution treatment trials on HIP STD samples, temperatures ranged from 1140 °C, slightly below the onset of the γ' solvus located at approximately 1150 °C, to 1260 °C, well above the solidus (1225 °C), where liquid formation is almost certain. Samples treated within the theoretical optimal window, between 1220 °C and 1240 °C, were analysed in detail. Based on the observations from the HIP STD series, the subsequent HIP 1220 and HIP 1240 trials focused primarily on solution temperatures of 1220 °C and 1230 °C. A summary of this first part of the solution trials, carried out with air cooling, is provided in Table 2.1.

The solidus temperature represents a critical upper bound in this context, as exceeding it causes incipient melting, which introduces severe microstructural inhomogeneity and adversely affects mechanical properties [44]. The formation of low-melting γ+γ' eutectic phases at grain boundaries is particularly concerning, as this condition is widely associated with cracking. If such eutectic persists after the full heat treatment sequence, it may weaken grain boundary cohesion, promote intergranular crack propagation during service, and increase susceptibility to ductility-dip cracking at intermediate temperatures [64]. Beyond cracking, eutectic phases and associated porosity also degrade high-temperature mechanical properties of superalloys [72].

In the first phase of the trials, air quenching was applied after solution treatment. Once the optimal temperature of 1220 °C was identified, the second phase of trials adopted a slower, more industrially viable cooling rate of approximately 40 °C/min, applied to samples treated at 1220 °C.

3.2.1. Effect of temperature: HIP performed at 1180 °C

As previously stated, the first part of the trials involved solution treatment of HIP STD (i.e. processed at 1180 °C) samples at temperatures ranging from 1140 to 1260 °C.

Initially, a qualitative microstructural analysis was conducted on samples within the 1220-1260 °C range. In all samples examined, primary MC carbides originating from the PBF-LB process are clearly visible. These carbides are characterised by their cuboidal morphology and preferential alignment along the build direction, forming rows that reflect the strong influence of the printing process on their distribution. In some instances, these carbide rows coincide with grain boundaries, as illustrated in Figure 3.11. High-temperature treatments such as HIP and solution annealing could partially mitigate this inhomogeneity; however, complete chemical rehomogenisation is not achieved, and regions of locally elevated carbide density persist.

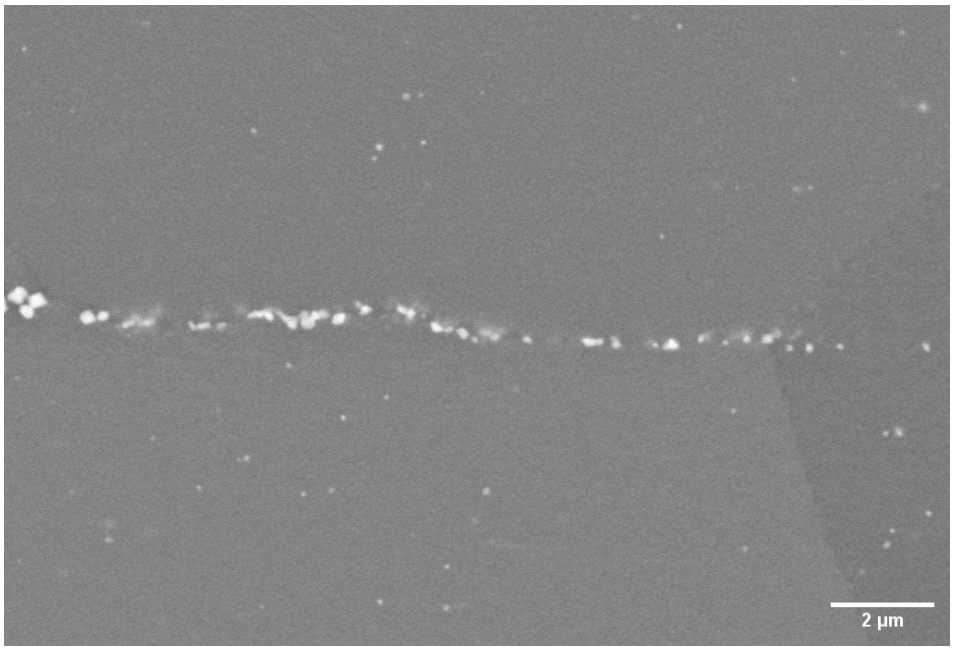

Figure 3.11: Row of MC primary carbides located along the grain boundary in HIP STD SOL 1220.

Further examination reveals additional residual features attributable to the PBF-LB process. Defects associated with partially unmelted powder particles of varying size were identified in all samples. These defects are recognisable by their dendritic internal structure enclosed within a near-circular boundary, as shown in Figure 3.12a. Such defects may be detrimental to material performance, as the pronounced chemical inhomogeneity they introduce can promote elemental segregation and the formation of low-melting zones. Evidence of this is provided by the shrinkage porosity observed in the vicinity of these particles (Figure 3.12b). It should be noted that these features are distinct from the eutectic dendrites observed in the post-DSC sample discussed in Chapter 3.1.2.

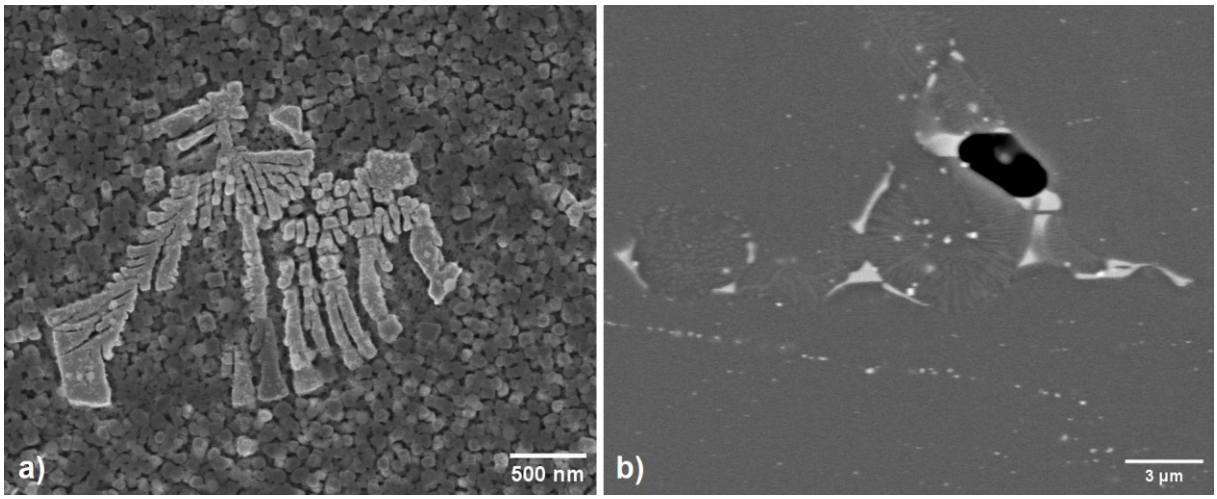

Figure 3.12: Dendritic structure of unmelted powder particles. a) SE image of HIP STD SOL 1230 etched sample b) BSE image of HIP STD SOL 1220 unetched sample.

A further defect was identified in the material (Figure 3.13), measuring approximately 3 µm in length. It is hypothesised to be an oxide inclusion, a type of defect arising from the PBF-LB fabrication stage that is commonly reported in metal AM components and known to be detrimental to structural integrity and long-term durability. Such inclusions are attributed to residual oxygen present in the processing chamber during fabrication [73].

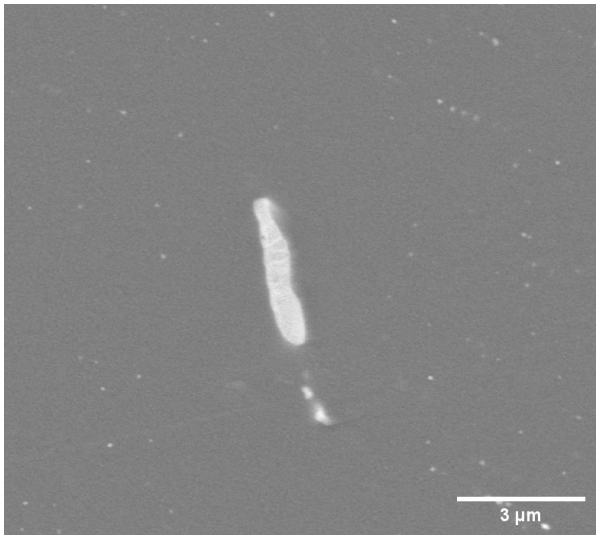

Figure 3.13: Microstructural feature identified as an oxide inclusion derived from PBF-LB process in the HIP STD SOL 1220 sample.

With regard to the assessment of potential liquid formation, a detailed analysis of grain boundaries and triple junctions was carried out. In the sample solution treated at 1220 °C, no eutectic structures or morphologically complex carbides were observed at grain boundaries. This confirms that the solidus temperature was not reached and that no low-melting phases are present at the grain boundaries, features that would otherwise be detrimental to creep resistance and overall mechanical properties.

In contrast, all samples treated at higher temperatures exhibit a newly formed phase located along grain boundaries, and in several instances these phase clusters are found adjacent to dendritic structures. Based on their morphology and compositional similarity to phases observed in the DSC samples, these are identified as irregular carbides precipitated from the liquid. Since these are the first samples in the series to exceed the solidus temperature, the presence of such liquid-derived features was anticipated. Both the quantity and size of the carbide clusters increase markedly with increasing treatment temperature.

In the samples solution treated at 1230 °C and 1240 °C, the carbide morphology differs substantially from the skeleton/fishbone-like observed in DSC samples, being instead governed by the local geometry of the grain boundary or triple junction. In the HIP STD SOL 1240 sample in particular, grain boundaries and triple junctions are almost entirely decorated with irregular carbides of liquid origin.

Along the grain boundaries, these carbides adopt an elongated morphology (Figure 3.14a), resulting in a smooth boundary profile devoid of corrugations. In some cases, such as in Figure 3.14b, this phase appears to form a continuous film along the grain boundaries, a morphology that may constitute a serious microstructural defect with several detrimental consequences. When sufficiently abundant, the film likely establishes a continuous weak path along the grain boundaries, potentially replacing the beneficial pinning effect of discrete particles with an embrittlement mechanism that could facilitate intergranular separation under creep or fatigue loading.

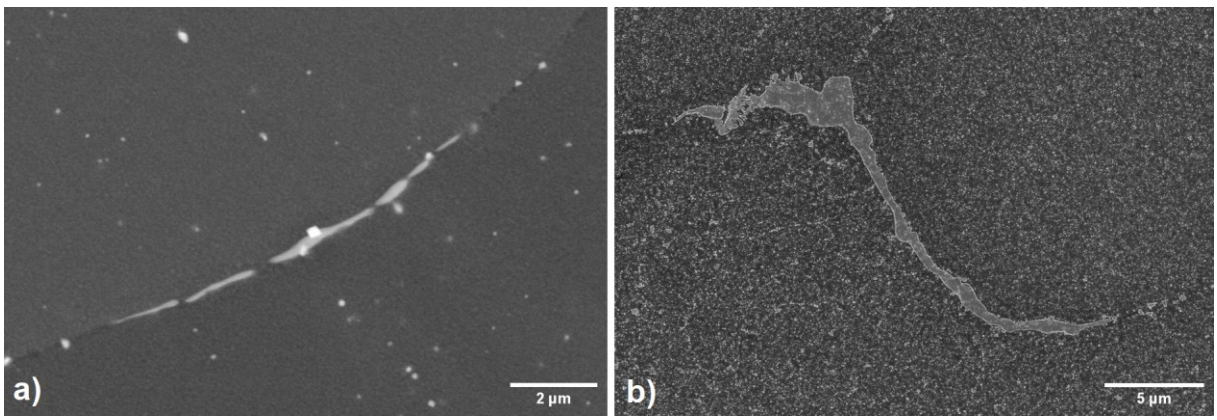

Figure 3.14: Carbide morphologies at the grain boundaries in HIP STD SOL 1240 sample: a) BSE image of elongated clusters, b) SE image of continuous film.

In the HIP STD SOL 1230 sample, the MC carbide clusters are predominantly located at triple junctions, such as in Figure 3.15a, where they assume a characteristic triangular morphology imposed by the geometry of the intersecting grain boundaries. Unlike the previous sample, the grain boundaries (Figure 3.15b) are largely free of carbide clusters. Instead, they exhibit a relative abundance of primary γ', which can be distinguished from carbides by its lower clustering tendency and finer precipitate size,

which is more similar to that of secondary γ'. Furthermore, primary γ' has a blocky morphology, not dependant from the grain boundary geometry.

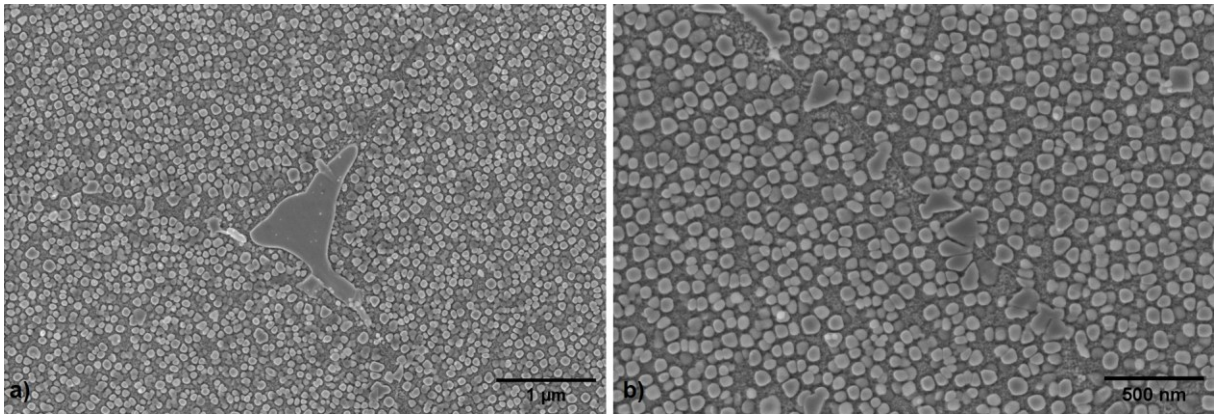

Figure 3.15: SE images of HIP STD SOL 1230 sample: a) large carbide located at triple junction, b) grain boundary.

Complementary EDS analysis was performed on the HIP STD SOL 1230 sample in a region containing two triple junctions with a high local density of carbides (Figure 3.16). As shown in Table 3.3, the composition of the light grey phase (Spectrum 1) differs markedly from that of an adjacent region at the boundary (Spectrum 2), where a eutectic zone with dendritic microstructure is present. The key compositional distinction confirming the identity of the brighter phase as an MC carbide is its high Hf content, which is absent in the neighbouring eutectic region. A compositional analysis of this region reveals a chemical composition similar to the matrix, but with an elevated Ta concentration attributable to a high-volume fraction of γ'.

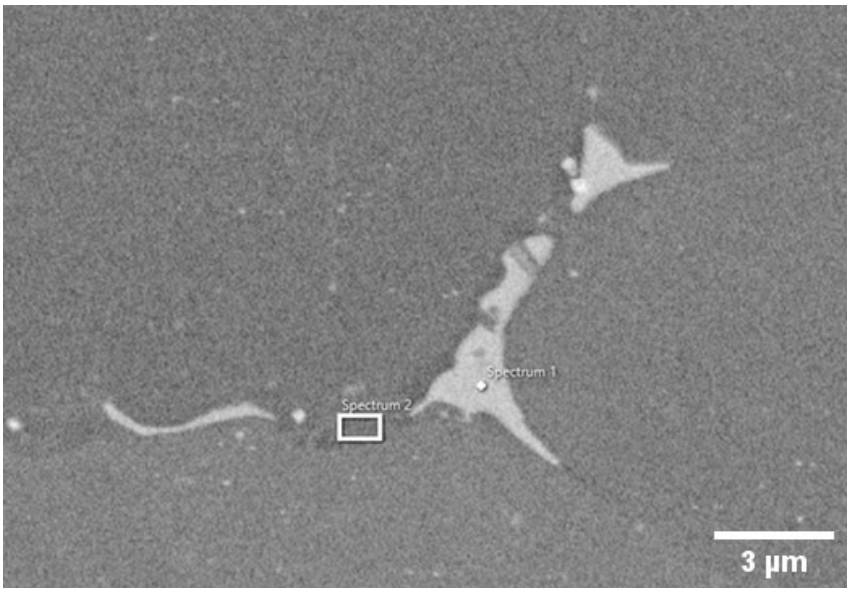

Figure 3.16: Particular grain boundaries and triple junctions with labels of the sites where the EDS analysis was performed.

Table 3.3: EDS semi-quantitative analysis of chemical composition for the represented spectrum.

Spectrum	C*	Al	Cr	Co	Ni	Mo	Hf	Ta	W
Spectrum 1	10.50	0.16	3.72	9.33	35.56	0.83	24.99	10.48	4.43
Spectrum 2		2.47	12.25	16.36	48.23	2.33	1.70	13.45	3.20

*The EDS analysis is not suitable for quantifying light elements such as carbon, so this value is only intended as an indication.

As noted above, dendritic microstructures of eutectic origin are sometimes found in the vicinity of the carbide clusters. In the HIP STD SOL 1230 sample, dendrites are mostly confined to triple junctions (Figure 3.17a), where only limited quantities of eutectic liquid had segregated. In the HIP STD SOL 1240 sample, by contrast, these dendrites are large and distributed across extensive regions, such as in Figure 3.17b. In some triple junctions, the concurrent presence of MC carbides, eutectic dendrites, shrinkage porosity, and other detrimental microstructural features produces regions that are severely compromised, with a high defect density that is expected to result in poor mechanical performance.

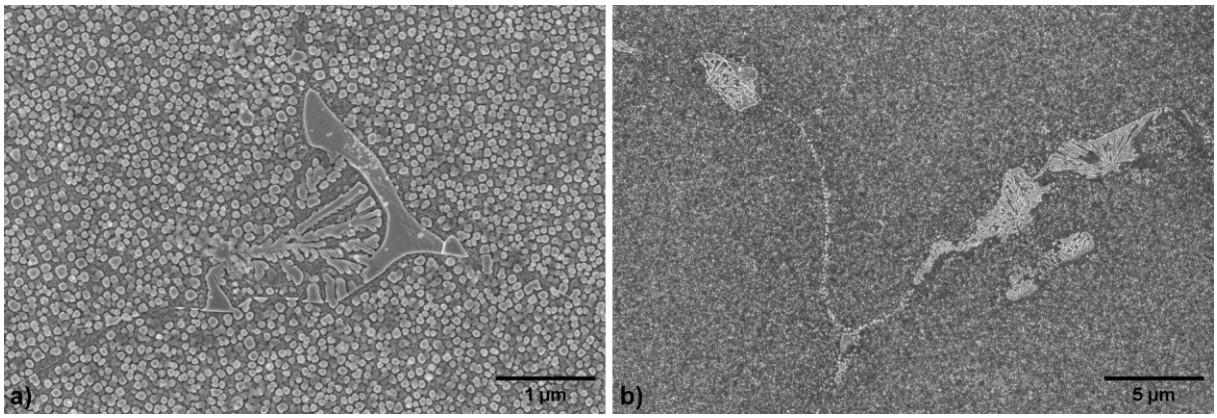

Figure 3.17: SE images of dendritic structures in a) HIP STD SOL 1230 sample and b) HIP STD SOL 1240 sample.

For the HIP STD SOL 1260 sample, given that treatment at 1240 °C had already produced extensive microstructural damage, characterisation was limited to light optical microscopy. The primary objective was to identify the large liquid-derived phases observed in the other super-solidus samples.

Figure 3.18a presents an area of an unetched specimen in which regions derived from liquid are clearly visible. The carbide microstructure closely resembles that observed in the double-run DSC analysis, confirming that the degree of damage is substantially greater than in the HIP STD SOL 1240 sample. Examination of the electrolytically etched region (Figure 3.18b) reveals the complex carbides with greater clarity and additionally allows the eutectic regions to be identified. These regions are situated along

grain boundaries in the immediate vicinity of the larger complex carbides and are distinguished by a light grey contrast, intermediate between the darker appearance of the intragranular matrix and the bright contrast characteristic of the irregular carbides.

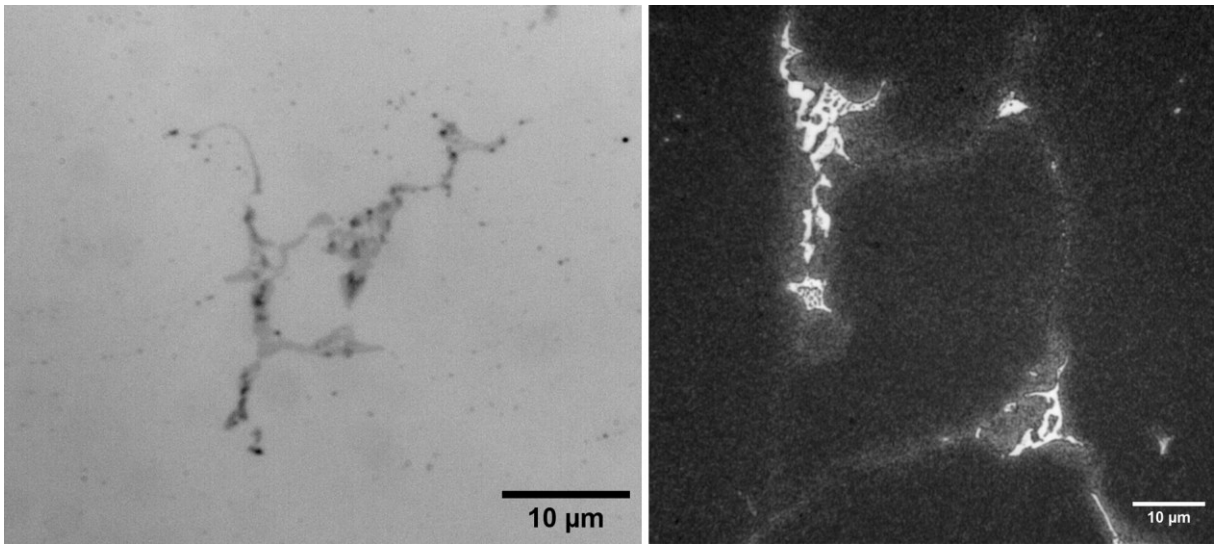

Figure 3.18: Images from LOM of the irregular carbides in the HIP STD SOL 1260 sample in a) unetched region and b) etched region.

Turning to the analysis of γ' precipitates in the three samples examined by FESEM, all three morphological classes were identified: primary γ', located at grain boundaries; secondary γ', the most abundant population, distributed throughout the matrix; and tertiary γ', present in the background between other particles. The tertiary precipitates are particularly difficult to resolve owing to their nanometric dimensions, with the largest measured diameter being approximately 20 nm. Clear imaging of this population was only achievable in micrographs acquired at grain boundaries, such as that shown in Figure 3.19.

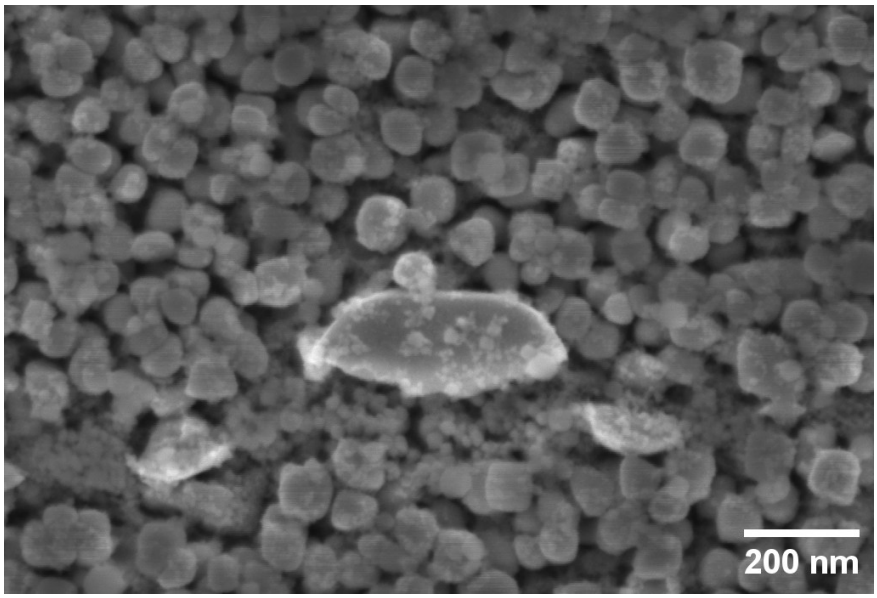

Figure 3.19: SE image of grain boundaries where the three γ' classes are present.

A quantitative analysis of the secondary γ' population was subsequently carried out on the small submicrometric particles. Given the rapid cooling rate and the correspondingly limited time available for precipitate growth, the secondary γ' particles are relatively fine in all samples examined.

Representative FESEM micrographs of the γ' microstructure for each of the three samples are presented in Figure 3.20. Five images for each sample were analysed to extract the average equivalent diameter and volume fraction, the results of which are summarised in Table 3.4.

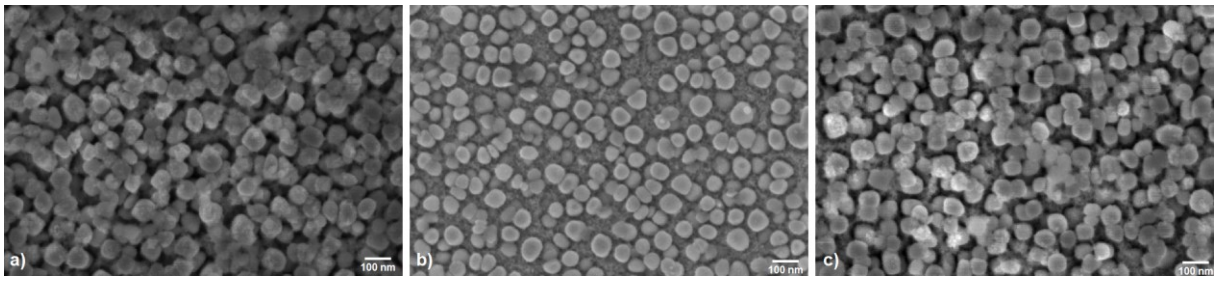

Figure 3.20: SE images of secondary γ' inside the grains in a) HIP STD SOL 1220 sample, b) HIP STD SOL 1230 sample and c) HIP STD SOL 1240 sample.

Table 3.4: Values on the γ' population acquired from image analysis with ImageJ.

Sample	**% γ' (vol %)**	**Average γ' diameter (nm)**
HIP STD SOL 1220	43.6 ± 5.9	62.2 ± 4.4
HIP STD SOL 1230	39.7 ± 1.1	59.4 ± 1.4
HIP STD SOL 1240	39.7 ± 2.8	60.4 ± 0.4

The results indicate that the secondary γ' volume fraction and the average diameter both decrease slightly with temperature increase, though the values remain within the same overall range, and no statistically significant trend can be established. This behaviour is most readily attributed to the dominant influence of cooling rate on γ' precipitation kinetics. A plausible interpretation of the observed slight reduction in both diameter and volume fraction is that, as the solution treatment temperature increases, the secondary γ' formed during the slow cooling stage of the HIP treatment is progressively dissolved and does not fully reprecipitate upon subsequent rapid cooling. The γ' fraction that remains dissolved in the supersaturated solid solution is then expected to precipitate during the first aging treatment.

A more detailed analysis was performed on the γ' particle population, including a statistical characterisation of the size distribution. All three samples exhibit a log-normal size distribution; for brevity, only the distribution of the HIP STD SOL 1230 sample is shown in Figure 3.21 , as the remaining samples display a nearly identical shape despite marginally different numerical values. The distribution shows a modal diameter of approximately 60 nm, with particles ranging from around 40 nm to just

above 92 nm. The tail extending toward larger diameters is consistent with the precipitation kinetics of γ', whereby a large population of fine particles coexists with a smaller fraction of coarser precipitates that have undergone coalescence, as visible in Figure 3.20.

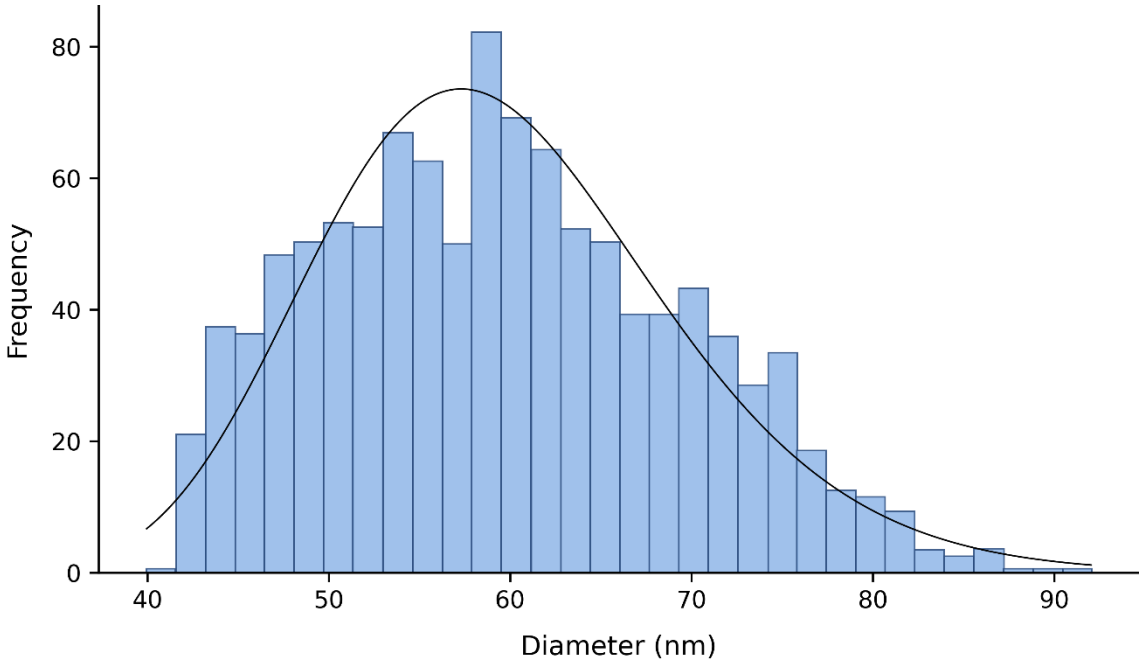

Figure 3.21: Size distribution histogram of secondary γ' precipitates measured in the HIP STD SOL 1230 sample, with a log-normal curve fitted to the data.

Grain size measurements and hardness testing were performed on all samples in the 1140-1260 °C range, complementing the qualitative microstructural analysis and quantitative γ' characterisation carried out on samples within the optimal temperature window. This broader dataset provides a more complete understanding of how treatment temperature affects material properties.

Firstly, the HIP STD SOL 1140 1h sample is of particular interest due to the pronounced hardness gradient observed along its vertical cross-section (Figure 3.22). Starting from the lower surface, hardness decreases steeply between 1 and 8 mm depth, dropping by 33 HB10 over a short distance, reaching a minimum of 341 HB10 at 5 mm. Approaching the lower surface, the value slightly rises again, though only to around 344 HB10, remaining well below the value measured at the top. This strong gradient provides clear evidence of the time required to achieve a complete and uniform solution heat treatment. Since the post-HIP STD samples were initially homogeneous, with a hardness of 335 $\pm$ 5 HB10, the observed heterogeneity can be attributed exclusively to the solution treatment and the associated cooling conditions.

The most likely origin of this behaviour lies in the sub-solvus temperature adopted. With a γ' solvus onset at 1148 °C, a treatment at 1140 °C is only 8 °C below the dissolution threshold, a range in which the γ' volume fraction is extremely sensitive to

small thermal fluctuations. A variation of just 5-10 °C in this regime can substantially alter the fraction of dissolved precipitate. The absence of hardness gradients in the sample treated at the same temperature for 4 hours confirms that a sufficiently long dwell time is necessary to eliminate hardness inhomogeneities. The non-uniformity observed in the short treatment is therefore a direct consequence of the intrinsic sensitivity of the alloy microstructure in the sub-solvus regime.

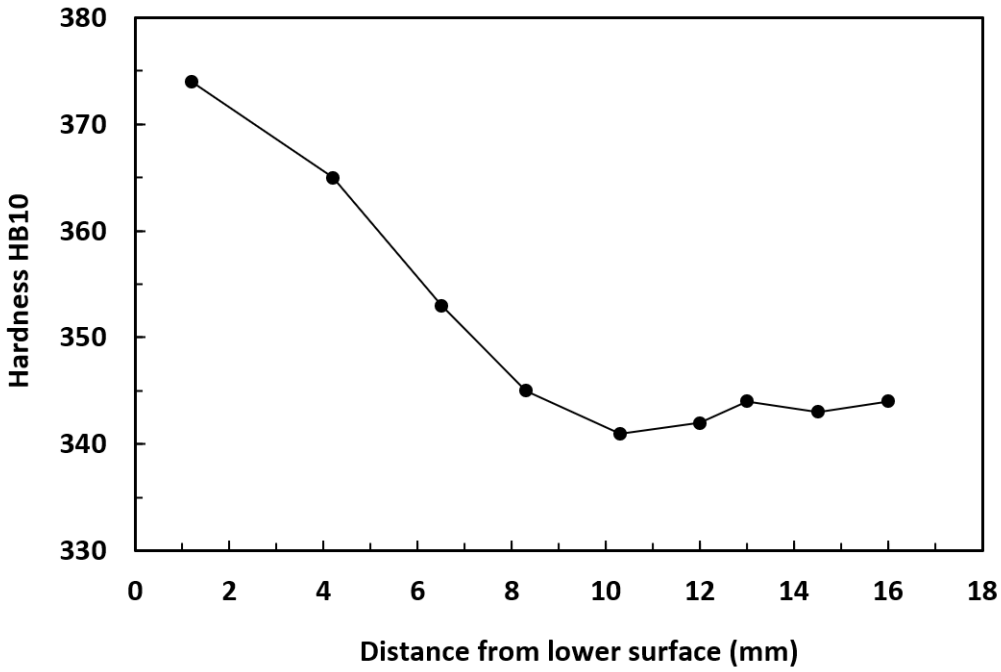

Figure 3.22: Hardness profile along the vertical cross-section of the HIP STD SOL 1140 °C 1h sample, measured as a function of distance from the lower surface.

Then, a comprehensive measurement of all the solutioned samples was performed. All hardness values obtained range from 339 to 370 HB10, all exceeding the baseline value of 335 HB10 measured on the as-HIPed sample at 1180 °C. As shown in Figure 3.23, the trend is non-monotonic, with the highest mean value of 358 HB10 recorded at 1220 °C. Outside this window, both at lower and higher temperatures, the scatter is more contained, suggesting a more uniform microstructural response to the treatment. Above this temperature, hardness decreases progressively up to 1240 °C, beyond which no significant further reduction is observed between 1240 and 1260 °C.

The decrease in hardness at higher temperatures can be attributed to the occurrence of incipient melting and the greater dissolution of γ' during solution treatment. In this scenario, γ' is dissolved into the matrix during the hold, but the subsequent rapid cooling does not allow full reprecipitation, leaving a supersaturated matrix with a relatively low γ' volume fraction. The fraction that remains in solid solution is then expected to precipitate during the first aging step. The lowest value in the series is recorded at 1170 °C, just above the γ' solvus, indicating that the rapid cooling which

begins in the γ′ solvus interval further limits reprecipitation, corresponds to low hardness.

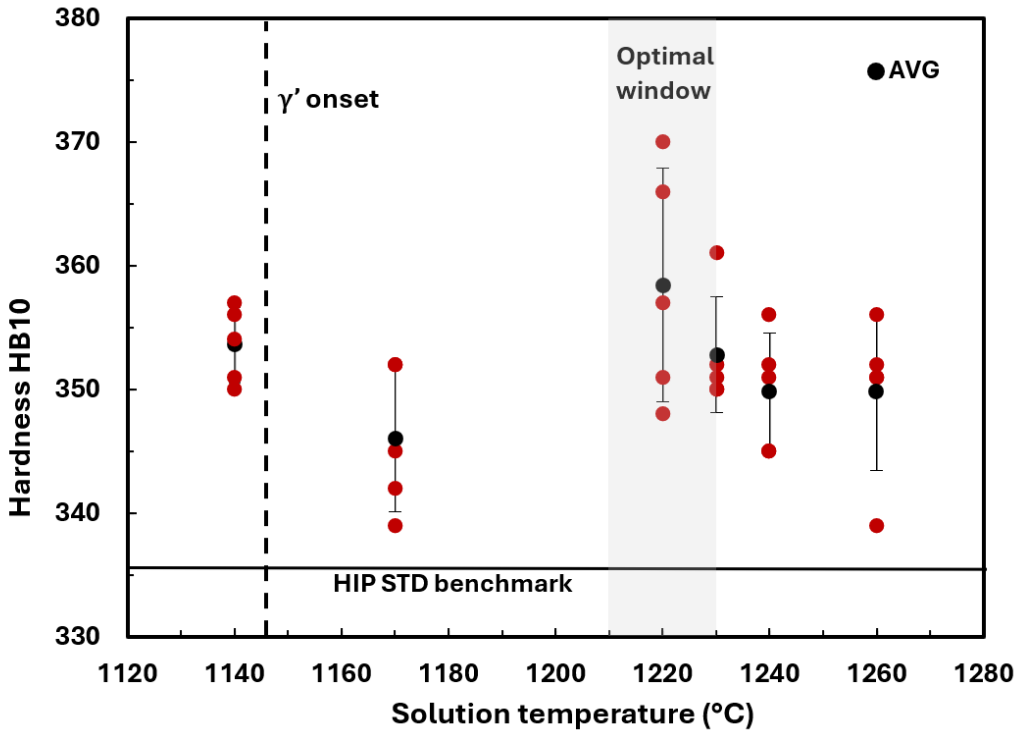

Figure 3.23: Hardness values for all the HIP STD samples solution treated at different temperatures for 4 hours.

Finally, measurements of the vertical grain size were carried out following the procedure described in the 'Materials and methods' section, with results shown in Figure 3.24. All samples exhibit grain sizes exceeding 110 μm, with a maximum of approximately 135 μm reached by both the HIP STD SOL 1220 and HIP STD SOL 1260 samples. Relative to the value of 115 μm measured at 1140 °C, this represents an increase of approximately 20 μm, corresponding to 17%. Despite the relatively large scatter observed in some samples, a clear trend is apparent: grain size increases with solution temperature, following a linear relationship well described by a fit with $R^2 = 0.8825$, indicating a strong correlation. The fitted equation ($y = 0.1945x - 108.19$) suggests that each 10 °C increase in solution temperature corresponds to an average grain size increase of approximately 2 μm. It is worth noting that the sample treated at 1220 °C, identified as the optimal solution temperature, exhibits the highest mean vertical grain size, albeit with a considerable spread in the individual measurements.

The observed increase in grain size with temperature is consistent with thermally activated grain boundary migration, in which higher temperatures provide greater driving force and atomic mobility for grain growth. In the supersolvus regime, the dissolution of pinning phases such as carbides, γ′, and the Hf-rich intermetallic phase characteristic of this alloy removes obstacles to grain boundary movement, further promoting grain coarsening.

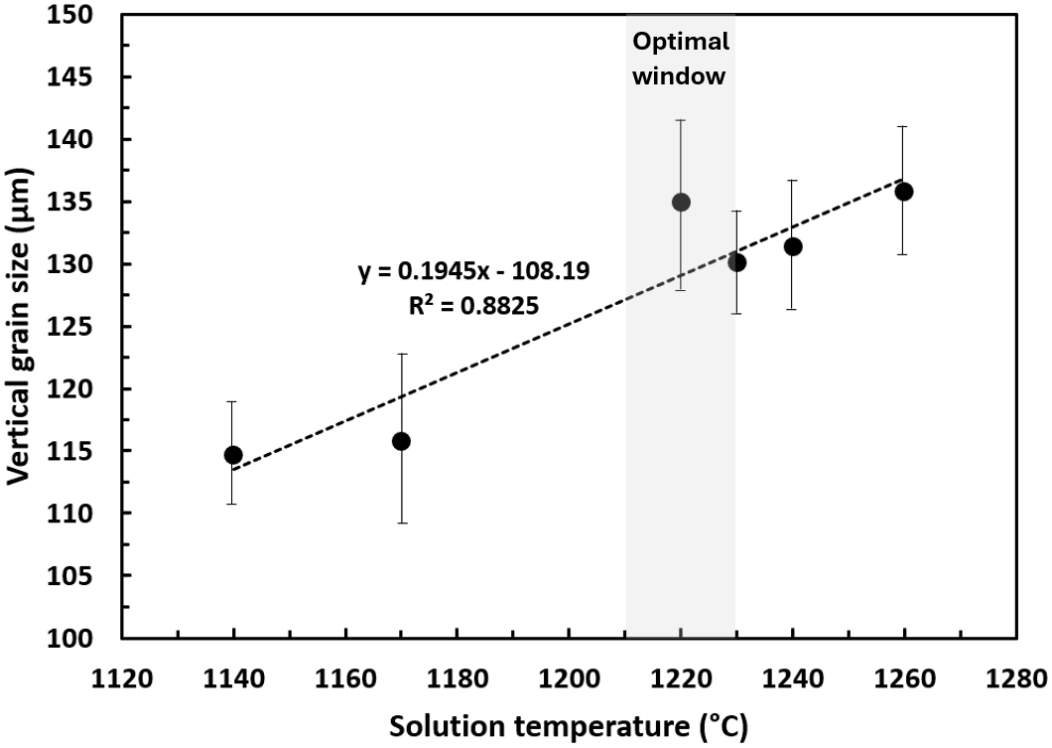

Figure 3.24: Vertical grain size mean values for all the HIP STD samples solution treated at different temperatures for 4 hours.

3.2.2. Effect of temperature: HIP performed at 1220 °C

The second HIP treatment temperature investigated was 1220 °C. Based on the results obtained from the HIP STD samples, solution treatment temperatures of 1220 °C and 1230 °C were selected for this series.

The first aspect examined was the presence of the defects derived from PBF-LB process previously identified in the HIP STD samples. The goal was to assess whether the higher HIP temperature promotes greater microstructural homogenisation, or whether the defects inherent to the PBF-LB process persist regardless of the heat treatment applied.

As shown in Figure 3.25, the segregation defects identified in the previous series are still present. The BSE images reveal a pronounced segregation of primary MC carbides originating from the PBF-LB process, with a high particle density distributed around the observed grains and concentrated particularly near grain boundaries. In the vicinity of these carbide-rich regions, morphologically complex carbides and eutectic zones are frequently observed, indicating that the strong local segregation induced liquation at the grain boundary.

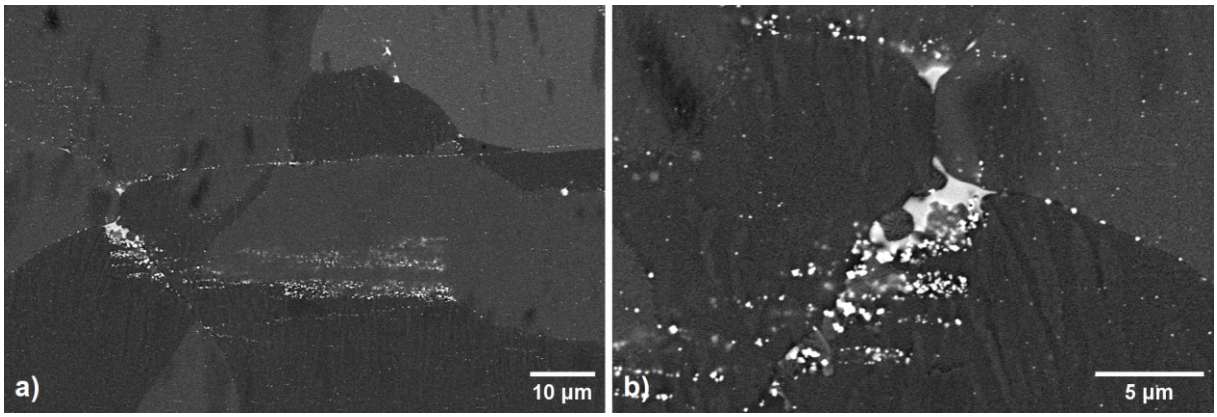

Figure 3.25: BSE images of region with pronounced PBF-LB induced segregation, characterised by primary MC carbide accumulation, in HIP 1220 SOL 1220 sample.

Partially unmelted powder particles were clearly identified, as illustrated in Figure 3.26a where localised liquation in the vicinity of such particles has left characteristic features including mixed carbides and shrinkage porosity, analogous to those discussed in the previous chapter.

An oxide inclusion analogous to that reported previously in Figure 3.12 was also identified in this sample (Figure 3.26b), though in this case the defect appears larger and more elongated, measuring approximately 6-7 µm in length. The inclusion presents a porous internal microstructure, visible as dark circular features within its body, which is consistent with the typical morphology of oxide inclusions and further supports their identification.

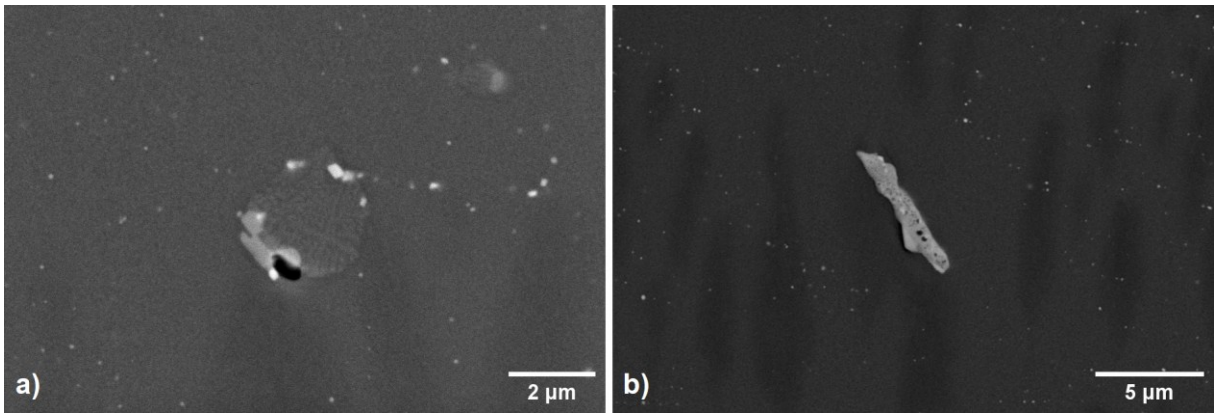

Figure 3.26: BSE images of defects originating from the PBF-LB fabrication stage, identified in the HIP 1220 SOL 1220 sample: a) partially unmelted powder particle with associated shrinkage porosity and b) porous oxide inclusion.

A subsequent examination confirmed the absence of eutectic or dendritic structures in most regions of the sample, these being observed only in zones of particularly strong segregation derived from PBF-LB process, such as that shown in Figure 3.27. It can therefore be confirmed that such features are highly localised and uncommon in the microstructure of the sample solution treated at 1220 °C. Nevertheless, the inhomogeneities identified in this series should ideally be minimised, as their presence introduces variability in local properties and may compromise the repeatability of mechanical behaviour.

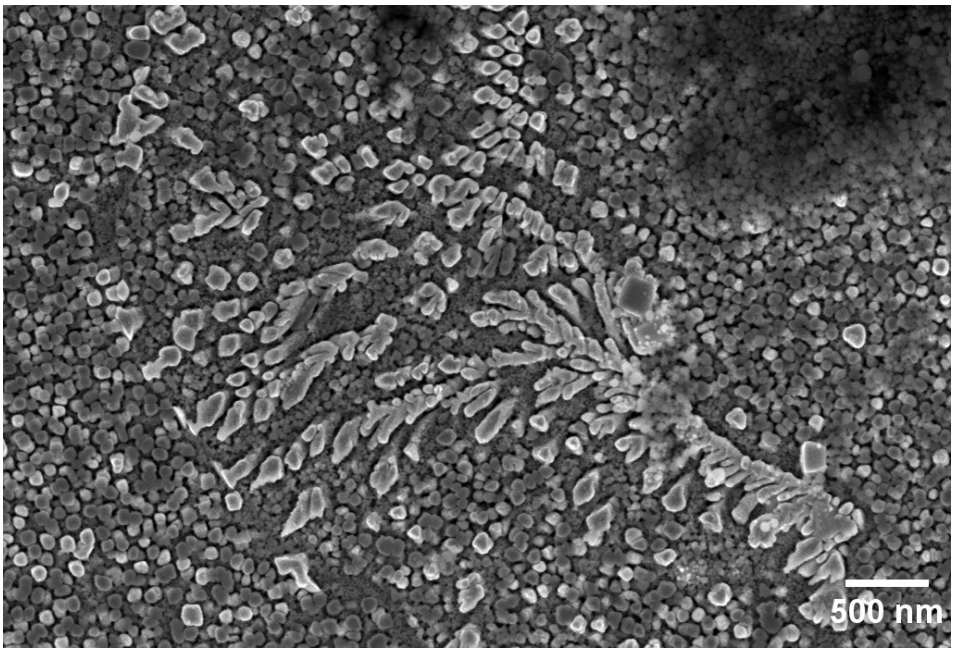

Figure 3.27: SE image of highly segregated region with dendritic structure in HIP 1220 SOL 1220 sample.

The situation differs markedly in the sample treated at 1230 °C, where extensive eutectic damage is present. Eutectic and dendritic structures are found both at triple junctions and along grain boundaries, and in some cases, such as in Figure 3.28, eutectic regions extend into the grain interior, with wide and severely damaged boundary zones.

The eutectic regions are sufficiently developed that γ' lamellae can be clearly identified, with mixed carbides frequently observed between the lamellar regions. The

morphological continuity between the carbides and the surrounding eutectic indicates that both originated from liquid present at the grain boundary. This microstructure differs from that observed in the HIP STD SOL 1230 sample and more closely resembles that of the HIP STD SOL 1240 condition (Figure 3.17b), suggesting that the higher HIP temperature amplifies the microstructural impact of solution treatment when the solidus temperature is exceeded.

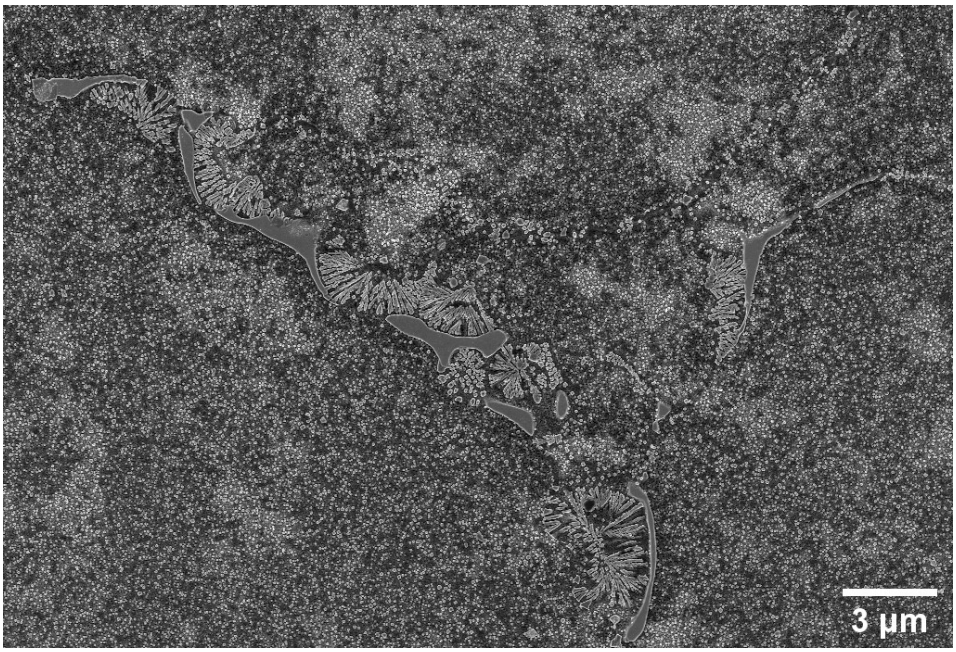

Figure 3.28: SE image of the HIP 1220 SOL 1230 sample showing extensive eutectic damage at grain boundaries and triple junctions.

Focusing on grain boundary microstructure, neither sample presents a uniform boundary morphology throughout. In the HIP 1220 SOL 1220 sample, no film-like carbide morphology is observed along the grain boundaries, confirming that no liquid was formed. Some boundaries present beneficial pinning particles, likely primary γ', distinguishable from the surrounding secondary γ' by their larger size and irregular morphology, as shown in Figure 3.29a.

In the HIP 1220 SOL 1230 sample, the grain boundary morphology is more varied. Some boundaries exhibit pinning particles and a corrugated profile (Figure 3.29b), while others are decorated with complex carbides that in some cases connect to form film-like morphologies, such as in Figure 3.28.

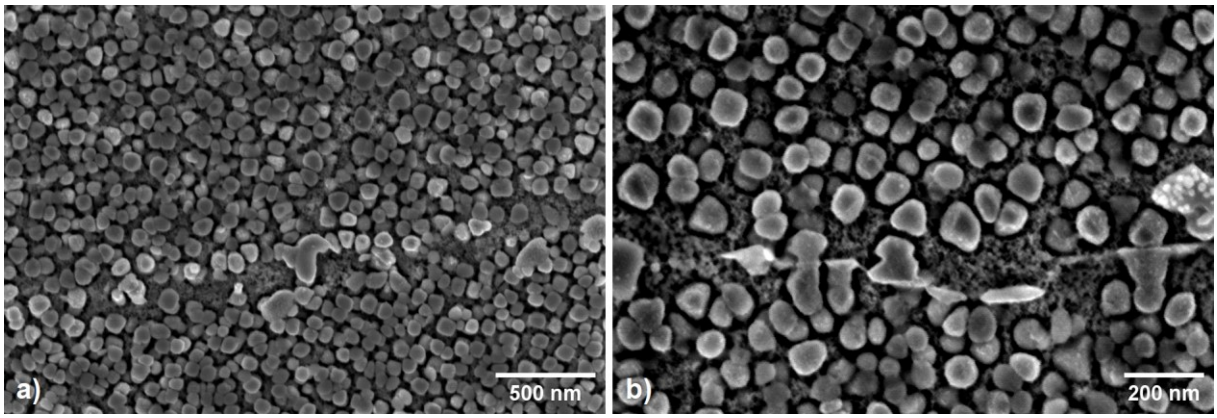

Figure 3.29: SE images of grain boundaries in a) HIP 1220 SOL 1220 b) HIP 1220 SOL 1230.

Regarding the secondary γ' population, the particle sizes in these samples are larger than those observed in the HIP STD series, with average equivalent diameters of 73.4 $\pm$ 3.2 nm for the HIP 1220 SOL 1220 sample and 66.4 $\pm$ 2.8 nm for the HIP 1220 SOL 1230 sample. In terms of volume fraction, the HIP 1220 SOL 1220 sample presents the highest value among all samples subjected to fast cooling after solution treatment, at 46.5 $\pm$ 1.7%, while the HIP 1220 SOL 1230 sample shows a slightly lower value of 43.0 $\pm$ 3.0%.

The higher average diameter and volume fraction of the former may be attributed to the greater degree of γ' dissolution achieved at the higher solution temperature, though the differences between the two samples remain small. This is also consistent with the FESEM images in Figure 3.30, where the γ' particles located within the grain interior appear morphologically very similar between the two samples, with some particles showing signs of coalescence in both cases.

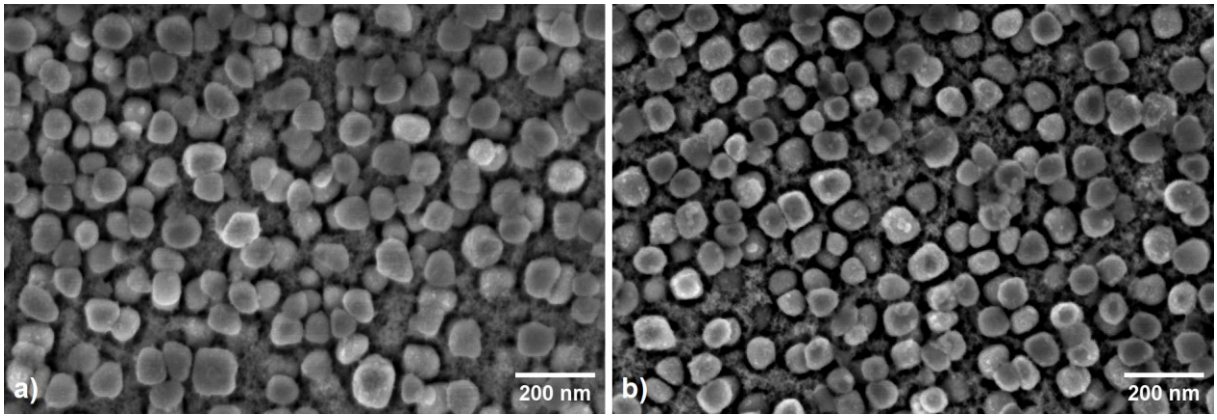

Figure 3.30: SE images of secondary γ' inside the grains in a) HIP 1220 SOL 1220 sample, b) HIP 1220 SOL 1230 sample.

A statistical analysis of the γ' particle size distribution for the HIP 1220 SOL 1220 sample is presented in Figure 3.31; the HIP 1220 SOL 1230 sample is omitted as its distribution is nearly identical in shape, differing only in the absolute values consistent with the slightly lower mean diameter reported above. The population follows a log-

normal distribution, although the fit, while reasonable, does not perfectly coincide with the experimental data across the full-size range. Particle diameters span from approximately 40 nm to around 140 nm, with the distribution peaking at a modal diameter of roughly 75 nm and the majority of particles concentrated between 65 and 95 nm. The asymmetric tail extending toward larger diameters reflects the natural spread of the γ' precipitate population.

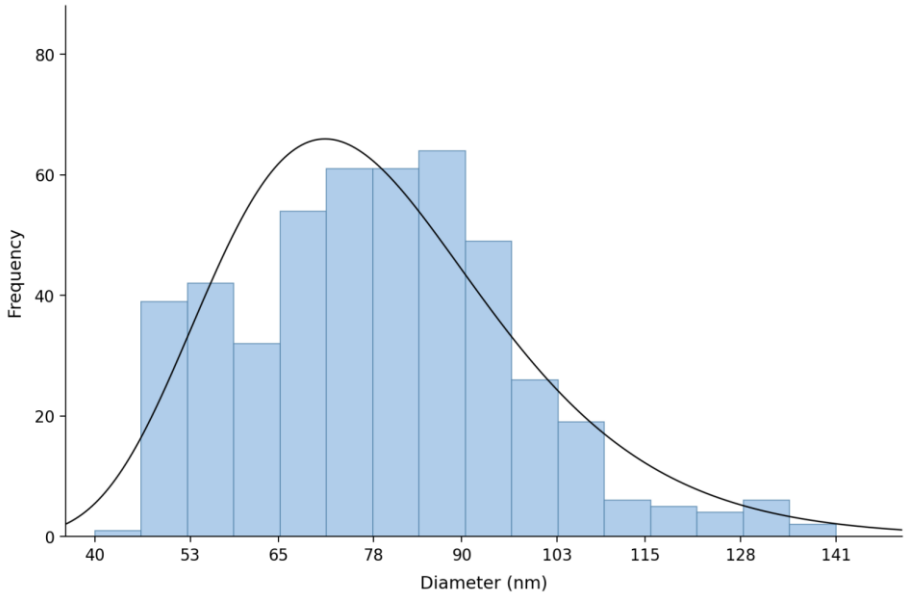

Figure 3.31: Size distribution histogram of secondary γ' precipitates measured in the HIP 1220 SOL 1220 sample, with a log-normal curve fitted to the data.

Tertiary γ' particles are also visible at high magnification along the grain boundaries, as shown in Figure 3.32, with diameters approximately half those of the secondary γ', ranging between 25 and 40 nm. Given the rapid cooling rate, these particles were able to nucleate but experienced very limited growth. The intergranular tertiary γ' is notably coarser than its intragranular counterpart, which is only discernible as a light grey background in the channels between secondary γ' particles.

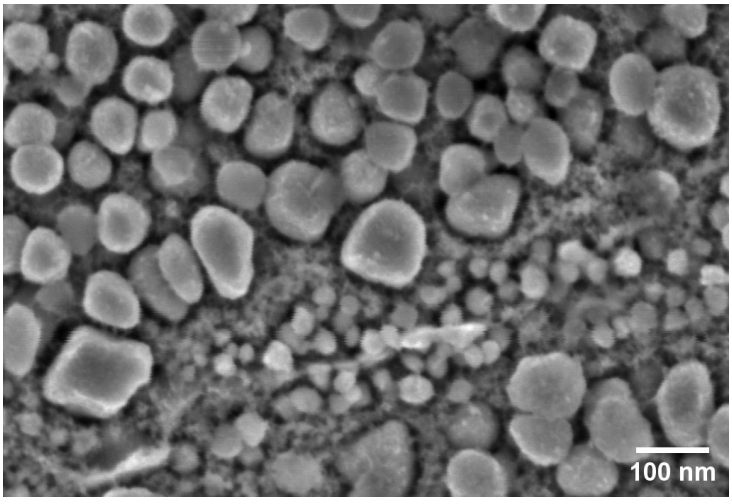

Figure 3.32: SE image of grain boundaries where tertiary γ' is observable.

Hardness measurements were carried out on both samples to complement the microstructural observations. The reference baseline for this series, established from the post-HIP 1220 condition, is 339 HB10. As observed in the HIP STD series, both samples exceed this value: the HIP 1220 SOL 1220 sample reaches 355 ± 3 HB10 and the HIP 1220 SOL 1230 sample reaches 363 ± 9 HB10. The increase relative to the baseline is comparable to that recorded in the HIP STD series at the same solution temperatures. The difference between the two samples, when the respective deviations are considered, is modest and may not be statistically significant.

Vertical grain size measurements were also performed on both samples, yielding values of 135 ± 6 µm for the HIP 1220 SOL 1220 sample and 146 ± 11 µm for the HIP 1220 SOL 1230 sample. Both values are equal to or slightly above those recorded in the HIP STD series at the same solution temperatures, suggesting that the solution treatment temperature remains the dominant variable governing grain growth, with the higher HIP temperature contributing only a modest additional effect. The wide deviations observed in both samples, however, prevent definitive conclusions from being drawn. The HIP 1220 SOL 1230 sample presents the highest grain size among all samples examined so far, consistent with it having experienced the highest combined HIP and solution treatment temperatures. The particularly wide scatter in this sample also points to a degree of microstructural inhomogeneity, likely associated with the extensive eutectic damage discussed above.

3.2.3. Effect of temperature: HIP performed at 1240 °C

The last HIP treatment temperature considered was 1240 °C. Based on the results from the previous series, only a solution treatment at 1220 °C was selected for this condition. Indeed, at a HIP temperature of 1220 °C, the sample solution treated at 1230 °C already showed extensive signs of microstructural degradation, and at both HIP temperatures previously investigated, samples solution treated at 1240 °C exhibited severe damage. The primary objective of this trial was therefore to assess whether a solution treatment below the solidus, combined with a preceding HIP at super-solidus temperature, yields a microstructure free of liquid-derived features.

Already at the macroscopic scale, signs of liquid formation were immediately apparent. A large number of shrinkage pores was identified, and unlike in the previous samples, these are not located in the vicinity of unmelted powder particles but are consistently associated with newly formed mixed carbides, clearly recognisable by their light grey contrast in BSE imaging. The pores are found both within the grain interior (Figure 3.33a) and at grain boundaries, where a characteristic row of primary MC carbides is also visible (Figure 3.33b).

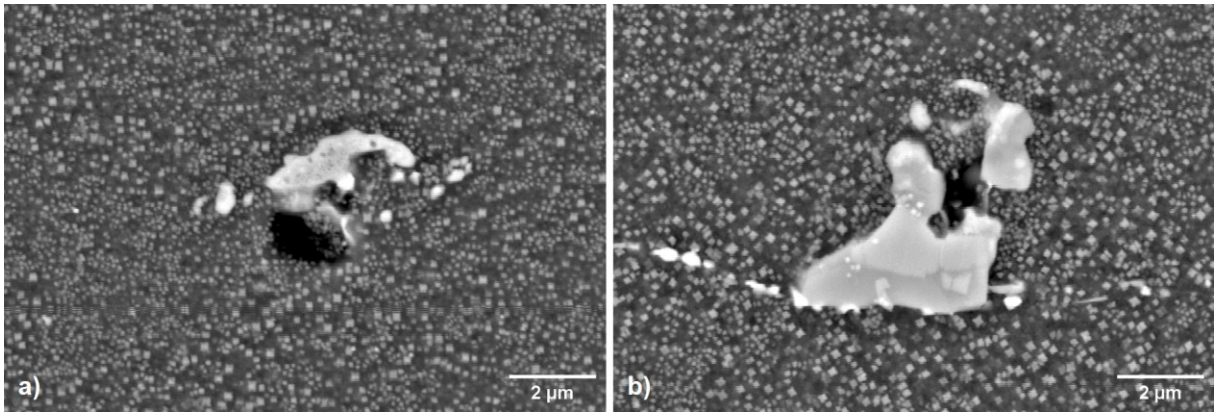

Figure 3.33: BSE images of shrinkage pores in the HIP 1240 SOL 1220 sample, located a) within the grain interior and b) at the grain boundary.

Eutectic structures were also identified. In some cases, lamellar structures are present without any nearby morphologically complex carbides, as shown in Figure 3.34. In this region, a large eutectic zone at the grain boundary is surrounded by a high density of small primary MC carbides, yet no complex carbides of the type observed in previous samples are present, despite some features of similar contrast being visible. These differ entirely in size and morphology. In other regions, by contrast, shrinkage pores are found in association with mixed carbides, as discussed above. The two types of regions likely reflect different degrees of local damage introduced during the super-solidus HIP treatment.

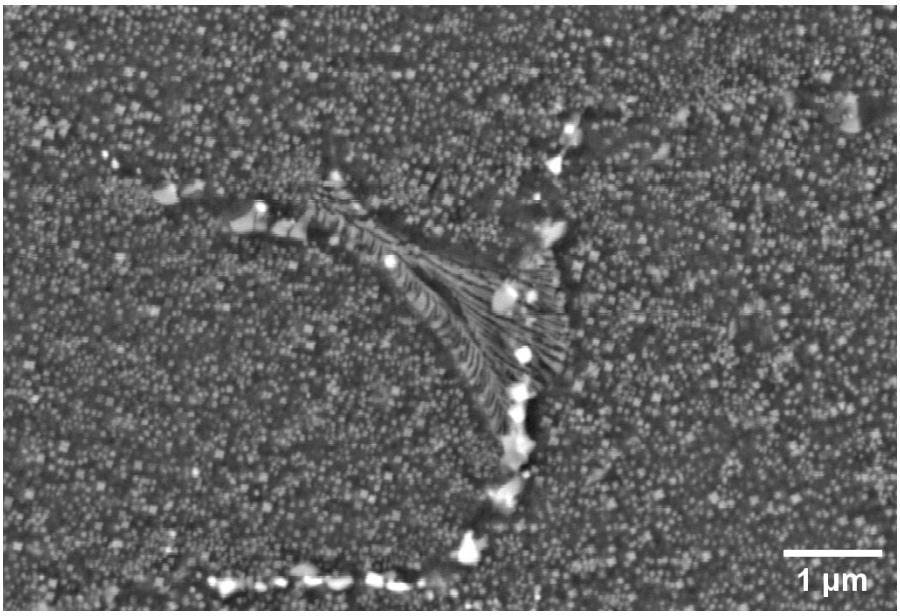

Figure 3.34: BSE image of a eutectic region.

In the most severely affected zones, the liquid-derived carbides were sufficiently stable to survive solution treatment at 1220 °C without fully dissolving, leaving behind the associated porosity. In the less severely affected regions, both the mixed carbides and the eutectic formed during the super-solidus HIP treatment dissolved during the subsequent solution treatment at 1220 °C, since the solution temperature remained below the solidus and no new liquid formed.

However, the local elemental segregation bands inherited from the eutectic regions were not fully homogenised, as the redistribution of Ta is particularly slow owing to its exceptionally low diffusivity in nickel, the lowest among the γ'-forming elements. Upon cooling from the solution temperature, these residual segregation bands, enriched in γ'-forming elements, provided preferential nucleation sites for γ', which precipitated in a lamellar morphology rather than as the discrete particles observed elsewhere in the microstructure.

Focusing on the most severely affected zones, such as that shown in Figure 3.35, large morphologically complex mixed carbides are clearly visible. Their presence confirms that the local damage introduced during the super-solidus HIP treatment was too severe to be fully remediated by solution treatment at 1220 °C.

The carbide shown in this figure is particularly illustrative, as it presents a central void likely resulting from shrinkage of the liquid upon solidification, around which the surrounding microstructure captures the full solidification sequence in a single field of observation, transitioning from the carbide at the periphery through a eutectic region located in the lower part of the void and finally to the regular γ' microstructure toward the centre.

Figure 3.35: Detailed SE image of a large mixed carbide.

Turning to the grain boundary microstructure, some regions exhibit extremely smooth boundary profiles. As shown in Figure 3.36 not only are the boundaries entirely devoid of corrugations, but the particles located along them, whether primary γ' or carbides, also adopt a markedly elongated morphology with one flat side aligned along the boundary. This suggests that the boundary geometry strongly constrains the shape of the precipitates, imposing a straight interface on the side in contact with the boundaries.

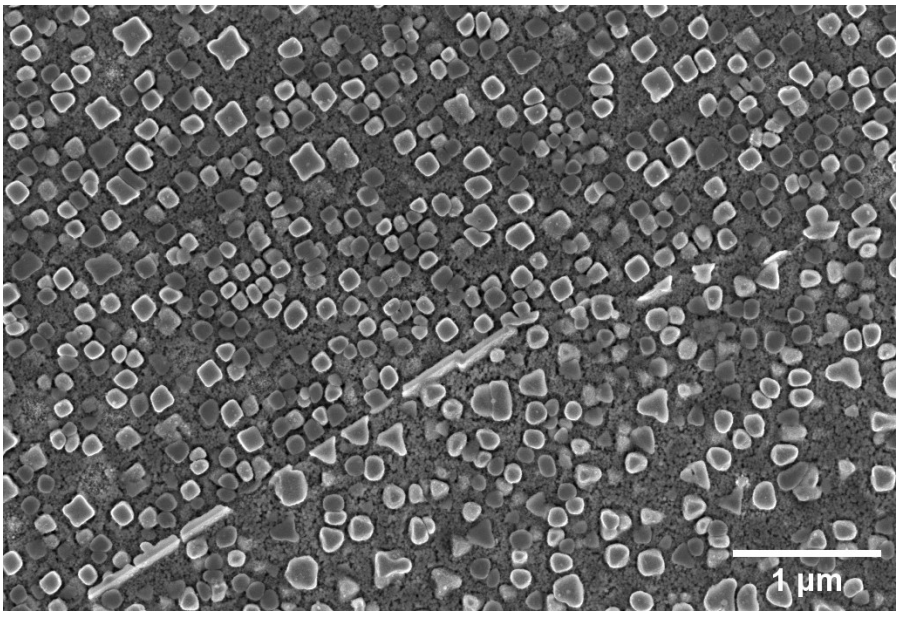

Figure 3.36: SE image of a grain boundary.

Among all the differences observed between this sample and the others, the most striking concerns the secondary γ' particles, shown in detail in Figure 3.37. The particles exhibit a markedly different morphology compared to all previous samples, being

considerably more cuboidal, as can be seen also in previous images, with some presenting rounded corners and others approaching a nearly perfect cubic shape. Beyond morphology, their size and distribution are also significantly different: the average equivalent diameter is 122.6 ± 9.8 nm and the volume fraction is 30.1 ± 3.7 %.

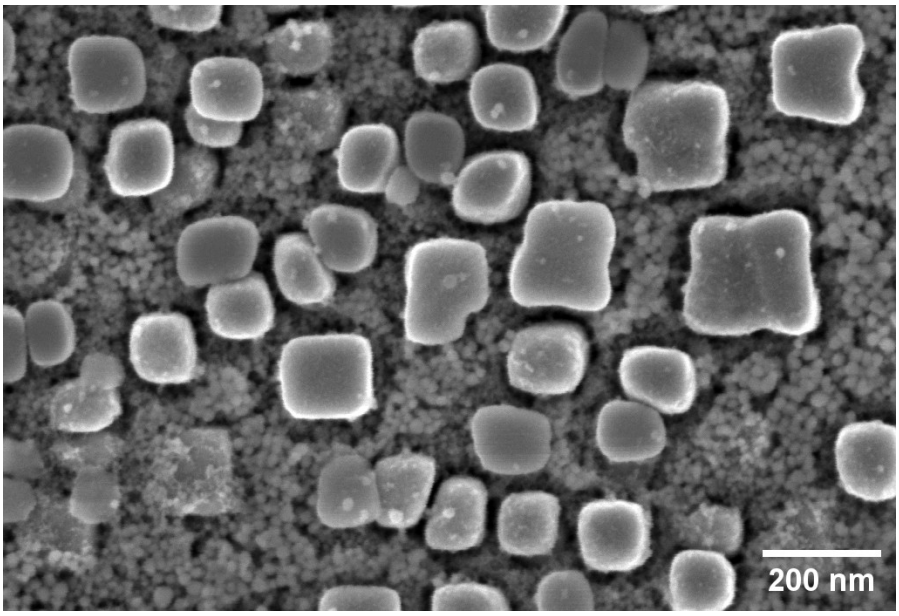

Figure 3.37: SE image of secondary and tertiary γ' precipitates inside a grain.

A statistical analysis of the γ' particle size distribution is presented in Figure 3.38. The population follows a log-normal bimodal distribution, although the fit, while reasonable, does not perfectly match with the experimental data. Particle diameters span from approximately 60 nm to around 240 nm, with the first peak at 90 nm and the second at 130 nm.

The value of the second peak is particularly noteworthy, as it is approximately twice that measured in all previous samples. This is not coincidental: as clearly visible in the images, many particles are the result of coalescence between adjacent secondary γ' particles, and in several cases, particles can be observed in contact with one another, indicating that coalescence is ongoing. This phenomenon has been documented in the literature during cooling from supersolvus temperatures, where precipitates develop non-equilibrium interfaces that reduce their energy through particle coalescence, forming necked regions between adjacent γ' [74]. The cuboidal morphology is consistent with this increased size: as precipitates grow, whether by diffusion-mediated coarsening or coalescence, the elastic misfit energy becomes dominant over the interfacial energy, making the cuboidal shape the configuration of minimum total energy [75] [76].

Beyond coalescence, the overall increase in size is also likely related to the different thermal history of this sample. A plausible interpretation is that the higher HIP temperature produces a matrix more heavily supersaturated in γ'-forming elements at

the end of the subsequent solution treatment. According to classical nucleation theory, a higher degree of supersaturation lowers the nucleation barrier, favouring precipitation at higher temperatures during cooling where diffusivity is greater. This results in a lower nuclei density with greater solute availability per particle and consequently more extensive growth. A similar temperature dependence of secondary γ' size was reported by Boonlert et al. in DZ125, although in that case part of the effect was attributed to incomplete dissolution of primary γ' [76]. A comparable observation was made by Kenevisi et al. for René 80, where coarsening was attributed to the reduced interfacial energy and coherent strain energy of the matrix/precipitate interface at elevated temperatures [77].

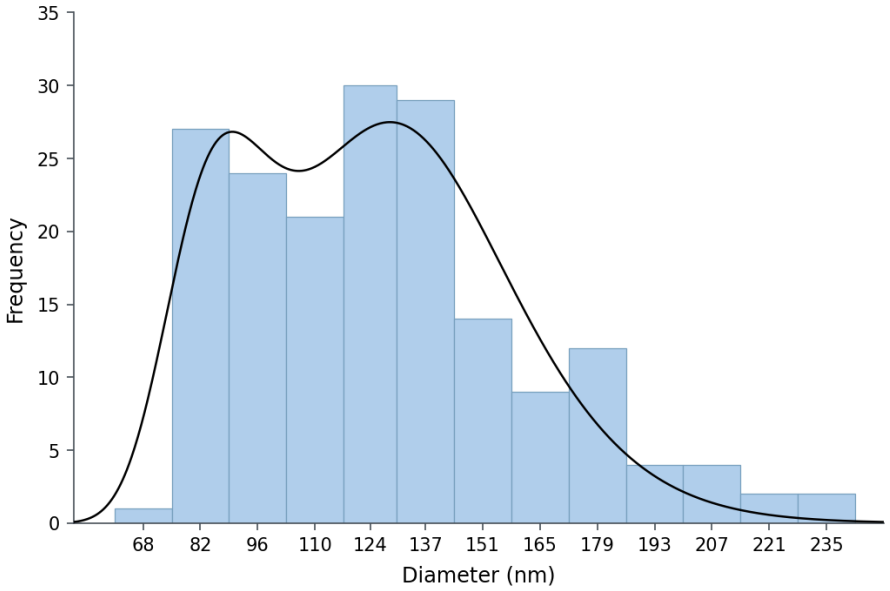

Figure 3.38: Size distribution of secondary γ' precipitates in the HIP 1240 SOL 1220 sample, with a bimodal log-normal curve fitted to the data.

The differences in γ' size, morphology, and volume fraction have a direct impact on mechanical properties. This sample presents the lowest hardness among all post-solution treatment samples analysed so far, with a value of 341 $\pm$ 7 HB10. The reduced hardness is consistent with the lower γ' volume fraction, which is approximately 10% below that of the other samples, since a lower precipitate fraction generally translates into reduced strengthening. The wider inter-precipitate channels, which scale directly with γ' size, may also contribute to the hardness reduction, although their influence is more complex and warrants a more detailed treatment beyond the scope of this discussion.

A further notable difference, confirmed by Figure 3.37, is the clearly visible tertiary γ' population, which unlike in previous samples is observable not only at grain boundaries but also within the grain interior. Measurements reveal that in these regions tertiary γ' particles can reach diameters of up to 45 nm, the largest recorded across all samples examined.

Last analysis was conduced on grain size. The sample exhibits a vertical grain size of 140 ± 4 µm, the highest of all the samples solution treated at 1220 °C, but lower than the sample HIPed at 1220 and solutioned at 1230 °C. So probably, the greatest influence on this parameter is given by the solution, rater than HIP process.

3.2.4. Effect of cooling rate

Following the solution treatment trials with air cooling, the effect of cooling rate was investigated by replacing air cooling with furnace cooling at approximately 40 °C/min. Since the results from the previous series consistently identified 1220 °C as the optimal solution temperature, this condition was applied to all three HIP series (1180 °C, 1220 °C, and 1240 °C) in this phase of the study.

It should be noted at the outset that the cooling rate has a negligible influence on certain microstructural features, namely those that do not undergo transformation during cooling. Grain size, for instance, is determined by growth at high temperature and is therefore unaffected by the subsequent cooling rate. The same applies to most carbides, which are highly stable and require extended holding times to transform, as occurs during aging. These expectations were confirmed by preliminary observations.

As expected, the first two samples (HIP STD SOL 1220-S and HIP 1220 SOL 1220-S) showed no eutectic regions at grain boundaries, and the features present were identical to those of the corresponding fast-cooled samples. The HIP 1240 SOL 1220-S sample, by contrast, exhibited substantial microstructural damage, with dendritic γ' structures and associated mixed carbides identified at grain boundaries and triple junctions (Figure 3.39), similarly to what was observed in its fast-cooled counterpart. This confirms that slow cooling is neither sufficient nor effective in promoting rehomogenisation of liquid-derived phases formed at grain boundaries during the HIP treatment.

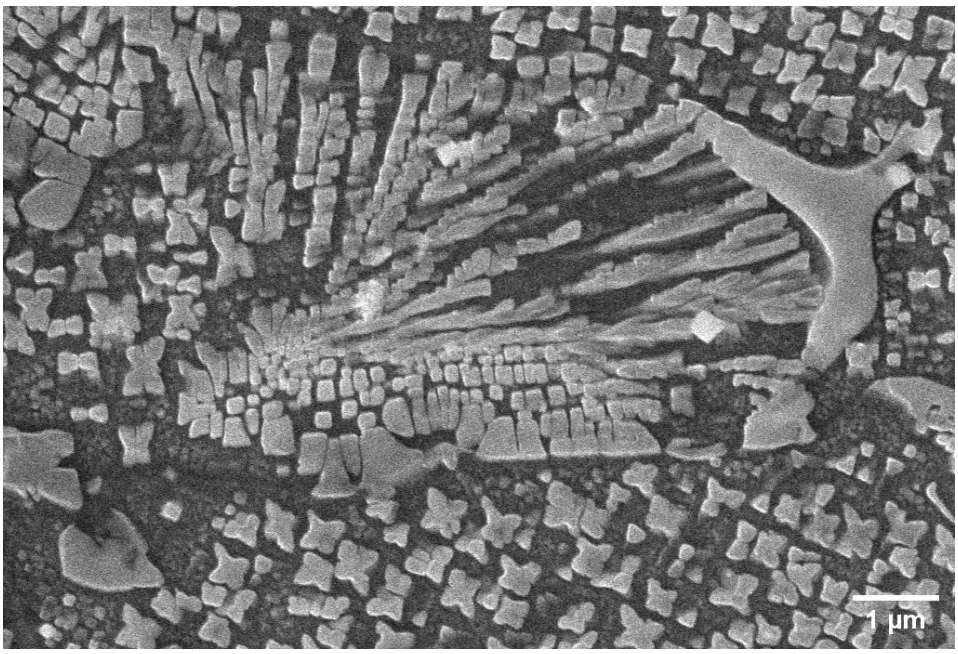

Figure 3.39: SE image of a eutectic microstructure in the HIP 1240 SOL 1220-S sample

Very differently from other microstructural features, instead the γ' precipitates were strongly influenced by the cooling rate, indeed, during the precipitation phase after the

holding at solution temperature, if longer times were passed in the transformation range, the particles were strongly influenced. For this reason, evaluation on the γ' quantitative aspects were conducted.

The γ' precipitates, on the other hand, are strongly influenced by the cooling rate, as the slower thermal cycle allows more time for precipitation and growth within the transformation range. Quantitative data on γ' volume fraction and average equivalent diameter are presented in Table 3.5. It should be noted that, due to the strong presence of tertiary γ' and the occurrence of coalescence between secondary particles, the images obtained for these samples differ substantially from those of the fast-cooled series and the measurements cannot be directly compared. The prominent tertiary γ' population, which is larger in size than in the previous samples, can be distinguished from the secondary γ', allowing measurements to be taken exclusively on the secondary population. This partly explains the lower volume fraction relative to the fast-cooled samples, as well as part of the increase in average diameter.

Table 3.5: Values on the secondary γ' population acquired from image analysis with ImageJ.

Sample	**% γ' (vol %)**	**Average γ' diameter (nm)**
HIP STD SOL 1220-S	37.7 ± 3.9	281.3 ± 9.7
HIP 1220 SOL 1220-S	38.2 ± 1.9	293.0 ± 8.9
HIP 1240 SOL 1220-S	34.1 ± 1.1	262.6 ± 12.5

The most notable difference concerns the secondary γ' diameter, which increases dramatically relative to the fast-cooled counterparts, reaching a 300% growth for the HIP 1220 SOL 1220-S sample. For the HIP 1240 SOL 1220-S sample, where the fast-cooled particles already had a diameter of approximately 120 nm, the increase is around 115%. The diameter increase is evident also from qualitative observation as well and is further amplified by coalescence between secondary particles. Regardless of the specific values, it can be stated with confidence that the slower cooling rate promotes a coarse γ' microstructure. In terms of volume fraction, the highest value is recorded for the HIP 1220 SOL 1220-S sample at 38.2%, followed by 37.7% for HIP STD SOL 1220-S and 34.1% for HIP 1240 SOL 1220-S.

To further characterise the secondary γ' size distribution, a histogram analysis was performed on the HIP 1220 SOL 1220-S sample, chosen as representative of the series given the comparable distribution shapes observed across all three samples, with results presented in Figure 3.40.

Unlike the fast-cooled samples, which exhibited a well-defined log-normal distribution with a clear single peak, the distribution profile in this case is considerably broader and more irregular, with no dominant peak clearly identifiable. This is attributed to the

coexistence of multiple particle populations at different stages of coalescence, which prevents the emergence of a well-defined statistical distribution. The distribution spans from approximately 113 nm to just above 467 nm, a range substantially wider than that observed in the fast-cooled samples, and the relatively uniform frequency across a wide central region further reflects the advanced degree of coarsening and the microstructural heterogeneity introduced by the slower cooling rate.

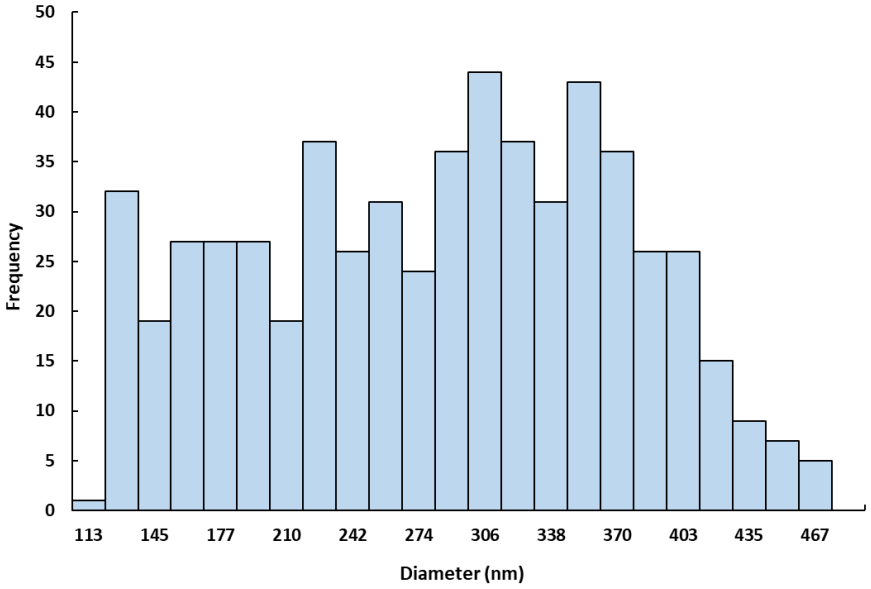

Figure 3.40: Size distribution histogram of secondary γ' precipitates measured in the HIP 1220 SOL 1220-S sample.

Beyond the quantitative differences, the SE images in Figure 3.41 reveal that the particle morphology is completely different from that observed in the fast-cooled samples. Rather than adopting a cuboidal or near-spherical shape, the particles present a lobed, fan-like morphology, characteristic of secondary γ' precipitates in slow-cooled solutioned samples prior to aging. This morphology results from the coalescence of initially cuboidal or spherical particles, a process that cannot occur under fast cooling conditions. Numerous examples of particles in various stages of coalescence are visible throughout the images, and in several cases necked regions between adjacent precipitates can be clearly identified, confirming that coalescence is an active mechanism under slow cooling conditions.

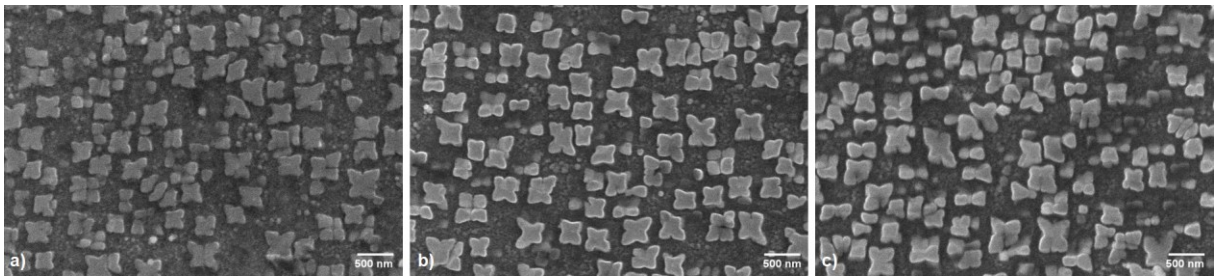

Figure 3.41: SE images of secondary γ' inside the grains in a) HIP STD SOL 1220-S sample, b) HIP 1220 SOL 1220-S sample and c) HIP 1240 SOL 1220-S sample.

These differences are directly reflected in the hardness values (Figure 3.42), which are markedly lower than those of the fast-cooled samples, particularly for the HIP STD and HIP 1220 series, where the reduction amounts to between 20 and 30 HB10. Among the three slow-cooled samples, HIP 1220 SOL 1220-S achieves the highest hardness at 332 HB10, though the difference with the other two is modest, both presenting values of approximately 329 HB10. Notably, despite the different HIP temperatures, the three samples converge toward a narrow hardness range, suggesting that under slow cooling conditions solution becomes the dominant treatment governing the final hardness, with the HIP temperature playing a comparatively secondary role. The HIP 1240 SOL 1220-S sample shows a smaller hardness reduction relative to its fast-cooled counterpart compared to the other two samples, which is consistent with the already coarse γ' microstructure produced by the HIP 1240 fast-cooled condition, where the additional coarsening induced by slow cooling has a limited further effect.

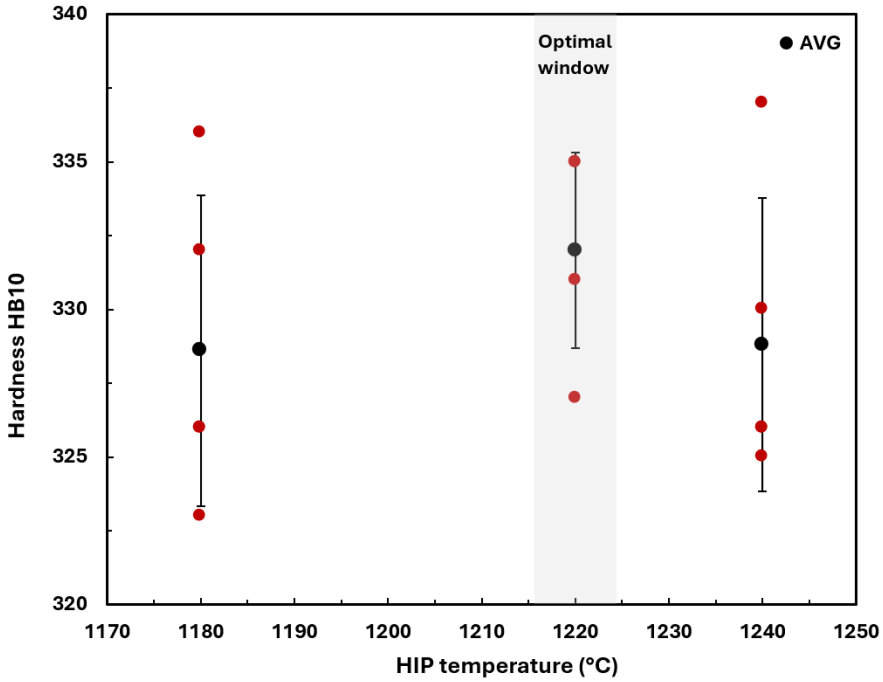

Figure 3.42: Hardness of the slow-cooled samples as a function of HIP temperature

3.2.5. Discussion of solution treatment results

This chapter presents a discussion of the main microstructural features observed in the solution-treated samples, integrating the quantitative data on γ', grain size, and hardness with specific information on SAM and relevant literature findings.

The blocky MC carbides identified in this alloy represent the first microstructural element to be discussed, and are labelled as TaC, supported by several converging lines of evidence. Firstly, observing the microstructure of post-solution samples these carbides remain stable even at elevated temperatures, persisting through solution treatments well above both the γ' solvus and the solidus, with regions of locally elevated carbide density surviving even the most aggressive thermal cycles. TaC is indeed widely recognised as one of the most thermally stable MC carbide types at elevated temperatures.

Second, previous work on SAM by Dörries et al. confirms that the microstructure of as-printed SAM consists of a supersaturated γ matrix with TaC on grain and cell boundaries, with no evidence of γ'. After heat treatment, the microstructure develops fine cubic γ' and TaC within the grains, alongside coarser γ' and TaC at grain boundaries. The same work reports that TaC remains stable in Thermo-Calc simulations up to 800 °C and that the presence of Zr may further stabilise TaC in SAM, slowing its dissolution [78] .

Third, EDS analysis performed in this work is consistent with the Thermo-Calc simulations on carbide composition reported by Bersano, as shown in Figure 3.43: the blocky cubic carbides present a higher Ta content relative to Hf, whereas the morphologically complex carbides formed during solution treatment just above the solidus show a higher Hf content, in full agreement with the simulated predictions [71].

This distinction is also corroborated by the work of Huang et al. on compositionally similar alloys such as CM247LC, where blocky Ta-rich MC carbides are reported to be highly stable, in contrast to morphologically complex carbides derived from the liquid. In the same work, blocky carbide particles at grain boundaries are shown to function as obstacles to grain boundary sliding and barriers to crack propagation, contributing to improved creep rupture life and reduced creep rate. Carbide morphology and spatial distribution are therefore crucial factors in determining the creep behaviour and ductility of nickel-based superalloys, though coarse or script-like carbides at grain boundaries may conversely promote moderate-temperature embrittlement [45].

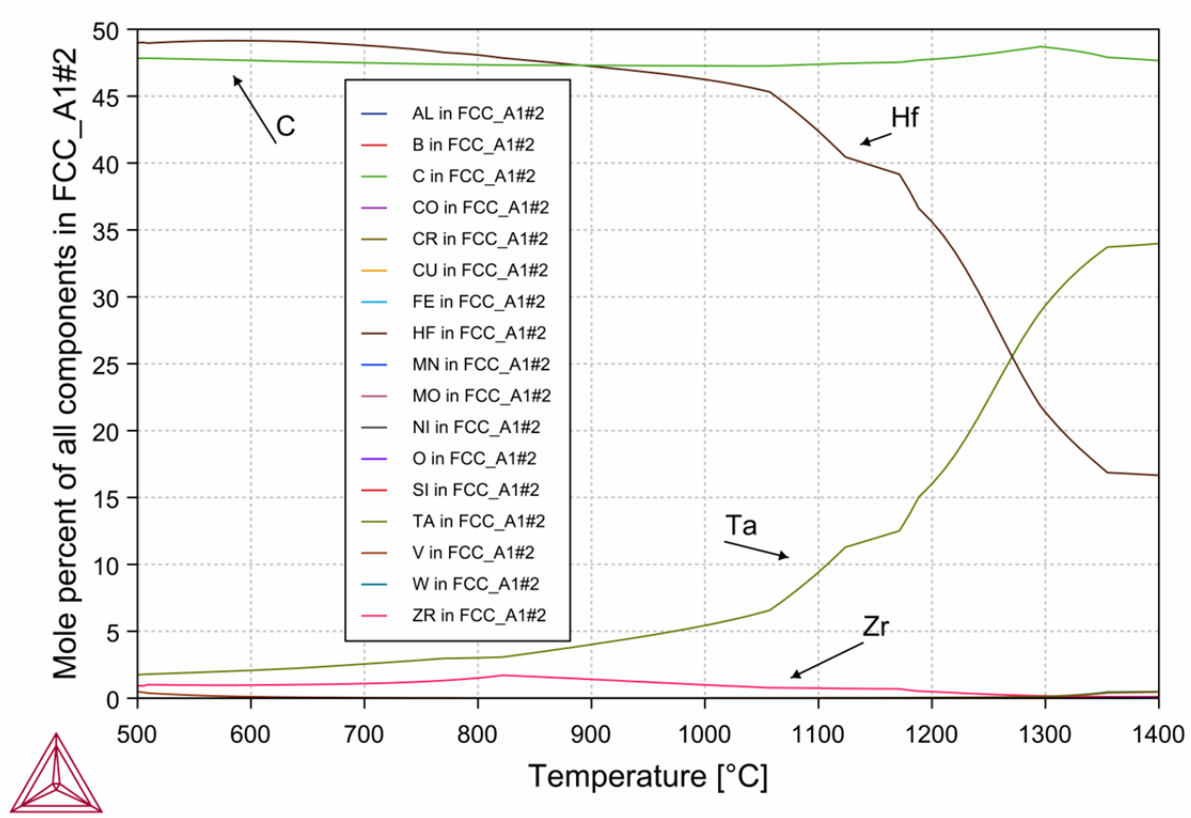

Figure 3.43: MC carbide composition according to Thermo-Calc *[71]*.

The formation of morphologically complex carbides, also referred to as skeletal carbides, is associated with liquid formation and is typically accompanied by lamellar or dendritic eutectic structures in the surrounding regions. Their formation is driven by competitive nucleation from residual liquid during solidification, with eutectic carbides nucleating at high-energy sites and growing along grain boundaries [79] [80].

The resulting coarse and irregular morphology reflects the local solidification conditions and the degree of elemental segregation in the final liquid fraction. Once formed, skeletal carbides are extremely difficult to dissolve during subsequent processing, as evidenced by their persistence in the HIP 1240 SOL 1220 sample even after solution treatment, a behaviour consistent with reports that such carbides survive both hot rolling and solution treatment [79].

From a mechanical standpoint, their continuous network character introduces stress concentrations at grain boundaries, making them preferential sites for fracture initiation and propagation. Compared to alloys with blocky carbide distributions, systems containing skeletal carbides exhibit higher local strain and lower tensile strength, though they retain comparatively higher elongation owing to more uniform slip distribution and the activation of multiple slip systems. The hardening contribution of carbides scales with volume fraction and inversely with particle size, and the transition from skeletal to blocky morphology, by increasing the volume fraction while reducing the effective diameter, enhances the overall hardening effect [81].

Following this qualitative analysis, a comparative overview of all samples within the optimal solution temperature range was conducted, with results summarised in Table 3.6 and Table 3.7.

Table 3.6: Summary of hardness and microstructural data for the fast-cooled solution treated samples within the optimal temperature range.

Sample	**Hardness (HB10)**	**% γ′**	**γ′ diameter (nm)**	**Grain size (µm)**	**Eutectic**
HIP STD SOL 1220	358 ± 9	43.6 ± 5.9	62.2 ± 4.4	135 ± 13	
HIP STD SOL 1230	353 ± 5	39.7 ± 1.1	59.4 ± 1.4	130 ± 8	✓
HIP 1220 SOL 1220	355 ± 3	46.5 ± 1.7	73.4 ± 3.2	135 ± 6	
HIP 1220 SOL 1230	363 ± 9	43.0 ± 3.0	66.4 ± 2.8	146 ± 11	✓
HIP 1240 SOL 1220	341 ± 7	30.1± 3.7	122.6 ± 9.8	140 ± 4	✓

Table 3.7: Summary of hardness and microstructural data for the slow-cooled solution treated samples within the optimal temperature range.

Sample	**Hardness (HB10)**	**% γ′**	**γ′ diameter (nm)**	**Grain size (µm)**	**Eutectic**
HIP STD SOL 1220-S	329 ± 5	37.7 ± 3.9	281.3 ± 9.7	135 ± 13	
HIP 1220 SOL 1220-S	332 ± 3	38.2 ± 1.9	293.0 ± 8.9	135 ± 6	
HIP 1240 SOL 1220-S	329 ± 5	34.1 ± 1.1	262.6 ± 12.5	140 ± 4	✓

Examining the fast-cooled samples, a clear pattern emerges with increasing HIP temperature. Between the HIP STD and HIP 1220 series, the secondary γ′ volume fraction increases slightly and hardness remains broadly comparable, with values ranging between 350 and 363 HB10 and γ′ fractions between approximately 40% and 47%. The secondary γ′ diameter is also consistent between these two series, falling within a narrow range of 59 to 73 nm. The HIP 1240 series, by contrast, presents markedly different values: the γ′ volume fraction drops to approximately 30%, the average diameter reaches 122 nm, and hardness falls to 341 HB10. The deterioration of these properties in the HIP 1240 series is attributed to the combined effect of the coarse γ′ microstructure and the formation of liquid-derived phases during the super-solidus HIP treatment. These results clearly indicate that exceeding a HIP temperature of 1220 °C leads to a significant and undesirable reduction in both hardness and γ′ volume fraction and should therefore be avoided.

A correlation analysis was also performed on the fast-cooled samples. As shown in Figure 3.44, a moderate positive correlation exists between γ′ volume fraction and hardness, described by a linear fit with $R^2 = 0.7223$. The fitted equation ($y = 1.0991x + 309.35$) suggests that each 5% increase in γ′ volume fraction corresponds to a hardness increase of approximately 5.5 HB10. Despite the scatter observed in some

samples, the trend is apparent and physically consistent. No other significant correlations were identified among the fast-cooled samples. For the slow-cooled series, the limited number of samples precludes a statistically meaningful correlation analysis.

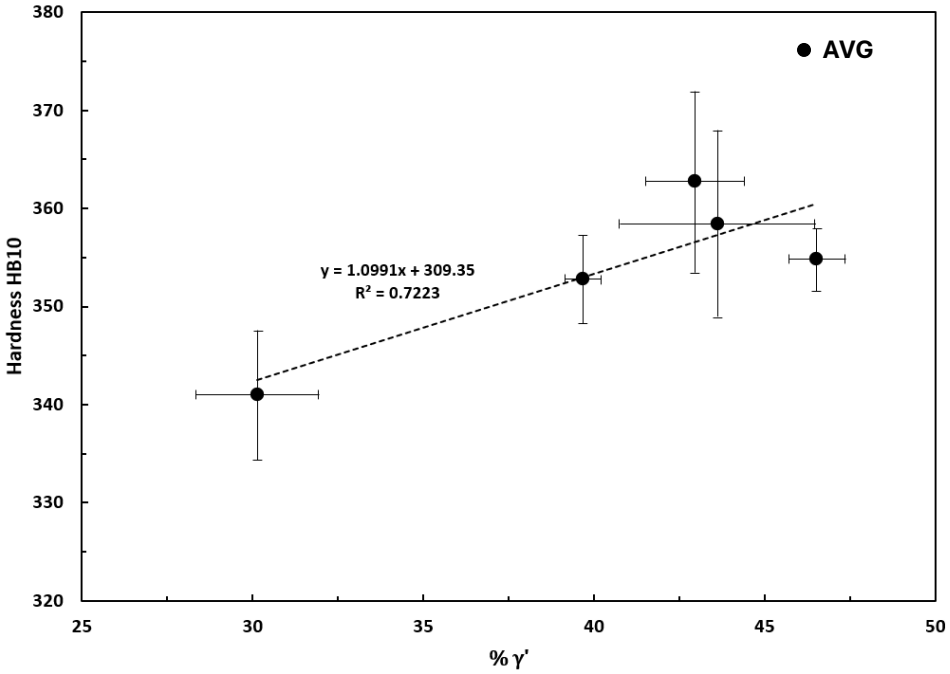

Figure 3.44: Correlation between secondary γ' volume fraction and hardness HB10 for the fast-cooled solution-treated samples.

Having established the main microstructural trends and identified the optimal processing conditions, it is useful to contextualise the results obtained in this work against the available literature data for this alloy and compositionally similar materials. This comparison serves both to validate the experimental findings and to assess how the microstructure achieved in this work relates to the targets and benchmarks reported for the alloy in service conditions.

The grain size values obtained in this work are consistent with those reported in the literature for this alloy. Dörries et al. report a grain size of approximately 100 µm for heat-treated samples [78], and a subsequent study by the same author records a value of 103 ± 68 µm after solution treatment at 1180 °C for 30 minutes on a SAM sample with 1.3% Hf [82]. A further source reports a grain size of 105 ± 46 µm after solution treatment at 1230 °C for 4 hours on the same composition. A grain size exceeding ASTM 5, corresponding to an equivalent diameter of approximately 65 µm, is identified as advantageous for achieving the creep rupture life target [53]. All samples examined in this work satisfy this requirement by a considerable margin.

The γ' volume fraction values are similarly in good agreement with the literature. Bersano reports a value of approximately 39% at a solution temperature of 1220 °C without prior HIP treatment, which is consistent with the results obtained in this work for the corresponding condition [71]. Technical documentation for the alloy indicates a

moderate to high γ' volume fraction, with an indicative value of approximately 30%, which represents a lower bound that is met or exceeded by all samples examined here [52].

Regarding γ' size, technical documentation for the alloy indicates a target primary γ' diameter of several hundred nanometres after aging [82]. No reference data for secondary γ' size and hardness measured under equivalent conditions were found in the available literature, making it impossible to establish target ranges for direct comparison at this stage for these specific properties.

Based on all the observations discussed above, a preferential direction for further development can be identified. The presence of eutectic regions derived from incipient melting represents an absolute constraint to be avoided, as it not only introduces detrimental microstructural features but also increases porosity through the formation of shrinkage pores. All samples in which at least one of the two treatments, HIP or solution, was performed above 1220 °C exhibited eutectic regions characterised by dendritic microstructures. Beyond this constraint, the main objectives are to maximise grain size, hardness, and γ' volume fraction, all of which are favourable for creep resistance and mechanical performance. Given the positive correlation between treatment temperature and grain size demonstrated in Chapter 3.2.1, and the consistently superior microstructural and mechanical results obtained at 1220 °C, both the HIP and solution treatment temperatures of 1220 °C are identified as the optimal conditions for further steps in the heat treatment optimization.

3.3. Aging

The aging trials were performed exclusively on the HIP 1220 SOL 1220-S sample, which was heat treated with a controlled and slower cooling rate. This condition was selected as it represents the optimal parameter combination identified in the preceding steps, and furnace cooling was preferred over air quenching as it is more representative of the industrially viable approach for large components, where rapid cooling would introduce unacceptable thermal gradients.

In aging treatment, the two primary variables are temperature and holding time. In this initial phase of aging trials, a relatively short holding time of 4 hours was adopted, with the focus placed on investigating the effect of temperature. The temperature selection was guided by the objectives of the treatment and the thermal data obtained from DSC analysis.

Two main aims were pursued. The first was to achieve the desired γ' morphology, size, and volume fraction. Regarding morphology, the target is a cuboidal shape, replacing the fan-like morphology typically observed in post-solution samples cooled at moderate rates. Regarding volume fraction, the objective was to increase it by promoting tertiary γ' precipitation, without inducing excessive coarsening of the secondary γ' population. Coarsening would widen the inter-precipitate channels and reduce their effectiveness in impeding dislocation motion. To obtain an effective modification of the γ' population, the treatment temperature must be above the γ' formation temperature, identified at approximately 600 °C by DSC.

The second aim was to promote carbide precipitation at grain boundaries, where carbides act as beneficial pinning particles. DSC data indicate that $M_{23}C_6$ forms in the 1010-1020 °C range, which informed the upper end of the temperature selection.

The lowest, 600 °C, is close to the γ' formation peak and was included to characterise the microstructure at this threshold, despite likely being too low for an effective aging treatment. A temperature of 800 °C was selected as an intermediate condition between the γ' and carbide formation peaks. The remaining three temperatures, 975 °C, 1000 °C, and 1025 °C, were chosen to investigate the carbide precipitation range and to assess whether treatment near 1000 °C leads to overaging, given the sensitivity of the microstructure in this interval.

3.3.1. Effect of temperature on sample HIP 1220-SOL 1220

The first aspect examined was the γ' microstructure within the grain interior. The secondary γ' morphology varies considerably across the five aging temperatures. In the sample aged at 600 °C (Figure 3.45a), the fan-like morphology remains clearly dominant, indicating that this temperature is insufficient to drive the transition toward a cuboidal shape. The particle size distribution is also notably heterogeneous, and tertiary γ' particles are observable in the channels between secondary particles.

Already at 800 °C (Figure 3.45b), the situation improves: secondary γ' particles begin to adopt a more cuboidal shape with a more uniform size distribution, while tertiary γ' remains clearly visible in the inter-particle channels. At 975 °C (Figure 3.45c), the majority of secondary particles are markedly cuboidal, with only occasional exceptions. However, early signs of excessive growth begin to appear, as coalescence between adjacent particles becomes relevant and some particles are clearly the result of the merging of two smaller ones. Tertiary γ' has almost entirely disappeared at this condition, and the secondary γ' size begins to approach the upper limit compatible with the desired final properties.

These trends become considerably more pronounced in the samples aged at 1000 °C and 1025 °C (Figure 3.45d and Figure 3.45e). While a well-defined cuboidal morphology is achieved, the particle size is substantially larger than in the lower-temperature samples, and regions almost entirely devoid of precipitates begin to appear, indicating the formation of very wide γ matrix channels. These channels are detrimental not only due to their width, but also because tertiary γ' has completely disappeared from the microstructure. The presence of tertiary γ' in the matrix channels is considered essential for achieving the target mechanical performance.

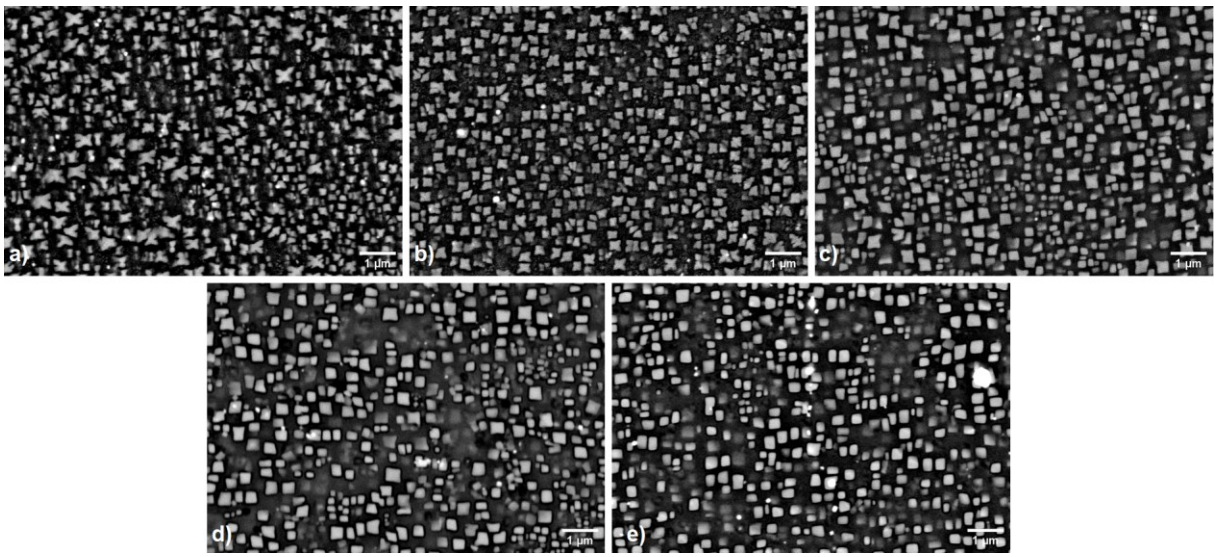

Figure 3.45: BSE images of γ' particles inside the grains of a) AG 600, b) AG 800, c) AG 975, d) AG 1000 and e) AG 1025 samples.

Despite these differences in morphology and size across the five temperatures, a common feature observed in all samples is the presence of regions with markedly different secondary γ' size within the same specimen, suggesting that longer holding times may be necessary to achieve a more homogeneous microstructure. This inhomogeneity could be very evident, such as in the sample treated at 975 °C, shown in Figure 3.46, though similar size gradients were observed across all samples and become more pronounced at higher treatment temperatures.

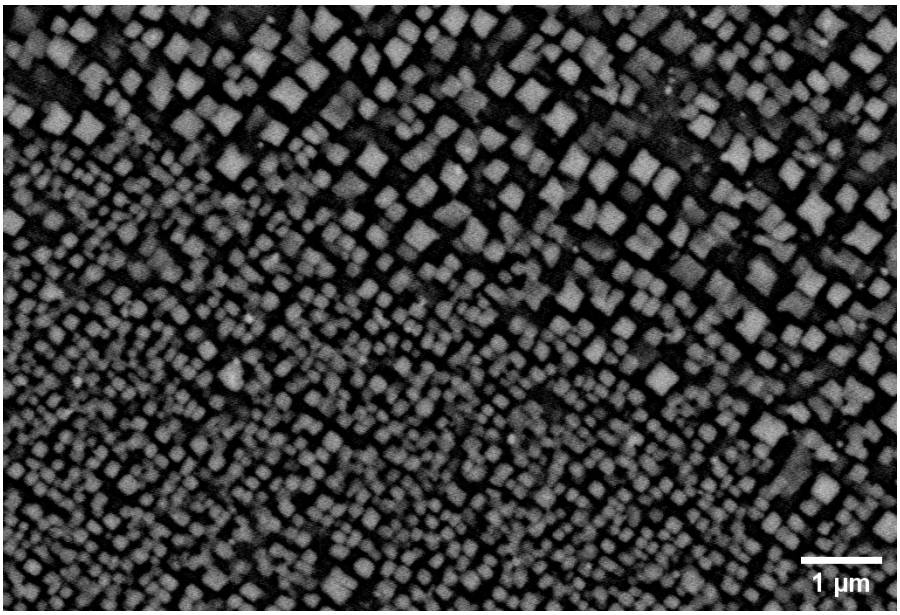

Figure 3.46: BSE image of inhomogeneous region with different γ' populations.

Turning to the grain boundary microstructure, all samples present broadly similar features, though samples treated at higher temperatures exhibit a greater density and size of primary γ' and carbide particles along the boundaries, consistent with the trends observed in the grain interior. This is well illustrated by the comparison between the AG 800 and AG 1000 samples shown in Figure 3.47, where in the former precipitates are only clearly visible at triple junctions, whereas in the latter the boundaries are decorated with large particles along their entire length.

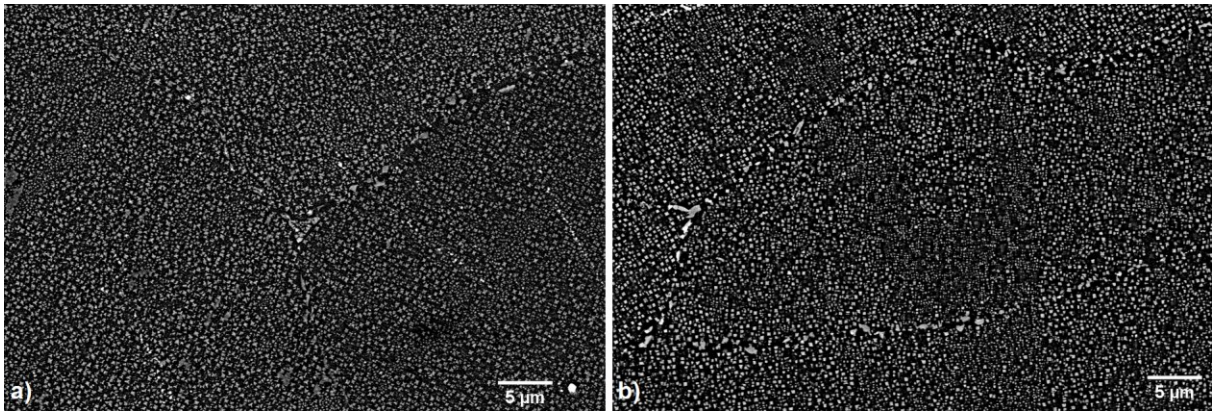

Figure 3.47: BSE images of grain boundary microstructure in a) AG 800 and b) AG 1000 samples.

Quantitative analysis of γ' size and volume fraction, summarised in Table 3.8, partially confirms the observations made above. It should be noted that these measurements were obtained from BSE images, which present a markedly different contrast from the SE images used for the solution-treated samples. Furthermore, the pronounced microstructural inhomogeneity of these samples results in regions with substantially different γ' size and volume fraction, meaning that the results are not directly comparable with those obtained in the previous sections.

Table 3.8: Secondary γ' volume fraction and average equivalent diameter for the five aging temperatures investigated.

Sample	**% γ' (vol %)**	**Average γ' diameter (nm)**
AG 600	34.9 ± 2.2	216.6 ± 9.1
AG 800	30.2 ± 2.3	208.4 ± 8.8
AG 975	31.0 ± 3.4	225.0 ± 3.9
AG 1000	23.3 ± 0.5	226.3 ± 7.4
AG 1025	27.9 ± 5.0	235.7 ± 14.6

Starting with particle size, the finest average equivalent diameter is recorded in the AG 800 sample at 208.4 nm, followed by AG 600 at 216.6 nm and AG 975 at 225.0 nm. The highest-temperature sample presents the largest secondary γ' particles at approximately 235.7 nm, though this value remains in the same range as those of AG 975 and AG 1000, in contrast to the more pronounced differences observed in γ' volume fraction.

The size distribution of the AG 800 sample was examined in greater detail, with results presented in Figure 3.48. Several fitting functions were tested, and the best agreement with the experimental data was achieved using a polynomial fit. The distribution spans a wide range, from approximately 113 nm to just below 390 nm, which is considerably wider than that observed in the fast-cooled solutioned samples, where only secondary γ' was measurable and the distribution was narrower and more symmetric, directly reflecting the effect of aging at 800 °C in promoting both tertiary γ' nucleation and secondary γ' growth. The breadth of the distribution is consistent with the coexistence of multiple γ' populations within the same sample. Two distinct peaks can be identified: the first, located at approximately 135 nm, is attributed to the tertiary γ' population, while the second, centred at approximately 260 nm, corresponds to the secondary γ'. The valley between the two peaks, reflects the size gap between the two populations and further supports their distinct origin.

The tail extending toward larger diameters is consistent with the presence of coarser secondary particles that have undergone limited coalescence or preferential growth. The

inability of a log-normal function to describe this distribution adequately, in contrast to the fast-cooled solution samples, is itself informative: it reflects the greater inhomogeneity of the precipitate population and the presence of two distinct γ' generations coexist with partially overlapping size ranges.

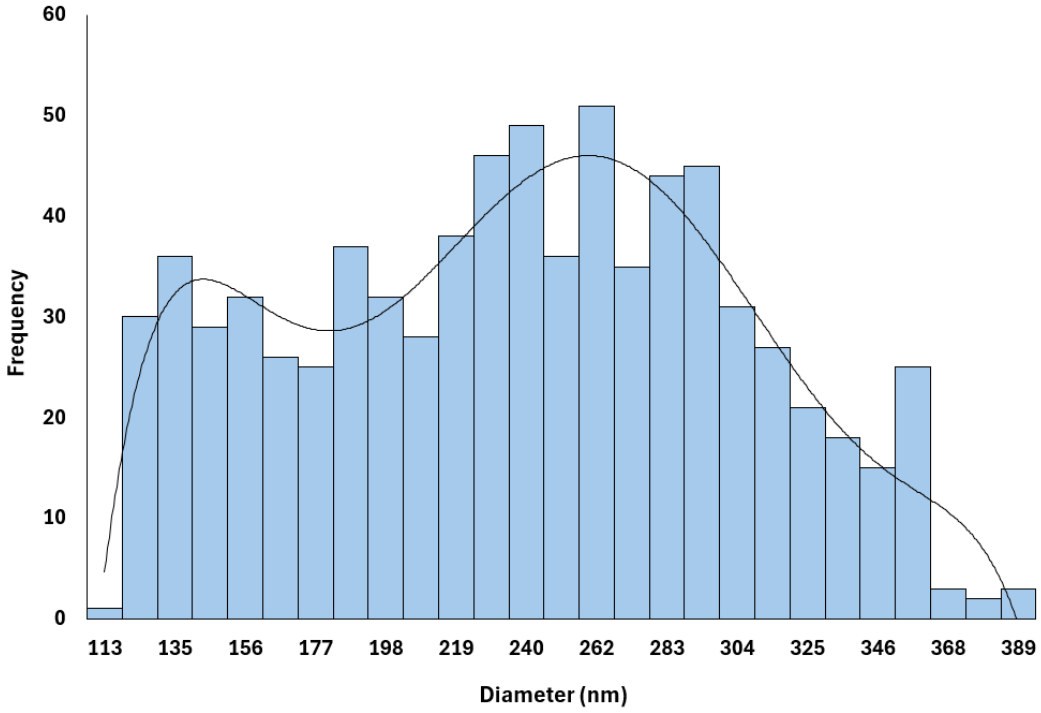

Figure 3.48: Size distribution histogram of γ' precipitates in the AG 800 sample, with a polynomial fitting curve.

In terms of volume fraction, the AG 600 sample presents the highest value at 34.9%, followed by AG 975 at 31.0% and AG 800 at 30.2%. It should be noted that both AG 600 and AG 800 contain a visible tertiary γ' population that is not captured by the image analysis, meaning that the total γ' fraction across all classes is likely considerably higher in these samples. The two highest-temperature samples present the lowest volume fractions, falling well below 30%. The large spread in values recorded across the three highest temperatures is consistent with the microstructural inhomogeneity observed qualitatively in these samples.

The relationship between γ' volume fraction and aging temperature is further illustrated in Figure 3.49, which shows a general decreasing trend with increasing temperature, described by a linear fit ($y = 0.0184x + 45.65$) with $R^2 = 0.6092$. The fitted equation suggests that each 100 °C increase in aging temperature corresponds to a reduction of approximately 2% in γ' volume fraction.

The moderate correlation reflects the wide scatter observed at higher temperatures, arising from the microstructural inhomogeneity of the secondary γ' population. Nevertheless, the overall decreasing trend is physically consistent with the progressive

dissolution of precipitates back into the matrix as the temperature approaches the γ′ solvus.

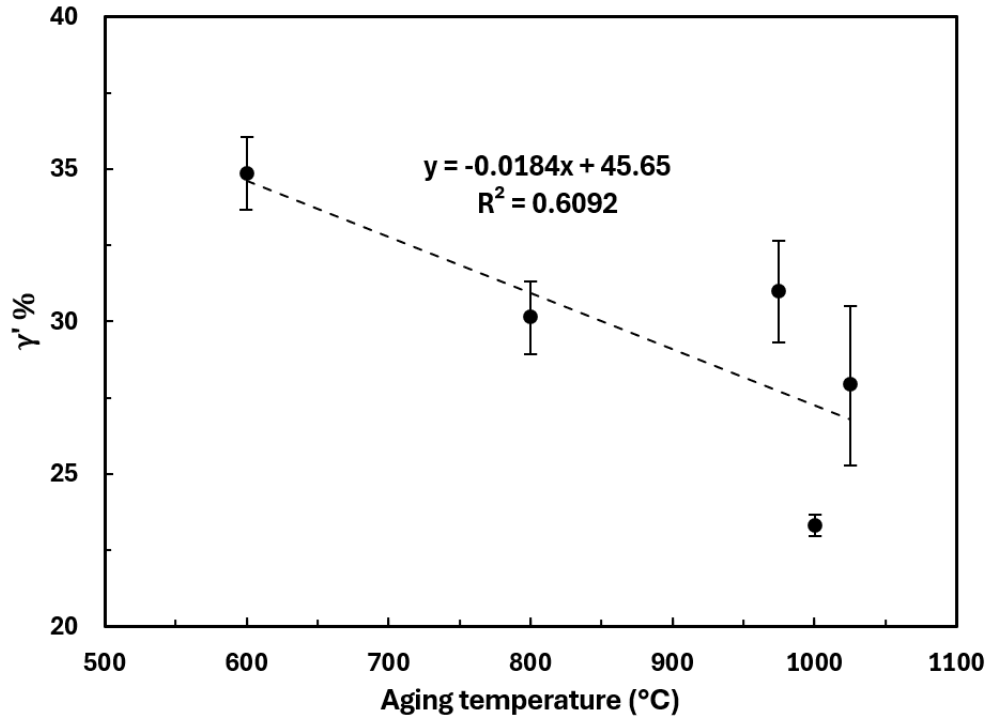

Figure 3.49: Secondary γ′ volume fraction as a function of aging temperature, with a linear fit superimposed on the data.

The differences in the secondary γ′ population are closely reflected in the hardness values obtained after aging. The results span a wide range, from 305 to 372 HB10, as expected given the considerable microstructural variation across the five temperatures. As shown in Figure 3.50, the trend is non-monotonic. The benchmark established by the sample solution treated at 1220 °C with slow cooling is 332 HB10.

The AG 600 sample presents a value almost coincident with this baseline at 336 HB10, indicating that at this temperature the aging treatment had a negligible effect on hardness. The AG 800 sample achieves the highest hardness among all samples at 372 HB10 and is the only condition that produces a meaningful improvement over the solution-treated benchmark.

Above 800 °C, hardness drops to 305 HB10 at 975 °C and 307 HB10 at 1000 °C, falling well below the benchmark, before recovering slightly to 317 HB10 at 1025 °C. This partial recovery coincides with the $M_{23}C_6$ formation temperature indicated by DSC data and is likely attributable to the pinning effect of carbides precipitated at grain boundaries at this condition. The decrease in hardness between 800 °C and 975 °C is consistent with an overaging effect, characterised by excessive coarsening of secondary γ′ and the disappearance of tertiary γ′ from the microstructure.

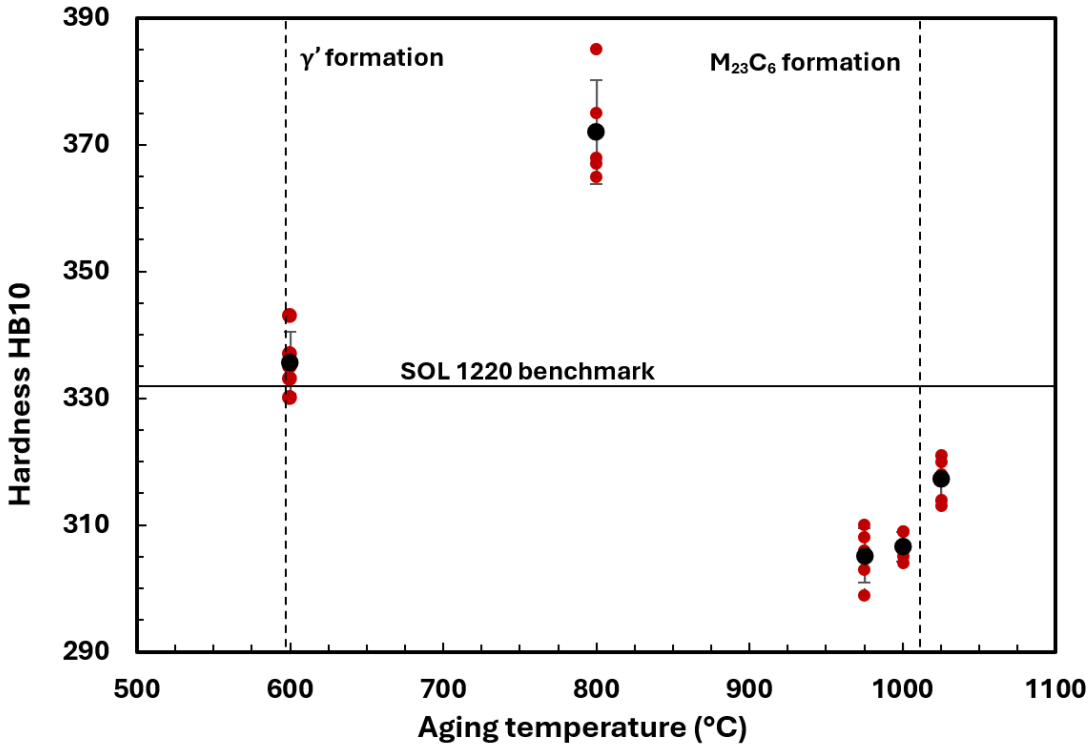

Figure 3.50: Hardness values for all the HIP 1220 SOL 1220-S samples aged at different temperatures for 4 hours.

4. Conclusions

The present work achieved a comprehensive thermal characterisation of the material, with the temperatures associated with the main phase transformations summarised in Table 4.1. These results were fundamental to the development and optimization of the heat treatment sequence, as the characteristic temperatures define the key constraints within which the treatments must operate.

Table 4.1: Characteristic transformation temperatures of the SAM alloy in the as-built and HIP STD conditions, as determined by DSC analysis.

Transformation	**As-built**	**HIP STD**
γ' precipitation	610 °C	-
γ' solvus	1148-1165 °C	1150-1170 °C
Solidus	1225 °C	1225 °C
Liquidus	1370 °C	1368 °C
MC $\rightarrow$ $M_{23}C_6$ (cooling)	1020 °C	1025 °C

For solution treatment in particular, knowledge of the γ' solvus and the solidus temperature is essential, as they represent the lower and upper thermal limits of the process window respectively. In this work, the upper limit is of particular importance, as it marks the onset of incipient melting and the associated formation of eutectic regions, which must be avoided.

Following the thermal characterisation, an extensive experimental campaign was carried out to optimize the main parameters of each heat treatment stage, investigating the influence of HIP temperature, solution temperature, solution cooling rate, and aging temperature on the resulting microstructure.

The principal finding regarding HIP and solution treatment is that the threshold for incipient melting is situated at approximately 1230 °C, representing the critical upper limit for this alloy. The HIP and SOL 1240 series clearly demonstrated that exceeding this threshold introduces irreversible microstructural damage in the form of liquid-derived phases and shrinkage porosity, which cannot be eliminated by subsequent treatments. At the same time, approaching this upper limit is desirable, since higher temperatures promote grain growth, which is beneficial for creep resistance. A temperature of 1220°C, situated 10°C below the critical threshold, therefore proved

optimal for both HIP and solution treatment. The resulting grain size values fall within the target range and are consistent with previous work on the same alloy, as discussed in Chapter 3.2.5. Beyond grain size, this condition also yields favourable results in terms of γ' volume fraction, precipitate size and hardness.

To provide a comparative overview of the microstructural and mechanical outcomes across the different processing stages, hardness was selected as the primary indicator, as it is less susceptible to the analytical variability that can affect γ' measurements by image analysis. A comparison of hardness values between the standard treatment and the optimized condition is presented in Figure 4.1, providing preliminary indicative information on the mechanical response of the material.

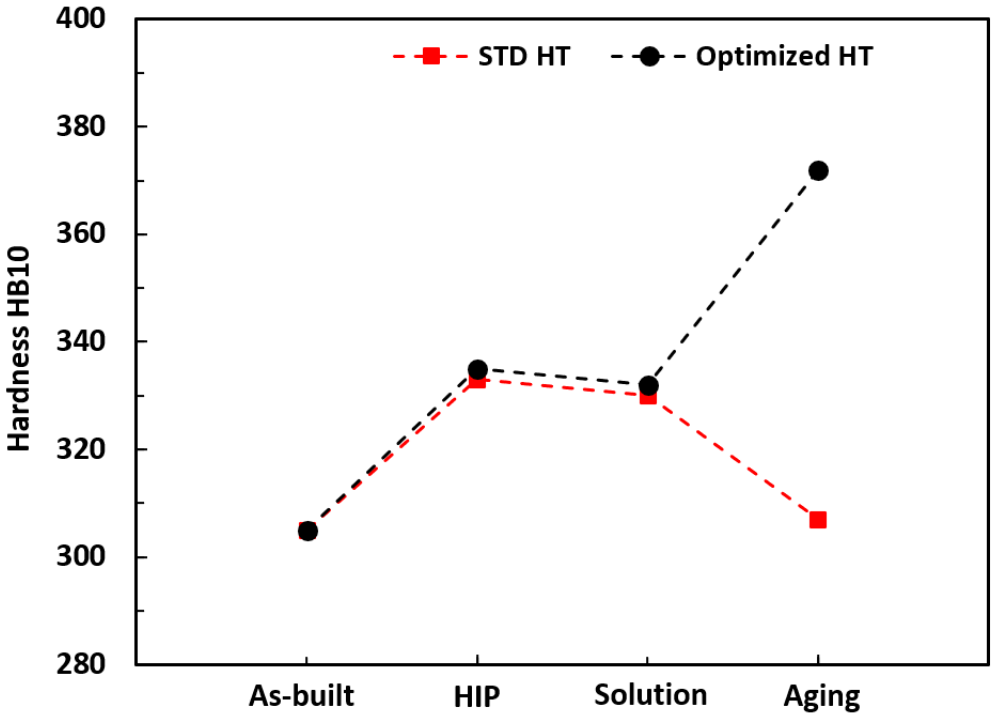

Figure 4.1: Hardness HB10 evolution across the main processing stages, comparing the standard treatment condition and the optimized heat treatment sequence.

The hardness of this alloy in the as-built state is notably lower than that of compositionally similar alloys, a characteristic that creates the potential for a meaningful increase through the successive heat treatment steps. This behaviour is directly related to the Ta/C ratio, which plays a central role in governing as-built hardness and cracking susceptibility.

A lower carbon content reduces hardness by limiting the formation of fine carbides through precipitation hardening and decreasing the contribution of interstitial solid solution hardening. A high tantalum content further suppresses hardness owing to its low diffusivity, which slows the γ' precipitation kinetics. The combined effect of reduced carbon and high tantalum content therefore results in lower as-built hardness.

As expected, HIP and solution treatment lead to a progressive increase in hardness, driven by the precipitation of γ', which strengthens the material through the precipitation strengthening mechanism. The two processing steps yield comparable hardness values, as both the temperature and holding time are identical, and the cooling rates are similar when furnace cooling is adopted for the solution step.

While air cooling allows higher hardness values to be achieved, furnace cooling is the more industrially viable option. Notably, the difference in hardness between the standard and optimized treatments at these two stages is small, confirming that the specific HIP and solution temperatures have a limited influence on the achievable hardness, with the dominant contribution coming from γ' precipitation driven by the slow cooling.

The aging treatment represents the final and most influential step in determining the hardness of the material. As discussed in Chapter 3.3.1, the choice of aging temperature has a pronounced effect on the final result. This is also clearly illustrated by the large difference between the hardness of 372 HB10 achieved with the optimized heat treatment, where an aging temperature of 800 °C was applied, and the value of 307 HB10 obtained with the standard treatment, which employs an aging temperature of 1000 °C. The optimization of this step therefore yields the most significant improvement in hardness among all the processing stages investigated.

Nevertheless, further work remains to be done before a fully optimized treatment can be established. Regarding the aging step, the temperature window has not yet been exhaustively explored, and an investigation of the 800 ± 100 °C range is recommended based on the results of this work. The holding time, fixed at 4 hours throughout this study, also warrants further investigation. Once the optimal temperature has been identified, a systematic exploration of longer holding times, starting from 4 hours and extending to 8, 16, and if necessary, beyond, is strongly recommended. A double-step aging treatment, commonly reported in the literature for similar superalloys, should also be considered as a candidate for the final optimized schedule.

Beyond the aging treatment, the microstructural and hardness data obtained in this work provide a valuable preliminary indication of the mechanical performance of the alloy, but more representative testing is needed for a comprehensive assessment. Tensile tests on fully heat-treated specimens are planned to complement the hardness measurements and to quantify strength and ductility under conditions closer to those of real applications. Creep rupture life testing will also be carried out to verify whether the targets established in previous work on the alloy, as outlined in Chapter 1.4.1, can be met and to assess the competitiveness of the final product against other superalloys in the same class.

Finally, scaling the heat treatment process from laboratory specimens to real components of larger size and complex geometry represents an essential step toward process certification and industrial implementation.

References

[1] B. Blakey-Milner, P. Gradl, G. Snedden, M. Brooks, J. Pitot, E. Lopez, M. Leary, F. Berto and A. Du Plessis, "Metal additive manufacturing in aerospace: A review," *Materials & Design,* vol. 209, no. 110008, 2021.

[2] E. Sacco and K. M. Seung, "Additive Manufacturing for Space: Status and Promises," *International Journal of Advanced Manufacturing Technology,* vol. 105, no. 10, pp. 4123-4146, 2019.

[3] N. Tepylo, X. Huang and P. C. Patnaik, "Laser-based additive manufacturing technologies for aerospace applications," *Advanced Engineering Materials,* vol. 21, no. 11, 2019.

[4] H. Bikas, P. Stavropoulos and G. Chryssolouris, "Additive manufacturing methods and modelling," *Additive manufacturing methods and modelling approaches: a critical review,* vol. 83, pp. 389-405, 2016.

[5] E. Chauvet, P. Kontis, E. A. Jägle, B. Gault, D. Raabe, C. Tassin, J.-J. Blandin, R. Dendievel, B. Vayre, S. Abed and G. Martin, "Hot cracking mechanism affecting a non-weldable Ni-based superalloy produced by selective electron Beam Melting," *Acta materialia,* vol. 142, pp. 82-94, 2018.

[6] T. DebRoy, H. Wei, J. Zuback, T. Mukherjee, J. Elmer, J. Milewski, A. Beese, A. Wilson-Heid, A. De and W. Zhang, "Additive Manufacturing of Metallic Components – Process, Structure and Properties," *Progress in Materials Science,* vol. 92, no. C, p. 112–224, 2018.

[7] I. Yadroitsev, I. Yadroitsava, A. Du Plessis and E. MacDonald, Fundamentals of Laser Powder Bed Fusion of Metals, Amsterdam: Elsevier, 2021.

[8] M. Taghian, M. H. Mosallanejad, E. Lannunziata, G. Del Greco, L. Iuliano and A. Saboori, "Laser powder bed fusion of metallic components: Latest progress in productivity, quality, and cost perspectives," *Journal of Materials Research and Technology,* vol. 27, pp. 6484-6500, 2023.

[9] O. Rehme and C. Emmelmann, "Reproducibility for properties of selective laser melting," in *Proceedings of the Third International WLT-Conference on Lasers in Manufacturing*, Munich, 2005.

[10] M. W. Barsoum, MAX Phases : Properties of Machinable Ternary Carbides and Nitrides, Wiley, 2013.

[11] N. T. Aboulkhair, M. Simonelli, L. Parry, I. Ashcroft, C. Tuck and R. Hague, "3D Printing of Aluminium Alloys: Additive Manufacturing of Aluminium Alloys Using Selective Laser Melting," *Progress in Materials Science,* vol. 106, no. 100578, 2019.

[12] Y. Zhai, D. A. Lados, E. J. Brown and G. N. Vigilante, "Understanding the microstructure and mechanical properties of Ti-6Al-4V and Inconel 718 alloys manufactured by Laser Engineered Net Shaping," *Additive manufacturing,* vol. 27, pp. 334-344, 2019.

[13] X. Zhao and T. Wang, "Laser Powder Bed Fusion of Powder Material: A Review," *3D printing and additive manufacturing,* vol. 10, no. 6, pp. 1439-1454, 2023.

[14] A. Azarniya, X. G. Colera, M. J. Mirzaali, S. Sovizi, F. Bartolomeu, M. St Weglowski, W. W. Wits, C. Y. Yap, J. Ahn, G. Miranda, F. S. Silva and H. R. Madaah Hosseini, "Additive manufacturing of Ti–6Al–4V parts through laser metal deposition (LMD): Process, microstructure, and mechanical properties," *Journal of alloys and compounds,* vol. 804, pp. 163-191, 2019.

[15] L. Tonelli, "Revealing the Hierarchical Microstructure of Innovative Additively Manufactured Metal Parts with Conventional Light Microscopy," *Metallography, microstructure, and analysis,* vol. 10, no. 2, pp. 278-282, 2021.

[16] J. Guan and Q. Wang, " Laser Powder Bed Fusion of Dissimilar Metal Materials: A Review," *Materials,* vol. 16, no. 7, p. 2757, 2023.

[17] S. Chowdhury, N. Yadaiah, C. Prakash, S. Ramakrishna, S. Dixit, L. R. Gupta and D. Buddhi, " Laser powder bed fusion: a state-of-the-art review of the technology, materials, properties & defects, and numerical modelling," *Journal ot Materials Research and Technology,* vol. 20, p. 2109–2172, 2022.

[18] W. Abd-Elaziem, S. Elkatatny, A.-E. Abd-Elaziem, M. Khedr, M. A. Abd El-baky, M. A. Hassan, M. Abu-Okail, M. Mohammed, A. Järvenpää, T. Allam and A. Hamada, " On the current research progress of metallic materials fabricated by laser powder bed fusion process: a review," *Journal of materials research and technology,* vol. 20, pp. 681-707, 2022.

[19] B. Yin, W. Yong, J. Zhu, H. Ge, S. Zhu, Y. Gui, W. Zhang, H. Fu and J. Xie, "Compositional design of Ni-based superalloys for additive manufacturing: Progress and perspectives," *Materials science & engineering. R, Reports : a review journal,* vol. 169, p. 101185, 2026.

[20] B. Saleh, R. Fathi and L. Zhao, "Additive manufacturing of nickel superalloys: A critical review of recent advances and future perspectives," *Applied materials today,* vol. 48, no. 103051, 2026.

[21] G. Jianting, Z. Y. and Z. Hongen, "Effects of rare earth elements on mechanical properties and chemical properties of Fe-Ni-Cr based alloys," *Journal of the Chinese Rare Earth Society,* vol. 5, no. 1, 1987.

[22] C. T. Sims, "A history of superalloy metallurgy for superalloy metallurgists," *Superalloys,* pp. 399-419, 1984.

[23] C. M. Katsari, A. Wessman and S. Yue, "Heat Treatment Optimization of a γ'-Strengthened Nickel-Based Superalloy Based on Central Composite Design," *Metallurgical and materials transactions. A, Physical metallurgy and materials science,* vol. 51, no. 11, pp. 5806-5817, 2020.

[24] H. Cai, J. Hou, Y.-a. Guo, J. Xing and L.-z. Zhou, "The evolution of carbides during long-term creep/aging of nickel based superalloy K444," *Journal of Materials Research and Technology,* vol. 28, pp. 3631-3640, 2024.

[25] S. E. Atabay, O. Sanchez-Mata, J. A. Muniz-Lerma and B. M., "Effect of heat treatment on the microstructure and elevated temperature tensile properties of Rene 41 alloy produced by laser powder bed fusion," *Journal of Alloys and Compounds,* vol. 858, no. 157645, 2021.

[26] H. Jin, J. Zhang, Y. Zhang, W. Zhang, S. Ma, S. Mao, Y. Du, Z. Wang, J. Qin and Q. Wang, "Effects of the orientation relationships between TCP phases and matrix on the morphologies of TCP phases in Ni-based single crystal superalloys," *Materials Characterization,* vol. 183, no. 111609, 2022.

[27] R. Reed, "Summary and future trends," in *The Superalloys: Fundamentals and Applications*, Cambridge University Press, 2006.

[28] R. Jiang, Y. D. Song and P. A. Reed, "Fatigue crack growth mechanisms in powder metallurgy Ni-based superalloys—A review," *International Journal of Fatigue,* vol. 141, no. 105887, 2020.

[29] G. Raisson, "Evolution of PM nickel base superalloy processes and products," *Powder Metallurgy,* vol. 51, no. 1, pp. 10-13, 2008.

[30] C.-j. WU, Y. Tao and J. Jia, "Microstructure and Properties of an Advanced Nickel-base PM Superalloy," *Journal of Iron and Steel Research, International,* vol. 21, no. 12, pp. 1152-1157, 2014.

[31] L. Yang, X. Ren, C. Ge and Q. Yan, "Status and development of powder metallurgy nickel-based disk superalloys," *International journal of material research,* vol. 110, no. 10, pp. 901-910, 2019.

[32] J. BAI, J. LIU, J. JIA and Y. ZHANG, "Creep Properties and Solute Atomic Segregation of High-W and High-Ta Type Powder Metallurgy Superalloy," *ACTA METALLURGICA SINICA,* vol. 59, no. 9, 2023.

[33] S. Sanchez, P. Smith, Z. Xu, G. Gaspard, C. J. Hyde, W. W. Wits, I. A. Ashcroft, H. Chen and A. T. Clare, "Powder Bed Fusion of nickel-based superalloys: A review," *International Journal of Machine Tools and Manufacture,* vol. 165, no. 103729, 2021.

[34] H. Hamdi, S. Sadatabhari, A. Tajik, A. Z. Hanzaki, A. Hatamiyan and H. R. Abedi, "From melt pool to performance: A review of microstructural engineering in the additive manufacturing of nickel-based superalloys," *Results in Engineering,* vol. 28, no. 107402, 2025.

[35] W. Zheng, Y. Zhu, Y. Zhang, A. Huang, H. Wang and K. Zhang, "Research on heat treatment of nickel–based superalloys by laser powder bed fusion: A review," *Journal of alloys and compounds,* vol. 1010, no. 177522, 2025.

[36] L. Gong, Y.-B. Li, X.-P. Wang, S. Li, Z.-G. Yang and H. Chen, "Progress in additive manufacturing of nickel-based superalloys:," *Rare metals,* vol. 44, no. 10, pp. 7041-7087, 2025.

[37] J. Xu, *Alloy Design and Characterization of γ' Strengthened Nickel-based Superalloys for Additive Manufacturing,* 2021.

[38] J. Cormier and C.-A. Gandin, "Processing of directionally cast nickel-base superalloys: solidification and heat treatments," in *Nickel Base Single Crystals Across Length Scales*, Elsevier, 2022, pp. 193-222.

[39] S. C. Krishna, N. K. Gangwar, A. K. Jha, B. Pant and P. Venkitakrishnan, "On the direct aging of iron based superalloy hot rolled plates," *Materials science & engineering. A, Structural materials : properties, microstructure and processing,* vol. 648, pp. 274-279, 2015.

[40] N. El-Bagoury, M. Waly and A. Nofal, "Effect of various heat treatment conditions on microstructure of cast polycrystalline IN738LC alloy," *Materials science & engineering. A, Structural materials : properties, microstructure and processing,* vol. 487, no. 1, pp. 152-161, 2008.

[41] A. Ramakrishnan and G. Dinda, "Direct laser metal deposition of Inconel 738," *Materials science & engineering. A, Structural materials : properties, microstructure and processing,* vol. 740, pp. 1-13, 2019.

[42] G. Wang, L. Yang, G. Dai, C. Chen, Y. Xuanyuan, W. Wu, Y. Qin and S. Yang, "Influence of post-heat treatments on the microstructure and mechanicalproperties of Inconel 738 produced by laser directed energy deposition," *Journal of materials research and technology,* vol. 33, no. 7182-7192, 2024.

[43] O. M. D. M. Messé, R. Muñoz-Moreno, T. Illston, S. Baker and H. J. Stone, "Metastable carbides and their impact on recrystallisation in IN738LC," *Additive Manufacturing,* vol. 22, p. 394–404, 2018.

[44] M. Mostafaei and S. Abbasi, "Influence of Zr Content on the Incipient Melting Behavior and Stress-Rupture Life of CM247 LC Nickel Base Superalloy," *Journal of Alloys and Compounds,* vol. 648, p. 1031–1037, 2015.

[45] H. E. Huang and C. H. Koo, "Characteristics and mechanical properties of polycrystalline CM 247 LC superalloy casting," *Materials Transactions,* vol. 45, no. 2, pp. 562-568, 2004.

[46] A. Seidel, T. Finaske, A. Straubel, H. Wendrock, T. Maiwald, M. Riede, E. Lopez, F. Brueckner and C. Leyens, "Additive Manufacturing of Powdery Ni-Based Superalloys Mar-M-247 and CM 247 LC in Hybrid Laser Metal Deposition," *Metallurgical and materials transactions. A, Physical metallurgy and materials science,* vol. 49, no. 9, pp. 3812-3830, 2018.

[47] V. Divya, R. Muñoz-Moreno, O. Messé, J. Barnard, S. Baker, T. Illston and H. Stone, "Microstructure of selective laser melted CM247LC nickel-basedsuperalloy and its evolution through heat treatment," *Materials Characterization,* vol. 114, no. 62-74, 2016.

[48] E. Bassini, A. Sivo, P. Martelli, E. Rajczak, G. Marchese, F. Calignano, S. Biamino and D. Ugues, "Effects of the solution and first aging treatment applied to as-built andpost-HIP CM247 produced via laser powder bed fusion (LPBF)," *Journal of alloys and compounds,* vol. 905, no. 164213, 2022.

[49] R. Baldan, R. L. P. da Rocha, R. B. Tomasiello, C. A. Nunes, A. M. da Silva Costa, M. J. R. Barboza, G. C. Coelho and R. Rosenthal, "Solutioning and Aging of MAR-M247 Nickel-Based Superalloy," *Journal of materials engineering and performance,* vol. 22, no. 9, pp. 2574-2579, 2013.

[50] A. Basak and S. Das, "Microstructure of nickel-base superalloy MAR-M247 additivelymanufactured through scanning laser epitaxy (SLE)," *Journal of alloys and compounds,* vol. 705, pp. 806-816, 2017.

[51] M. Ramsperger and S. Eichler, "Electron Beam Based Additive Manufacturingof Alloy 247 for Turbine Engine Application: FromResearch towards Industrialization," *Metallurgical and materials transactions. A, Physical metallurgy and materials science,* vol. 54, no. 5, pp. 1730-1743, 2023.

[52] K. Dorries, J. Rosler, C. Haberland, J. Burow, B. Gehrmann and S. Piegert, "Nickel-base alloy composition for component parts with reduced susceptibility to cracking and optimized high-temperature properties". Patent US20240011128A1, 1 january 2024.

[53] B. Gehrmann, J. Burow, R. Joachim, C. Haberland, S. Piegert and D. Kai, "Method for manufacturing a metal component". Patent WO2025098567A1, 15 May 2025.

[54] Y. T. Tang, C. Panwisawas, J. N. Ghoussoub, Y. Gong, J. W. Clark, A. A. Németh, D. G. McCartney and R. C. Reed, "Alloys-by-design: Application to new superalloys for additive manufacturing," *Acta materialia,* vol. 22, pp. 417-436, 2021.

[55] A. Basak, "Additive Manufacturing of High-Gamma Prime Nickel-Based Superalloys through Selective Laser Melting (SLM)," *Solid Freeform Fabrication 2019: Proceedings of the 30th Annual International Solid Freeform Fabrication Symposium – An Additive Manufacturing Conference,* 2019.

[56] A. Basak and S. Das, "Additive Manufacturing of Nickel-Base Superalloy René N5 through Scanning Laser Epitaxy (SLE) − Material Processing, Microstructures, and Microhardness Properties," *Advanced engineering materials,* vol. 19, no. 3, 2017.

[57] D. Migas and M. Tomasz, "Superalloys: methodological aspects of thermal analysis," *Journal of Thermal Analysis and Calorimetry,* vol. 148, no. 4, pp. 1491-1500, 2023.

[58] W. Boettinger, U. Kattner, K. Moon and J. Perepezko, "NIST recommended practice guide: DTA and heat-flux DSC measurements of alloy melting and freezing," pp. 1-50, 2006.

[59] ASTM, *ASTM E10-23: Standard Test Method for Brinell Hardness of Metallic Materials,* West Conshohocken: ASTM International, 2023.

[60] W. Shao, Y. Hou, J. Tang, Q. Liu, H. Ding and Z. Li, "On the predictive modeling of surface micro-topography in vibratory polishing of aeronautic gear considering initial workpiece topography," *The International Journal of Advanced Manufacturing Technology,* vol. 126, no. 3-4, pp. 1553-1565, 2023.

[61] ASTM, *ASTM E112-25: Standard Test Methods for Determining Average Grain Size,* West Conshohocken: ASTM international, 2025.

[62] ASTM, *ASTM E562-19e1: Standard Test Method for Determining Volume Fraction by Systematic Manual Point Count,* West Conshohocken: ASTM International, 2019.

[63] F. Schulz, K. Lindgren, J. Xu and E. Hryha, "Gamma prime formation in nickel-based superalloy IN738LC manufactured by laser powder bed fusion," *Materials Today Communications,* vol. 38, p. 2, 2024.

[64] X. Zhang, H. Chen, L. Xu, J. Xu, X. Ren and X. Chen, "Cracking mechanism and susceptibility of laser melting deposited Inconel 738 superalloy," *Materials & Design,* vol. 183, pp. 5-6, 2019.

[65] O. A. Ojo, N. L. Richards and M. C. Chaturvedi, "Study of the fusion zone and heat-affected zone microstructures in tungsten inert gas-welded INCONEL 738LC superalloy," *Metallurgical and Materials Transactions,* vol. A37, pp. 421-433, 2006.

[66] S. Xiaoqing, W. Yongxin, Z. Xiaoxiao, Z. Jing, L. Yan, W. Yifan and C. Zheng, "Analysis of carbide transformation in MC-M23C6 and its effect on mechanical properties of Ni-based superalloy," *Journal of Alloys and Compounds,* vol. 911, no. 164959, 2022.

[67] Ł. Rakoczy, M. Grudzień-Rakoczy, R. Cygan, T. Kargul and A. Zielińska-Lipiec, "Microstructure and selected properties of the solution heat-treated MAR-M247 Ni-based superalloy fabricated via directional solidification," *The International Journal of Advanced Manufacturing Technology,* vol. 3, no. 130, pp. 1321-1339, 2024.

[68] Ł. R. B. Rakoczy, M. Grudzień-Rakoczy, R. Cygan, W. Ratuszek and A. Zielińska-Lipiec, "Analysis of γ' precipitates, carbides and nano-borides in heat-treated Ni-based superalloy using SEM, STEM-EDX, and HRSTEM," *Materials,* vol. 13, no. 19, p. 4452, 2020.

[69] Y. Ji, C. Yang, T. Xu, L. Xu, Y. Li, C. Hu and H. Dong, "Study on the characteristics and high-temperature dissolution mechanism of eutectic carbides

in medium-alloy steel," *Journal of Materials Research and Technology,* vol. 31, pp. 276-286, 2024.

[70] N. El-Bagoury, M. Waly and A. Nofal, "Effect of various heat treatment conditions on microstructure of cast polycrystalline IN738LC alloy," *Materials Science and Engineering,* vol. 487, no. 1, p. 152–161, 2008.

[71] G. N. Bersano, *Optimization of Solution Heat Treatment for a Novel Nickel-Base Superalloy Design for PBF-LB Process,* Politecnico di Torino, 2025.

[72] Y. Zhang, L. Qin, B. Zhu, H. Jiang, L. Tan, T. Huang, B. Gan, Z. Jie and L. Liu, "Optimizing a Solution Heat Treatment by Increasing the Cooling Rate of Directional Solidification for Ni-Based Superalloys," *Materials,* vol. 16, no. 9, p. 3433, 2023.

[73] J. V. Gordon, S. P. Narra, R. W. Cunningham, H. Liu, H. Chen, R. M. Suter, J. L. Beuth and A. D. Rollett, "Defect structure process maps for laser powder bed fusion additive manufacturing," *Additive manufacturing,* vol. 36, no. 101552, 2020.

[74] L. Xu, J. Zhou, C. Cui, C. Sun and S. Xie, "Precipitation of the gamma prime phase in a Ni-co-based superalloy during different stages of cooling," *Materials characterization,* vol. 16, no. 114235, 2024.

[75] Q. Tian, W. Zhang, J. Du, T. Lu, Y. Liu, X. Liu, H. Li and K. Wang, " Growth and dissolution behavior and morphology evolution of γ' precipitates in GH4742 nickel-based superalloy," *Journal of materials research and technology,* vol. 32, pp. 4198-4211, 2024.

[76] N. Boonlert, Z. Wang, K. Chen, H. Shen, P. Zhang and R. Narayan, "Cooling rate and solution temperature dependent γ' coarsening mechanism in DZ125 Ni-based superalloy," *Materials characterization,* vol. 228, no. 115429, 2025.

[77] M. Kenevisi, P. Martelli, I. Titonel, E. Bassini, G. Marchese and D. Ugues, "The effect of solution annealing on additively manufactured and hot isostatically pressed René 80 Ni-based superalloy," *Journal of materials research and technology,* vol. 33, pp. 6591-6600, 2024.

[78] K. Dörries, C. Haberland, J. Burow, J. Rösler, B. Gehrmann, C. Somsen, P. S. and H. Brodin, "Beyond Hot Cracking: Impact of Minor Elements on a Novel Ni-Based Superalloy for Additive Manufacturing," in *Superalloys 2024. The Minerals, Metals & Materials Series*, Springer, 2024.

[79] L. Jiang, W.-Z. Zhang, Z.-F. Xu, H.-F. Huang, X.-X. Ye, B. Leng, L. Yan, Z.-J. Li and X.-T. Zhou, "M2C and M6C carbide precipitation in Ni-Mo-Cr based superalloys containing silicon," *Materials & design,* vol. 112, pp. 300-308, 2016.

[80] K. Öztürk, A. Kısasöz, G. Özer and A. Karaaslan, "Precipitation of carbides in a nickel-based cast heat-resistant alloy during thermal exposure: evolution of microstructure, hardness and corrosion properties," *Materials Testing,* vol. 65, no. 2, pp. 233-243, 2023.

[81] Q. Wang, J. Song, C. Xiao, Y. Kang, Y. Wu, D. Wang and F. Liu, "A cross-scale study on synergistic deformation mechanisms between the grain boundary orientation and carbide morphology in nickel-based superalloys," *Materials science & engineering. A, Structural materials : properties, microstructure and processing,* vol. 935, no. 148369, 2025.

[82] K. Dörries, Advancing Alloy Design: A Study of Novel and Conventional Cast Ni-based Superalloys in Additive Manufacturing, 2025.

[83] S. Lerda, B. Luo, G. Marchese, X. Zhao, S. Biamino and S. Dadbakhsh, "Role of the preheating temperature during electron beam powder bed fusion (PBF-EB/M) in precipitation of $\gamma'$and carbides in Inconel 738 superalloy," *Journal of Materials Research and Technology,* vol. 37, pp. 4639-4650, 2025.